Transfer reaction measurements and the stellar nucleosynthesis of ^{26}Al and ^{44}Ti

Vincent Margerin
School of Physics and Astronomy

A thesis submitted for the degree of Doctor of Philosophy
of the University of Edinburgh

March, 2016

Lay summary

The atomic elements found in the Universe have been produced in two stages. Hydrogen and Helium were produced in the immediate aftermath of the Big Bang. And, for billions and billions of years stars have been cooking up the rest, including carbon, nitrogen, oxygen or the calcium of our bones.

Some of these elements have radioactive isotopes. For example, everybody knows aluminium. But what we call aluminium is the stable version, which contains 13 protons and 14 neutrons or ^{27}Al, and it is indeed produced by stars. But ^{27}Al does not decay, hence it does not send "signals" of its existence; unlike aluminium-26. This radio-isotope is not stable. When it is formed in a star it decays into ^{26}Mg that is stable just like ^{27}Al and has one less proton. However it does not decay to the stable form of ^{26}Mg. If it did, the only emitted "signals" would be electrons, which would never reach us even if the next star was just next to the Moon, and anti-neutrinos, but we would not be able to tag those either. No, ^{26}Al decays to an excited form of ^{26}Mg which needs to release the energy excess to re-arrange itself in a stable structure. The release of this energy is made via the emission of a gamma-ray, an electromagnetic relaxation that carries the energy excess (1.809 MeV). In the Universe's vacuum this γ-ray will fly unstopped such that we can collect it in satellite based γ-ray observatories. And the quantity we measure tells us about the ability of the observed star to create ^{26}Al, from which some of its characteristics can be derived. Similarly, titanium-44 is produced when the most massive of stars collapse to such density that a cataclysmic (outward) explosion is generated, called a supernova event. The masses involved are so huge that what is left, from the explosion, may be a neutron star or even a black hole. So when we measure the flux of ^{44}Ti from the remnant of a core collapse supernova we can derive information about the strength of the explosion.

Nuclear physics slots in as it provides key ingredients: the reaction rates between nuclei involved in producing/destroying ^{26}Al and ^{44}Ti. These rates allow to precisely define how much of one or the other is produced as a function of the star's temperature. Without those reaction rates the information extracted from

the in-space observations cannot yield meaningful results.

In this work, we first investigate what stellar environments are responsible for the production and destruction of ^{26}Al and ^{44}Ti, and focus on the reactions that control their production rate. We then turn to pioneering experimental methods that we can use, here on Earth, to reproduce these stellar reactions. From the analysis of these experiments we will draw conclusions on the information gained on the relevant star formation.

Abstract

Progress in the description of stellar evolution is driven by the collaborative effort of nuclear physics, astrophysics and astronomy. Using those developments, the theory of the origin of elements in the Universe is challenged. This thesis addresses the problem behind the abundance of ^{44}Ti and the origin of ^{26}Al.

The mismatch between the predicted abundance of ^{44}Ti as produced by the only sites known to be able to create ^{44}Ti, core collapse supernovae (CCSNe), and the observations, highlight the current uncertainty that exists in the physics of these stars. Several satellite based γ-ray observations of the isotope ^{44}Ti have been reported in recent times and confirm the disagreement. As the amount of this isotope in stellar ejecta is thought to critically depend on the explosion mechanism, the ability to accurately model the observed abundance would be a pivotal step towards validating that theory. The most influential reaction to the amount of ^{44}Ti in supernovae is ^{44}Ti(α, p)^{47}V. Here we report on a direct study of this reaction conducted at the REX-ISOLDE facility, CERN. The experiment was performed at a centre of mass energy 4.15$\pm$0.23 MeV, which is, for the first time, well within the Gamow window for core collapse supernovae. The experiment employed a beam of ^{44}Ti extracted from highly irradiated components of the SINQ spallation neutron source of the Paul Scherrer Institute. No yield above background was observed, enabling an upper limit for the rate of this reaction to be determined. This result is below expectation, suggesting that the ^{44}Ti(α, p)^{47}V reaction proceeds more slowly than previously thought. Implications for astrophysical events, and remnant age, are discussed.

In Wolf-Rayet and asymptotic giant branch (AGB) stars, the ^{26g}Al(p, γ)^{27}Si reaction is expected to govern the destruction of the cosmic γ-ray emitting nucleus ^{26}Al. The rate of this reaction, however, is highly uncertain due to the unknown properties of several resonances in the temperature regime of hydrogen burning. We present a high-resolution inverse kinematic study of the ^{26g}Al(d, p)^{27}Al reaction as a method for constraining the strengths of key astrophysical resonances in the ^{26g}Al(p, γ)^{27}Si reaction. In particular, the results indicate that the resonance at E$_r$ = 127 keV in ^{27}Si determines the entire ^{26g}Al(p, γ)^{27}Si reaction rate over

almost the complete temperature range of Wolf-Rayet stars and AGB stars. The measurements of spectroscopic factors for many states in ^{27}Al and a shell model calculation of nuclear properties of *rp*-resonant states in ^{27}Si also allow for testing the structure model.

Preface

This work describes a study of the ^{26}Al(d, p)^{27}Al and ^{44}Ti(α, p)^{47}V nuclear reactions. The investigation of the former reaction was proposed by Professor Philip Woods and Dr Gavin Lotay. The experiment was conducted in several phases at the TRIUMF facility in Vancouver, Canada. The campaign spanned a period from 2010 to 2012, time at which I was not part of the Edinburgh group. Consequently I did not take part in the experiments, however the entirety of the analysis work is mine. A sort code existed that I adapted, and largely modified it to meet the needs of the experiment. I developed all subsequent codes, apart from the penetrability factor calculation that helps to calculate reaction rates at energies corresponding to star temperatures. The later was generated using an existing code. The study of the ^{44}Ti(α, p)^{47}V reaction was proposed by Professor Alex Murphy after the ERAWAST project, which he helped kick off, become able to deliver a ^{44}Ti sample from beam dumps of the PSI facility near Zurich, Switzerland. The experiment was done at CERN, Geneva, Switzerland in November 2012. Having formally started in September 2012 I was able to spend time on the choice of windows but the design of the gas cell itself was anterior to the experiment proposal. Here, too, the rest of the work, including the suite of codes needed, was entirely mine unless duly referenced, such as the Monte Carlo simulation of Professor Alex Murphy (but, for example, the 2D plotting code is my work), a code used already in several works from the Edinburgh group and prior to my arrival, as well as other studies from other nuclear groups in the UK.

Part of this thesis has been published in:

Study of the ^{44}Ti(α, p)^{47}V Reaction and Implications for Core Collapse Supernovae
V. Margerin, A.St.J. Murphy, T. Davinson, R. Dressler, J. Fallis, A. Kankainen, A.M. Laird, G. Lotay, D.J. Mountford, C.D. Murphy, C. Seiffert, D. Schumann, T. Stowasser, T. Stora, C.H.-T. Wang, P.J. Woods
Physics Letter B **731** (2014) 358-361.

Inverse Kinematic Study of the ^{26}gAl(d, p)^{27}Al Reaction and Implications for Destruction of ^{26}Al in Wolf-Rayet and Asymptotic Giant Branch Stars

V. Margerin, G. Lotay, P.J. Woods, M. Aliotta, G. Christian, B. Davids, T. Davinson, D.T. Doherty, J. Fallis, D. Howell, O.S. Kirsebom, D.J. Mountford, A. Rojas, C. Ruiz, and J.A. Tostevin

Physical Review Letters **115** (2015) 062701

The following oral presentations were also given about this PhD work:

- *Measurement of neutron spectroscopic factors in ^{27}Al from the ^{26}Al(d, p)^{27}Al reaction and implications for the destruction of ^{26}Al in AGB and WR stars*, Heavy-Ion Accelerator Symposium 2015, Canberra, Australia, September 2015.

- *Measurement of neutron spectroscopic factors in ^{27}Al from the ^{26}Al(d, p)^{27}Al reaction and implications for the destruction of ^{26}Al in AGB and WR stars*, Nucleus-Nucleus 2015, Catania, Italy, 2015.

- *Titanium-44 yield in stellar ejecta, Nuclear Physics Seminar*, University of Surrey, United Kingdom, May 2014 (invited)

- *^{44}Ti(α, p)^{47}V at REX-ISOLDE. Implications for Core Collapse Supernovae*, Workshop on Nucleosynthesis: Origins and Impacts at the Royal Astronomical Society, London, February 2014 (invited)

- *Towards a Nuclear Explanation for the Obsrvation of ^{44}Ti Isotopic Excesses in Core Collapse Supernovae*, ATHENA Workshop on Astrophysics, Brussels, Belgium, January 2014

- *Measurement of the ^{44}Ti(α, p)^{47}V reaction rate at energies within the Gamow window for interpretation of satellite based γ-ray observations*, Institute of Physics Nuclear Physics Conference, York, United Kingdom, April 2013

- *Measurement of the ^{44}Ti(α, p)^{47}V reaction rate at energies within the Gamow window for interpretation of satellite based γ-ray observations*, Institute of Physics Workshop on Radioactivity in Physics, York, United Kingdom, April 2013 (invited)

Declaration

Except where acknowledged in the customary manner, the material presented in this thesis is, to the best of my knowledge, original. It represents my own work and has not been submitted in whole or in part for a degree at any other university.

Vincent Margerin
March, 2016

Contents

List of Figures

List of Tables

Chapter 1

Introduction

The origin of elements in the Universe is still not clearly understood. Following the Big Bang, the elemental composition of the Universe was simply helium and hydrogen with some residual lithium. This would not explain what is observed on Earth, in the Solar system or what makes the human body. The question of where heavier elements such as carbon and oxygen are produced was highly debated until 1957 when Burbridge, Burbridge, Hoyle and Fowler [B^{2}HF 1957], the famous B^{2}HF, presented a clear explanation for stellar nucleosynthesis demonstrating that stars are responsible for the production of those elements. The article also describes different paths for such production in different ratios or via different parts of the chart of the nuclides. The theory developed therein comprehensively described the known atomic abundances observed from the Earth at the time. Since then, tremendous development in the field of astronomy, nuclear physics and astrophysics has allowed to challenge the extent to which the theory satisfies what Nature has produced.

1.1 Observing stars

1.1.1 Nuclear reactions and emission of γ-rays

Even before the B^{2}HF paper, it was known that nuclear reactions occur in stars. A nuclear reaction occurs when a nuclear system A, evolves into a different system A', or when several species become spatially close enough that there is an interaction between them that at least changes their outgoing trajectory from what it would have been without the reaction. In most cases though one can simply write a nuclear reaction as:

$$\mathrm{A} + a \rightarrow \mathrm{B} + b + ..., \tag{1.1}$$

where, again in general, A and B are heavy nuclei and a and b are lighter nuclei, *e.g.* α-particles, protons or neutrons, or a γ-ray or an electron. If the combined mass of A and a is greater than that of B and b, then the excess energy will be spread amongst the outgoing species. If the heavy nucleus B is excited (but still bound) then it will de-excite into its more (structurally) stable ground state by emission of one or several γ-rays. In this internal decay it can also decay to a lighter nucleus via α or β-decay. The γ-rays may be observed outside the star as its material is mostly transparent to them, such that they are not trapped into the star. The other types of particles produced, however, are stopped by the star's material regardless of their kinetic energy, which they get from the mass gap that may exist between the two sides of Equation 1.1, otherwise called the nuclear Q-value. In the case that this quantity is positive, *i.e.* the (B, b) system is heavier than (A, a), the reaction can only proceed if there is an input of an energy. This happens, for example, if the particle a comes from a previous energetically favoured reaction.

Consequently, the occurrence of nuclear reactions in a star will lead to observational features to be emitted, namely γ-rays, and when their energy may be uniquely matched to a nuclear process, their observations can deliver information needed to test the theory of the origin of the elements.

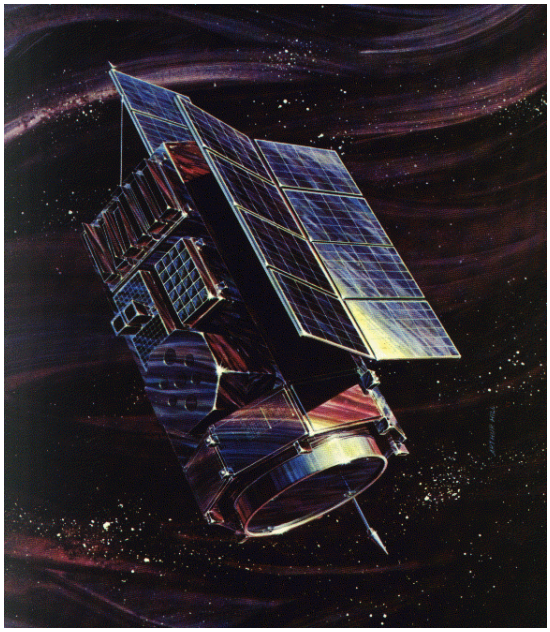

Figure 1.1: Artist impression of the HEAO satellite that orbited the Earth in 1979. The first signal from a cosmic γ-rays was recorded by the on-board instrumentation and reported in Ref. [Mahoney 1982]. The image is from www.nasa.org.

1.1.2 Looking for γ-rays in-space

The observational evidence for the occurrence of nuclear phenomenon in stars came after the theory was introduced. In fact, the first observation of a flux of γ-ray, from the stars was reported in 1982 from a mapping of the sky by the HEAO 1 satellite, see Figure 1.1 that happened in 1979 [Mahoney 1982]. The γ-rays in question were measured at an energy of 1.809 MeV, corresponding to the de-excitation of the 1.809 MeV state in ^{26}Mg, which may be populated in the β-decay of ^{26}Al.

Due to the lifetime of the ^{26}Al β-decay, $\tau \approx 10^5$ yrs, insignificantly short compared to the age of the Universe, this was also a proof of ongoing nucleosynthesis in the cosmos. Ever since this discovery, there has been tremendous development in the field of observational γ-ray astronomy. Perhaps one of the most complete results from this development was the mapping of the galactic provenance of the 1.809 MeV γ-ray by Diehl *et al.*, see, *e.g.*, Refs. [Diehl 2006, Diehl website] and Figure 1.2. These combined data from both the spectrometer onboard the INTErnational Gamma-Ray Astrophysics Laboratory (INTEGRAL) satellite mission, see Figure 1.3, and the COMPton TELescope instrumentation (COMPTEL) on the Compton Gamma-Ray Observatory (CGRO), which provided the map. Recently an astonishing insight into the asymmetry of a star's explosion was obtained thanks to the greater precision brought about by the Nuclear Spectroscopic Telescope Array (NuSTAR), see Ref. [Grefenstette 2014] and Figures 1.4 & 1.5. The most recent satellites embark observatory equipped with the latest generation of high purity Germanium detectors providing a 1 keV full-width at half maximum resolution accross the ≈30 keV to ≈2 MeV range. This is very competitive against the usual values that nuclear physicists enjoy from, for example, the use of arrays of many high purity Germanium detectors for the measurement of γ-rays (*e.g.* AGATA, CAESAR or Gammasphere), around half to a tenth of 1 keV depending on the energy of the signal.

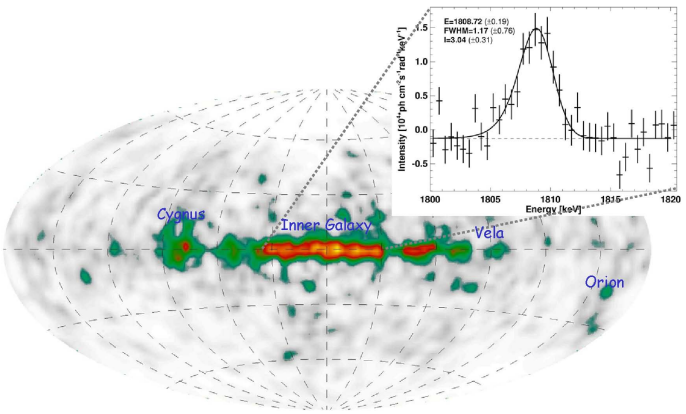

Figure 1.2: All-sky mapping and spectroscopy of the 1.809 MeV γ-ray, see Refs. [Diehl 2006, Diehl website] and references therein. This line can be linked to the decay of ^{26}Al after it has been produced in stars. This figure shows that the object producing ^{26}Al are concentrated on the galactic plane.

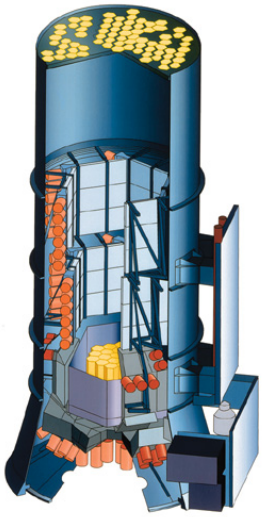

Figure 1.3: The instrument on-board INTEGRAL, the Germanium spectrometer crystals can be seen in yellow at the bottom of the equipment.

1.2 Structure of this work

In this study, the tools presented above are further described and, in the context of nuclear physics, developed for the specific case of the galactic abundance of the ^{26}Al and ^{44}Ti radionuclides. In Chapter 2, a high level description of stellar evolution is delivered and leads to the motivation for this thesis work. In Chapter 3, the theory of nuclear reactions, and, in particular, nuclear astrophysics, is developed with the main aim being to introduce the stellar reaction rate, and the concept of proton and neutron spectroscopic factors. In Chapter 4, the focus is on the development of the experimental work of this study. Since there is some overlap between the two experiments, this chapter is held as one consistent piece that still distinguishes between the two different experimental approaches used in this work. In comparison, the analysis of the experimental data is split into two chapters to accurately present the data analysis corresponding to the independent experiments for ^{26}Al, Chapter 5, and ^{44}Ti, Chapter 6. The experimental results presented in these two chapters are discussed in Chapter 7, which also presents a separated discussion of both set of results, depending on whether they correspond to the stellar environments in which ^{26}Al or ^{44}Ti are synthesised, respectively. Chapter 8 discusses the conclusions of the two experiments, bringing a final review of the results.

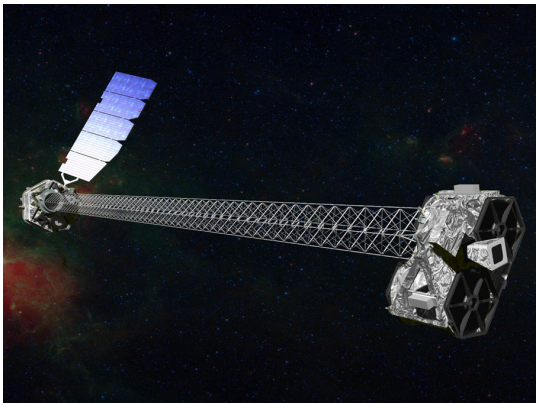

Figure 1.4: Artist impression of the NuSTAR space mission, from www.nustar.caltech.edu.

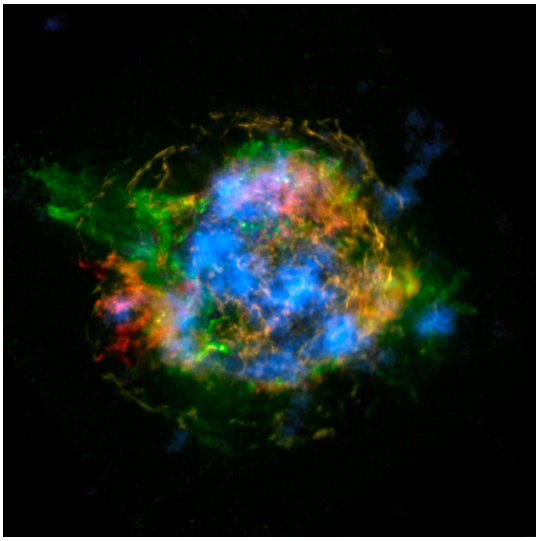

Figure 1.5: Observation of the ashes of a core collapse supernovae, Cassiopeia-A, by NuSTAR, see Ref. [Grefenstette 2014] and the www.nustar.caltech.edu website. The bright blue maps the signal from γ-rays emitted in the decay of ^{44}Ti after it is produced during the star's explosion

Chapter 2

Stellar evolution and motivation for the study of the cosmic γ-ray emitters ^{26}Al and ^{44}Ti

This chapter presents some background in the physics of the stars relevant to this thesis. Studied here are three different stellar situations: Core Collapse Supernovae (CCSNe), Wolf-Rayet (WR) and Asymptotic Giant Branch (AGB) stars. The first two are very similar, in that they both have enough mass to achieve the full stellar evolution cycle, but neither is a subset of the other, and they are classified as Type Ib, Ic and Type II which is specific to CCSNe. An AGB star is a much lighter star that has failed to evolve towards the CCSN event due to its lack of gravitational energy, hence temperature.

This chapter will first establish the astronomical classification, via a presentation of the evolution of stars on the main sequence including specific discussions of the three type of stars aforementioned. As said in the Introduction, this thesis work has been focussed on the production/destruction of two nuclei: ^{44}Ti and ^{26}Al. The former is created at the explosion stage of a CCSN, the later in the evolution stage of AGB and WR stars. This means that the information that will be extracted from the experiments will lead to conclusions of different types. While the destruction of ^{26}Al in AGB and WR stars will tell about the sites creating this nucleus, that of ^{44}Ti will help to understand the explosion mechanism of a CCSN, which is still debated.

Table 2.1: Big Bang (primordial) nucleosynthesis abundances, table made from data from Ref. [Serpico 2004].

Nuclei	Abundance Y_i
p	0.75
d	2.44×10^{-5}
^{3}He	1.0×10^{-5}
^{4}He	0.062
^{6}Li	1.1×10^{-14}
^{7}Li	4.9×10^{-10}

2.1 The evolution and hydrodynamics overview of stars

This section presents a simplified overview of the different evolutionary stages of the life of stars.

2.1.1 Birth and sequences up to the CNO cycle

Primordial nucleosynthesis

Nucleosynthesis in the Universe commenced a couple of seconds after the Big Bang, the time needed for the thermal energy to descend below the minimum required to convert protons into neutrons, and conversely, $E = (m_n - m_p) \times c^2 = 1.24$ MeV. At lower energy it is possible to start forming light nuclei. Any combination of exclusively many protons or many neutrons being unbound, the first product of primordial nucleosynthesis (PN) is the *deuteron*, d, formed from the fusion of a proton and a neutron. At that stage it may be produced via the highly exothermic reaction:

$$p + n \rightarrow d + \gamma \ , \quad E_\gamma = 2.2 \text{ MeV}. \tag{2.1}$$

Further reactions between the available species, p, n and d, take place leading to the final PN abundances shown in Table 2.1, made from data taken from Ref. [Serpico 2004]. Note the absence of $A = 5$ nuclei (mass gap), as no nuclei with A=5 are stable, similarly no $A = 8$ nuclei are produced. As expansion of the Universe goes on, the temperature cools down until it reaches a point below that that nuclear fusion may occur. In self gravitated masses the temperature, however, may rise above this threshold.

Proton-proton chain

After this period, certain clouds, formed from the PN ashes, became more structured spherical self gravitated masses consisting of H gas, with some He too. If the mass was such that the temperature could rise above 10^7 K and the density above 100 g/cm^3 then a nuclear reaction network can be triggered. It starts through the so called proton-proton mechanism which has the overall result of converting four protons into an α-particle (^{4}He). The three different reaction mechanisms performing this conversion are shown in more details in Figure 2.1. They are all initiated by:

$$p + p \rightarrow d + e^+ + \nu_e, \tag{2.2}$$

operating via the weak interaction process which is extremely slow, explaining the millions of year long first stage of the life of a star. It has in fact such a low cross section that it has never been measured directly. Observations of neutrino oscillations from the Sun's emissions, however, demonstrated its occurrence, measurements of the cross section led to the resolution of the so-called solar neutrino problem [SNO 2001].

Chains I and II release ≈26 MeV and chain II releases ≈19 MeV. This drives the luminosity of the star during this evolutionary phase and until the star has accumulated enough helium (therefore mass) to ignite the next stage as He nuclei will have enough energy to overcome the Coulomb barrier between them and fuse. Yet stars with an initial mass smaller than ∼1.5 $M_\odot$ will diverge from the main sequence at the end of the *pp* mechanism. As the *pp* H-burning ceases the star contracts and the temperature does rise within the star. However, with such an initial mass, the collapsing star does not have enough gravitation potential energy (GPE) for its conversion to heat to be sufficient for ignition of He burning, while the electron degeneracy pressure, due to particle densities forcing electrons to higher and higher energy levels, and to not being able to move to lower level to release the energy gained from GPE, cannot combat the collapse. This mass threshold is called the Chandrasekhar limit. Below this, stars eventually contract to a sphere of electron degenerate matter.

A competing scenario for hydrogen burning are the CNO cycles, for carbon, nitrogen and oxygen. This will be shown in the next section. However the occurrence of the CNO cycle owes to the presence in the progenitor star of those three elements. The early Universe being of low metallicity, *i.e.* did not contain much elements above ^{4}He, the CNO cycle only appeared in later generation of stars which are born from a mix of PN H and ashes from supernovae of this first era of stars. Observations of such phenomena have been reported in Refs. [Keller

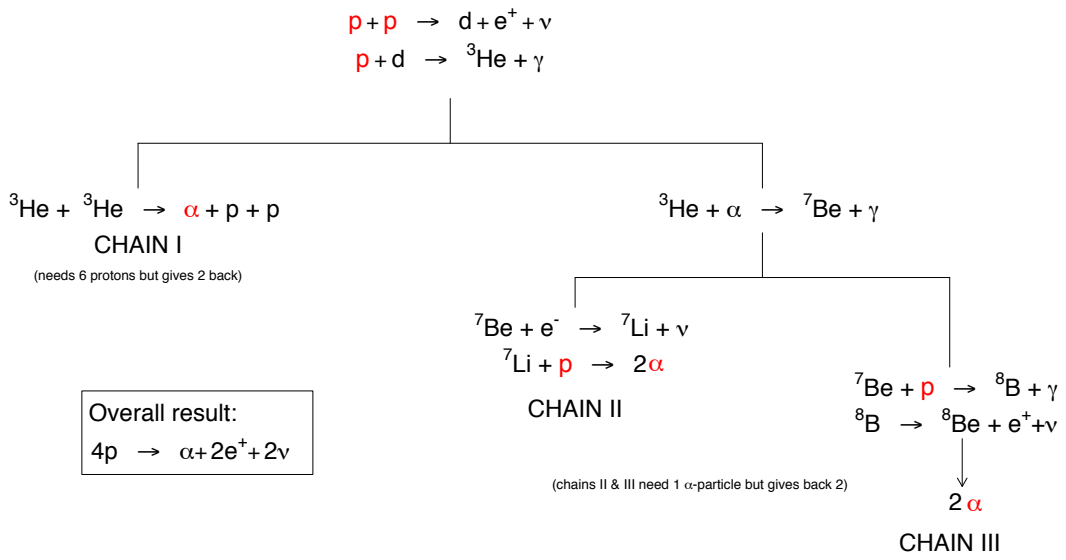

Figure 2.1: The different proton-proton chains and how they perform the conversion of four protons into one α-particle. Note that each chain has a different energy positive output that powers the luminosity of the star while it is accreting enough α-particles to gain mass and ignite the next stages. Re-edited from Ref. [Thompson & Nunes 2009].

2014, Fisher 2014]. Because of the virtually zero metallicity in the immediate post PN Universe, the first massive stars would go on from the end of the *pp*-chains to helium-burning. These stars are categorised as Population II & III stars. Their explosion led up to a metallicity enrichment of the interstellar medium, which is why for example our Sun, not massive enough to ignite fusion other than the helium conversion mechanisms has a high surface metallicity.

The CNO cycles

As newer stars contain carbon, nitrogen and oxygen, the CNO cycles become available for the creation of an α-particle from four protons. For such cycles to be ignited a star must have a progenitor mass $\gtrsim 1.5$ M$_\odot$, corresponding to a temperature $T_9 \gtrsim 0.03$ GK. Here it is via a series of reactions between protons and the CNO species that a ^{4}He nuclei is obtained, see Figure 2.2. These temperatures are much more suited to the optimal cross sections of the CNO reactions, and indeed at that stage they are much higher than the cross sections of the *pp*-chain reactions. These cycles become much faster to produce helium. Another main consequence of the CNO cycles is the high population of neon in the star. None of the reaction of interests in this thesis occur within any of the CNO cycles.

The enrichment of the interstellar medium in heavy nuclei allows for other

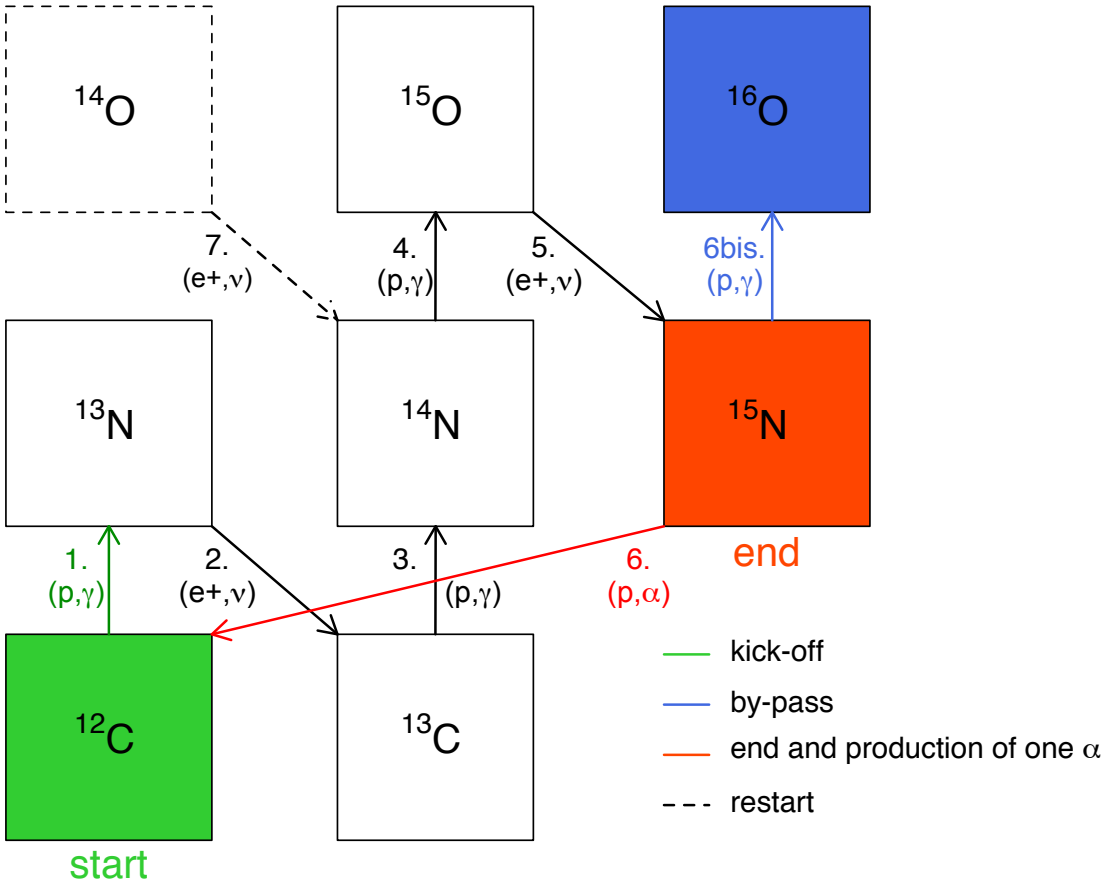

Figure 2.2: Production of an α-particle in the CNO cycle, other cycles can occur in a similar manner if heavier seeds are present in the star, e.g. ^{16}O. Consequently the by-passing of this CNO cycle may still lead to the production of an α-particle.

channels for the conversion of four protons into an α-particle in population I stars, for example, the NeNa and MgAl cycles. These require larger initial masses as more energy is required to ignite the first heavy nucleus plus proton fusion, typical sites for such cycles include Wolf-Rayet stars.

2.1.2 Later evolutionary stage of stars

After hydrogen has been consumed, a star contracts further due to gravitation energy and if its mass is such that M$\gtrsim$ 0.4 M$_\odot$, the core's temperature reaches 0.1 GK and helium burning ignites. An hydrodynamic equilibrium is re-established. In this burning phase the first main product is ^{12}C, principally via the triple-α reaction. This topic brought much interest in the history of nuclear astrophysics. Beryllium-8 is unbound, however by a mere 92 keV and, with a ground state width of 5 eV, this transcripts to a lifetime of the order of 10^{-16} s before it decays back to two α-particles. This is long enough such that a there is a possibility for two α-particles to fuse into ^{8}Be and for a third α-particle to fuse with this ensemble to create ^{12}C:

$$3\alpha \rightarrow^{8} \mathrm{Be} + \alpha \rightarrow^{12} \mathrm{C}^{*} \rightarrow^{12} \mathrm{C} + (\gamma\gamma \; or \; e^{+}e^{-}). \tag{2.3}$$

This process is only possible thanks to a resonant 0^+ state in ^{12}C at 7.7 MeV, called the Hoyle state. It has a large enough width to decay to the ground state before the three α-particles separate, see Figure 2.3. Note the possible $E0$ decay from the Hoyle state to the ground state leading to electron-positron pair creation, while the other decay proceeds through two $E2$ decays, *i.e.* the emission of two γ-rays. As the star is now formed of a C/O core with two outer layers of H and He, the later being the deeper, it evolves towards a Red Giant. Burning of the core material occurs if the progenitor mass is higher than $\sim$2.5 M$_\odot$.

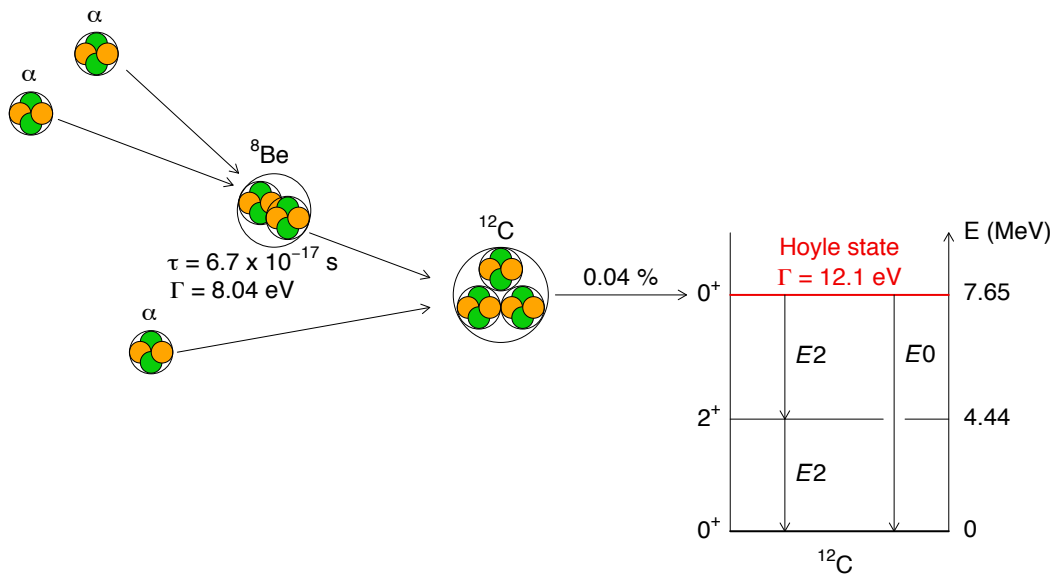

Figure 2.3: Fusion of two α-particle into ^{8}Be, and subsequent fusion of a third α-particle to produce ^{12}C in the Hoyle state.

What happens to stars with M$\lesssim$2.5 M$_\odot$?

Stars with original masses below the ∼2.5 M$_\odot$ threshold cannot gain enough temperature via GPE to trigger fusion reactions in the C/O core. However, H and He keep burning in the outer layers. At this stage the stars are called asymptotic giant branch stars as they depart the main sequence from the Red Giant evolution phase. The hydrogen burning provides large amount of energy to the inner helium layer to the point that it cannot synthesise carbon fast enough to sustain that input of energy. As a result the star suffer a thermonuclear runaway of its outer hydrogen layer powered by that energy surplus. The temperature in the left-over outer layers progressively cools to the point where hydrogen nuclei do not have the required minimum energy to fuse. Consequently the energy contribution to these stars can only come from a new stage of helium burning which provokes a new stage of radial expansion. However, the temperature of those stars drops again and helium burning ceases. This leads to a new gravitational contraction and hydrogen burning reignites. Such a cycle repeats until a pressure excess applied on the outer layers generates a stellar wind sufficiently strong to totally sweep these out of the atmosphere of the stars. This process exposes the hotter deeper layers whose thermal energy powers the stars' luminosity. The low amounts of H and He that remain burn to depletion and the stars are left only with their inert C/O core. It slowly cools down and the luminosity decreases, turning the stars from bright (white dwarves) to dark (black dwarves).

For stars with M$\gtrsim$ 2.5 M$_\odot$, reaching the Super Giant stage, the gravitational

contraction of the core raises the temperature to ignition of carbon burning. (Note that the $^{16}O(\alpha, \gamma)^{20}Ne$ is so slow that it will be bypassed.) It occurs mainly via $^{12}C(\alpha, \gamma)^{16}O$. The final (mass) frontier is 8 $M_\odot$ from which stars will complete all the following element burnings. However stars with a mass between 2.5 and 8 times the solar masses will evolve towards AGB stars similarly to the previous case. The difference is the content of the core since the products of carbon burning will also populate the inert core.

Is it all doom for white dwarves?

No. White dwarves can still accrete matter from a companion star which may be a main sequence star and eventually generate a nova event. This happens if both are close enough to form a binary system, and starts when the evolving star's radial expansion overpasses what is called the Roche lobe point (which, fundamentally, describes the mutual gravity field cancellation point). Then it is possible for the white star to capture its companion's outer layer material as its gravity field is stronger in this layer. The accreted matter mainly consists of hydrogen, but also contains He, CNO grains or even Al and Mg for more evolved, or younger, main sequence stars. It first forms an accretion disk around the star which eventually falls onto it, at which point it becomes degenerate. The newly formed layer on the white dwarf gets quickly heated up as the material does not expand due to its degeneracy. The temperature then becomes high enough that the cold (very slow) and the hot (very fast) CNO cycles are triggered successively. The hot CNO cycles powers an outward explosion in the outer layer releasing material into the interstellar medium while, at these temperatures, electrons are ejected out of their orbitals resulting in a UV flash (X-rays from lighter nuclei). The matter loses its degeneracy allowing the star to expand. Reactions in this work, at the energy they are studied, will only shed a feeble light on these phenomena.

Progenitor Mass $\gtrsim$ 8 $M_\odot$: Lead-up to Core Collapse Supernova

The star's next deepest layer burns the neon content, which was the main heavy product of the CNO cycle:

$$^{20}\mathrm{Ne} + \gamma \rightarrow ^{16}\mathrm{O} + \alpha \tag{2.4}$$

$$^{20}\mathrm{Ne} + \alpha \rightarrow ^{24}\mathrm{Mg} + \gamma. \tag{2.5}$$

The core is now formed of oxygen and magnesium whose burning forms silicon and a large quantity of alpha-particles and γ-rays. Incidentally, the final burning stage, silicon burning, consists mainly of an interplay of photodissociation and

α-capture that feed each other:

$$^{28}\mathrm{Si}(\gamma,\ \alpha)^{24}\mathrm{Mg}(\gamma,\ \alpha)^{20}\mathrm{Ne}(\gamma,\ \alpha)^{16}\mathrm{O}(\gamma,\ \alpha)^{12}\mathrm{C}(\gamma,\ 3\alpha) \tag{2.6}$$

$$^{28}\mathrm{Si}(\alpha,\ \gamma)^{32}\mathrm{S}(\alpha,\ \gamma)^{36}\mathrm{Ar}(\alpha,\ \gamma)^{40}\mathrm{Ca}(\alpha,\ \gamma)^{44}\mathrm{Ti}(\alpha,\ \gamma)^{48}\mathrm{Cr}(\alpha,\ \gamma)^{52}\mathrm{Fe}(\alpha,\ \gamma)^{56}\mathrm{Ni}. \tag{2.7}$$

This leads to the well known onion-like structure shown in Figure 2.4. The nuclear binding energy per nucleon maximises for ^{56}Ni, further fusion reactions are henceforth endothermic and the gravitational collapse of the star's material cannot be prevented by the release of nuclear fusion energy.

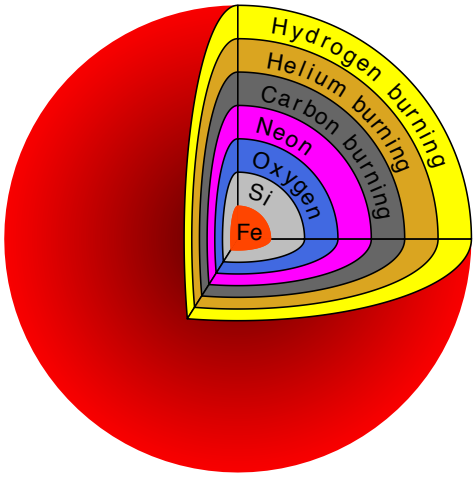

Figure 2.4: The onion-like structure of red giants before collapse of the core.

As such a star collapses, and the density grows in the core, elements in and around the iron core are rapidly photo-dissociated back to free protons, neutrons and α-particles. A significant number of protons convert to neutrons inside the core, resulting in a burst of electron neutrinos. Thermal production, and emission, of all neutrino flavours follows over the next few seconds (see, e.g., Refs. [Janka 2007, Magkotsios 2010]). This sequence of events, which had met much agreement within the astrophysics community, was further confirmed by observations of SN1987A (see Refs. [Bionta 1987, Chevalier 1992, Arnett 1989]).

2.1.3 Supernova explosion, synthesis of ^{44}Ti and relevance to the study of CCSNe

Modelling the physics of the supernova explosion is a task that has proven hard to realise, such that unravelling the underlying explosion mechanism of CCSNe has become a highly topical quest in modern astrophysics. The development of a neutrino wind appears as the most compelling theory [Janka 2007]. This wind would be strong enough that sufficient neutrino-nucleon interactions occur [Bethe 1985], powering the nuclear reaction network in the outer layer of the core.

The current situation is that models do not produce a robust explosion, and more problematic, models that produce an explosion in 1D or 2D, do not when

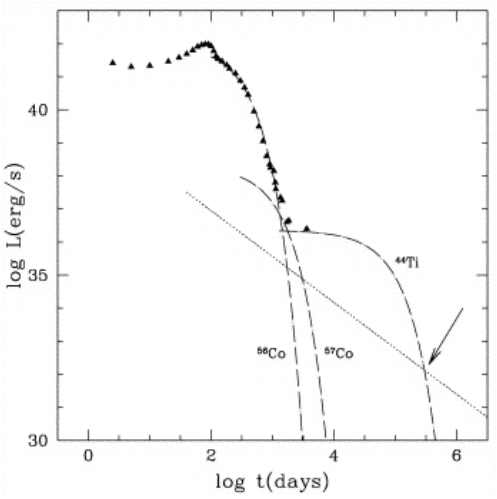

Figure 2.5: Light curves for SN 1987A. The triangles show the observed luminosity. Dashed lines represent the contribution from the decay of nuclei using model-based estimation of the ejecta content in ^{56,57}Co and ^{44}Ti, *i.e.* $M_{^{44}Ti} \approx 5\times10^{-5}M_{\odot}$. The dotted line denotes the calculated luminosity emitted by accretion on a putative black hole in SN 1987A. The arrow marks the time of the black hole emergence. Taken from Ref. [Zampieri 1998].

more realistic 3D calculations are performed along the same considerations made in 1D and 2D. However, there are still many avenues to explore that could in time help 3D models to produce robust explosions. For example, the breaking of the star's symmetry following the Si burning in the region just outside the iron core leads to better treatment of the titanic convection occurring in the star, and can greatly enhance the possibility of an explosion from neutrino heating, see Ref. [Couch 2015].

Validating any model for the CCSN explosion will however come from observations. Signatures such as light curves and (near)optical spectra show little sensitivity to the detail of the explosion mechanism. In contrast, γ-rays from the decay of ^{44}Ti have been observed from known CCSNe. Indeed the radionuclide ^{44}Ti is one of the very few cosmogenic nuclei to be observed in our Galaxy, and in particular from remnants of CCSNe. The γ-rays associated with the decay of ^{44}Ti have been observed from the type-II supernova SN1987A by the INTEGRAL IBIB/ISGRI instrument [Grebenev 2012]. This instrument previously detected this isotope from the type-IIb supernova Cassiopeia-A [Renaud 2006]. Traces of ^{44}Ti from Cassiopeia-A were further observed by the COMPTEL satellite [Iyudin 1994] and by BeppoSAX [Vink 2001]. As a result observations of γ-rays from the long lived isotope ^{44}Ti, τ=85.3(4) years [Ahmad 2006], ejected into the interstellar medium, might provide such sensitivity.

The ^{44}Ti nucleus is produced in α-rich regions. These regions are generated near the iron core when the quasi-static equilibrium between nuclear reactions and their inverse ceases [Magkotsios 2010] after the explosion, at a time where the star cools down. The deep, thermalised, core is doomed to evolve to a neutron star or a black hole, but how much of the newly produced ^{44}Ti would be caught in this fate is linked to the hydrodynamics of the star. As a result, the production

site of ^{44}Ti is very sensitive to the prediction of where the boundary between the material falling into the newly formed structure at the core and the material ejected into the interstellar medium is, this is known as the mass cut. The ^{44}Ti material that is expelled powers the luminosity of the remnant from about 2000 days after the explosion, and until accretion around the newly formed black hole takes over much later. In the case of SN 1987A, see Figure 2.5 and Ref. [Zampieri 1998], this means that since 2011 the luminosity has been driven by the β-decay of ^{44}Ti while it is expected that accretion around a (predicted but unconfirmed) black hole from the supernova's remnant will be the main source of luminosity around 300 years after the explosion, *i.e.*, near 2300 AD.

About X-ray bursts

A binary system such as that described earlier for novae may occur with neutron stars. The higher density of the neutron star makes it possible to quickly produce heavier nuclei resulting in higher energy X-rays than that generated in novae. Consequently they are called X-ray bursts, note that the neutron star's gravity is strong enough that no material is thought to be expelled in a X-ray burst [Schatz & Rehm 2006].

Existing CCSNe models predict that the maximal ejecta content in ^{44}Ti does not exceed 1×10^{-4}M$_\odot$, even assuming a wide range of progenitor models and masses [Timmes 1996, Magkotsios 2010, Tur 2010]. Observations, however, conducted by satellite-based γ-ray observatories, report significantly larger values. In the sequence of β-decays from ^{44}Ti to ^{44}Ca several γ-rays are emitted, at 68, 78 and 1157 keV, and are detectable in space. Combining the different observations of Cassiopeia-A, the estimated mass of ^{44}Ti ejected is $1.6^{+0.6}_{-0.3}\times10^{-4}$ M$_\odot$ [Renaud 2006] while observations of SN1987A indicate the presence of $(3.1\pm0.8)\times10^{-4}$ M$_\odot$ of ^{44}Ti in the ejecta. Note that recent observations from Cas-A with the NuSTAR space-based telescope reports an ^{44}Ti ejecta content of $1.25\pm0.3\times10^{-4}$ M$_\odot$, with the difference with the previous observation due to the asymmetry of the explosion, see Ref. [Grefenstette 2014]. The re-orientation of the telescope to SN1987A hinted at an even larger asymmetry in the explosion while the ^{44}Ti ejecta's content is measured at $1.5(3)\times10^{-4}$ M$_\odot$ [Boggs 2015], bringing the observations from Cas-A and SN1987A into agreement. Yet the latter amounts of ^{44}Ti are still higher than any theoretical model predictions. Age and/or distance determination for supernova remnants (SNRs) also critically depend on the amount of ^{44}Ti observed in the ejecta. An intriguing example lies in the observation of a previously unknown SNR located in the Vela region from the COMPTEL γ-ray data [Iyudin 1998]. Given the distance to this object, 200 pc, and a 'standard'

^{44}Ti yield of 5×10^{-5} $M_\odot$, the suggested age for the remnant was $\sim$700 years. For the relative proximity, and the period in history, it has been noted that it is somewhat surprising that no record of a corresponding supernova explosion observation exists.

It has been shown, in detailed studies by The *et al.* [The 1998] and Magkotsios *et al.* [Magkotsios 2010], that the nucleosynthesis of ^{44}Ti hinges upon a few reactions, the triple-α reaction, ^{40}Ca$(\alpha, \gamma)^{44}$Ti (producing ^{44}Ti) and ^{44}Ti$(\alpha, p)^{47}$V (consuming ^{44}Ti). Critically the final amount of ^{44}Ti depends most sensitively, by a significant margin, on the reaction rate for ^{44}Ti$(\alpha,\ p)^{47}$V. The later fact motivates the investigation of the cross section for this reaction and will be the subject of later Chapters.

Wolf-Rayet stars

Wolf-Rayet stars are extremely massive stars, $M_{\text{initial}} \gtrsim 25\ M_\odot$, that feature extremely violent environments. In particular mass loss due to convection and stellar wind leads to the ejection of the entire hydrogen envelope such that an observational specificity is the lack of hydrogen lines in the emission spectrum. However deeper layers containing He, C, Ne, or O may be exposed such that associated lines are also observed. However, the mass is so extreme that there is a high radiation pressure even in those deeper layers, sufficient for high stellar winds to expel all surface material (and some of the outmost layers) into the surrounding interstellar medium.

2.1.4 Overview: Figure 2.6

The final result of stellar evolution is presented in Figure 2.6 on which the pictures of the Horsehead nebula and the Crab nebula (with the Crab pulsar/neutron star at the centre) have been taken by NASA's Hubble Space Telescope; the picture of the Sun displays a solar eruption and was combined by NASA's Solar Terrestrial Relations Observatory and ESA/NASA's Solar and Heliospheric Observatory. The picture of Vega comes from NASA's Spitzer Space Telescope and is a mid-infrared spectroscopy therefore showing light from the debris around the star. Observations yielding the values for Vega's radius, mass and luminosity can be found in Ref. [Yoon 2010]. The image of Betelgeuse is from ESOs Very Large Telescope, the value for its radius comes from observations reported in Ref. [Bester 1996], its mass and luminosity have been taken from Ref. [Smith 2009]. The representation of SN1987A is an artist impression made from observations by ESO's Very Large Telescope which does show the structure of the two rings with

the remnant at the centre. Finally both the black hole and binary star images are made by NASA. NASA's images and pictures can be found on their website, www.nasa.org, ESO's images on www.eso.org. Wolf-Rayet stars have different possible fates (hence the dashed lines).

In Figure 2.6, the left to right horizontal axis can, for the main sequence, be seen as a proxy for the evolution of the surface temperature while the bottom/up axis would represent luminosity. This is better seen in a Hertzsprung-Russell diagram such as that of Figure 2.7.

How are supernovae classified?

An implicit feature of the above explanation is that the elements populating the surface of a star varies depending on which evolutionary path it follows. For example, a red giant's surface will mainly contain hydrogen and the light spectra of this star will exhibit lines at the corresponding absorption wavelength. But if the star is heavy enough that it evolves to a Wolf-Rayet star then the outer layer will be ejected into space by the strong stellar wind, and, as said earlier, a main feature of these stars would be an absence of the H absorption lines the light spectra. A natural classification of supernovae is then to separate those with hydrogen line in their spectrum (Type II) and those without (Type I). Similarly in thermonuclear runaways, such as those produced in binary systems, there will not be any H absorption lines, seeing as the white dwarf would have lost its hydrogen envelope due to stellar winds. However unlike Wolf-Rayet stars (Type Ib/c), novae (Type Ia) may exhibit a silicon absorption line as this element may be produced by the explosive nuclear fusion reaction.

2.1.5 Production sites of ^{26}Al, motivation for studying the (p, γ) destructive reaction

The low energy level structure of ^{26}Al is presented in Figure 2.8. It can be seen that the ground state is $J^{\pi} = 5^{+}$, its β-decay to the stable ground state of ^{26}Mg, $J^{\pi} = 0^{+}$, is therefore highly hindered and τ =10^{6} years. However, there is an isomer at 228.2 keV, with spin and parity 0^{+} which can decay to the ground state of ^{26}Mg much more effectively τ= 9 s. As a result, production of ^{26}Al is constrained to astronomical environments colder than T_9 =0.1 [Arnett 1996] where the temperature is low enough that most of ^{26}Al is in its ground state configuration. In terms of astronomical age the lifetime for ^{26g}Al is relatively short (about a tenth of hydrostatic H-burning time), such that the next constraint on which environment will be responsible for ^{26}Al production is how fast stellar winds appear in the star, in order to expel ^{26}Al from the star before the temperature is

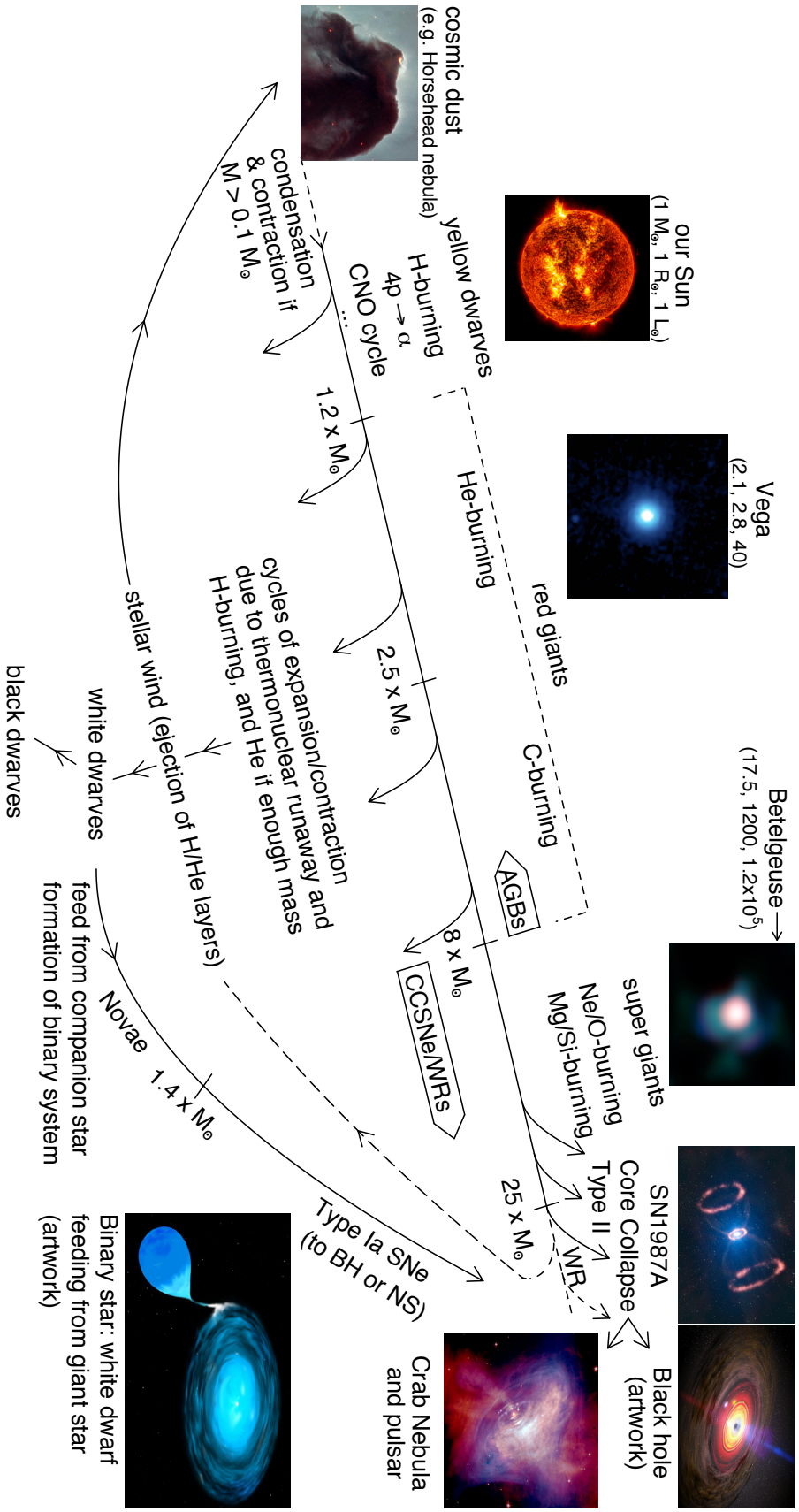

Figure 2.6: Diagram of stellar evolution showing some well known objects of the sky. A longer description with references can be found in the text.

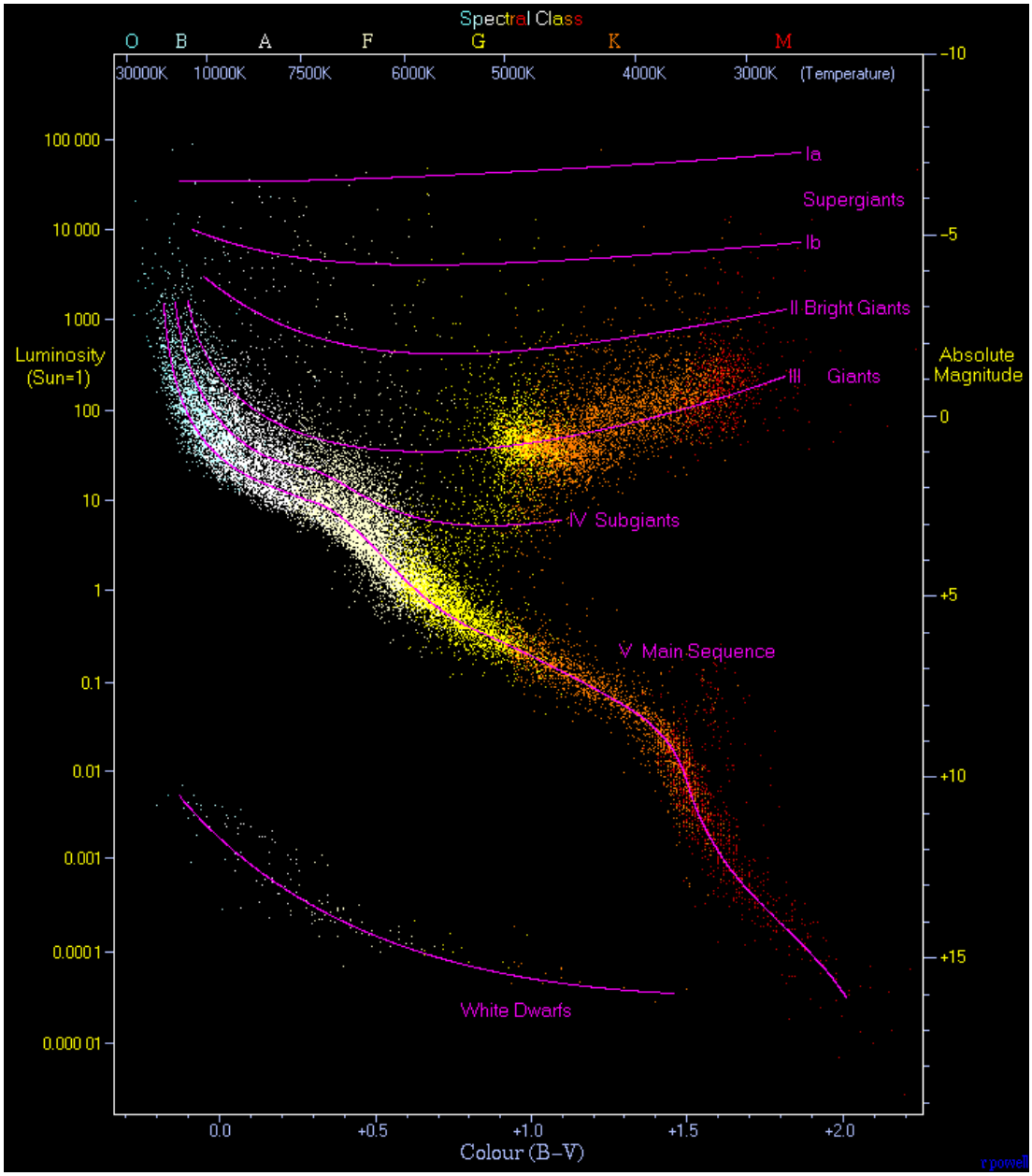

Figure 2.7: Hertzsprung-Russell diagram plotting data from the Hipparcos Catalogue and the Gliese Catalogue. It represents observational data as a spectrum colour (or surface temperature) against the apparent luminosity (or magnitude). The Sun is still on the main sequence however it will diverge from it as shown in Figure 2.6 in around 4 billion years. The diagram, arguably the best available online, is from wikipedia.

too high and the decay to ^{26}Mg can proceed via excitation to the isomer state and further rapid β-decay. Taking these considerations, explosive hydrogen burning that can occur at high temperature (T_9 >0.06) and density 10^3g/cm^3 is the main candidate for production of ^{26}Al, if the star contains seed nuclei with A$\gtrsim$20. The reaction network of explosive hydrogen burning responsible for ^{26}Al production in such condition is shown in Figure 2.8 and highlights the pivotal role of the destructive radiative proton capture reaction on ^{26}Al.

Observations support this hypothesis. Indeed, emissions of cosmic γ-rays throughout the interstellar medium (ISM) have been tracked and mapped by the latest generation of space-based telescopes, providing new insights into astrophysical processes occurring during the life cycles of stars [Grebenev 2012, Churazov 2014, Diehl 2014]. A first milestone was the detection by the HEAO-3 satellite of a diffuse γ-ray line in the equatorial plane of the Galaxy at 1.809 MeV, associated with the ground-state decay of ^{26g}Al into the 1.809 MeV 2^+ state in ^{26}Mg. This showed nucleosynthesis is an ongoing process in the Milky Way. However, because of the poor angular resolution and sensitivity of the instrument, no spatial information on the source of the 1.809 MeV emission line could be obtained [Mahoney 1982]. More recently, the COMPTEL and INTEGRAL satellite missions have been able to measure the distribution of the ^{26g}Al cosmic γ-ray line across the Milky Way [Diehl 2006, Diehl 1995, Wang 2009]. These studies measured overall abundances of ^{26}Al and reported that emission across the Galactic plane were irregular, indicating that ^{26}Al source regions corotate with the Galaxy. In turn this points to high-mass progenitors as the favoured production sites. In particular, galactic ^{26}Al is expected, as shown before, to be predominantly produced during the hydrogen burning phase of massive Wolf-Rayet (WR) stars, which pollute the ISM with the products of hydrogen burning via a strong stellar wind, or during the cataclysmic core collapse supernova phase [Diehl 2006]. Additional contributions to the observed Galactic abundance have been suggested to come from asymptotic giant branch (AGB) stars and classical novae [Siess & Arnould 2008, Jose 1997]. The existence of radioactive ^{26}Al in the Galaxy may also be traced through excesses of its daughter nucleus ^{26}Mg in meteoritic material. Excesses of ^{26g}Mg were found in calcium and aluminium inclusions of the Allende meteorite, inferring a relatively large ^{26}Al/^{27}Al ratio present in the Solar System at the time of its formation [Lee 1977]. A much-debated question relates to the origin of ^{26}Al in the early Solar System [Wasserburg 2006]. It has been suggested that energy released by in situ decay of ^{26}Al in protoplanetary disks orbiting young stars may cause melting of icy planetesimals, thereby influencing the conditions required of planetary systems to support life [Srinivasan 1999].

The elaboration of a clear scenario is currently hampered by the absence of critical nuclear reaction rates for the production and destruction of ^{26}Al in stellar environments [vanRaai 2008, Iliadis 2011]. In the case of hydrogen burning scenarios such as Wolf-Rayet stars and AGB stars, it is the uncertainties in the ^{26g}Al(p, γ)^{27}Si destruction reaction that dominate. A recent sensitivity study by Parikh *et al.* [Parikh 2014] has considered the importance of these uncertainties and has drawn attention to the need for experimental constraints on the rate of the ^{26g}Al(p, γ)^{27}Si reaction. However, difficulty primarily arises in this regard because ^{26}Al is radioactive. Direct (p, γ) measurements of a resonance at 189 keV have been made using both a radioactive target of ^{26}Al [Vogelaar 1989] and a radioactive ion beam of ^{26}Al [Ruiz 2006], reporting resonance strengths of 55(9) and 35(7) μeV, respectively. More recent spectroscopic studies of ^{27}Si indicate that a lower-energy resonance at 127 keV could play the dominant role in the destruction of ^{26}Al in Wolf-Rayet stars and AGB stars, where burning occurs at relatively low temperatures in the Gamow peak (T_9 ≈0.03–0.10) [Lotay 2009]. However, direct measurements of the reaction at this lower energy are not practicable with presently available ^{26}Al beam intensities, due to the rapid reduction in the cross section with beam energy below the Coulomb barrier, and an indirect approach is mandated to estimate the resonance strength. In earlier work, Vogelaar *et al.* [Vogelaar 1996] used a radioactive target of ^{26}Al to perform a ^{26}Al(^{3}He, d)^{27}Si transfer reaction study. However, there were large impurities of ^{27}Al ($> 90\%$) in the target, and only upper limits could be placed on the strength of the relevant resonances [Vogelaar 1996].

In a recent paper by Parikh *et al.* [Parikh 2014], the effect of a range of possible strengths from 0 to 1 μeV (which would correspond to an almost pure single particle state) for the 127 keV resonance on ^{26}Al nucleosynthesis was considered. By using the complete range of values for the 127 keV ^{26g}Al(p, γ)^{27}Si destruction resonance, Parikh *et al.* found variations in the synthesised abundance of ^{26}Al in AGB stars by up to a factor of 6, as well as even up to 40% in novae, which are relatively high-temperature astrophysical environments (T_9 = 0.1–0.4). Furthermore, an additional sensitivity study of the effect of the ^{26g}Al(p,γ)^{27}Si reaction rate variations for $T_9 < 0.05$ by Iliadis *et al.* [Iliadis 2011] found that an increase in the rate by a factor of 100, corresponding to a 127 keV resonance strength of ≈1 μeV, would result in a reduction in the amount of ^{26}Al synthesised by a factor of ≈300. This highlights the need for tightening the experimental investigation of the (p, γ) destructive radiative proton capture reaction on ^{26}Al. In this work, using theoretical models for mirror nuclei (here $^{27}_{13}$Al^{14} and $^{27}_{14}$Si^{13}), these will be developed in the following chapter, understanding of this reaction is obtained

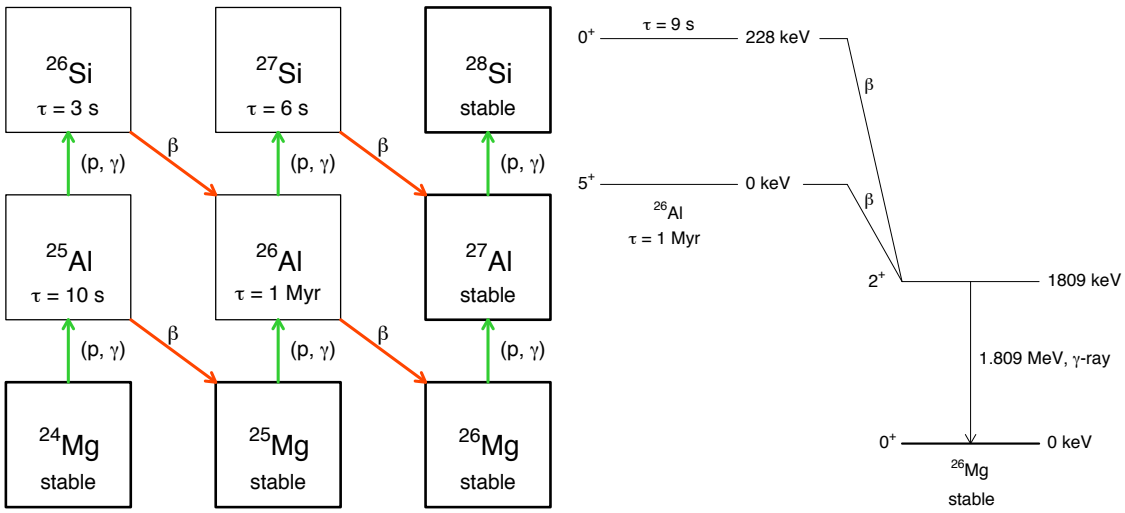

Figure 2.8: (right) Reaction network, in explosive and hydrostatic H-burning phases, responsible for the production and destruction of ^{26}Al; (right) and low energy level structure and β-decay of ^{26}Al.

using the ^{26}Al$(d, p)^{27}$Al neutron capture.

Consequently, in this thesis, the stellar sites of interest are found in different places of the summary diagram shown in Figure 2.6, namely AGB and WR stars and the experimental investigation will be conducted in an energy region that will allow conclusions to be drawn for the destruction rate of ^{26}Al in these environments.

Chapter 3

Theoretical models for the study of nuclear reactions in astrophysical environments

This chapter first presents the theoretical background for the study of nuclear reactions in stars. This is relevant for both reactions studied in this thesis, ^{26}Al(p, γ)^{27}Si via ^{26}Al(d, p)^{27}Al, and ^{44}Ti(α, p)^{47}V. The second part of this chapter, however, focuses on the theory of transfer reactions and leads to the definition of nucleon spectroscopic factors and, to a lesser degree, asymptotic normalisation coefficients. This later part also contains a description of the numerical approach used to calculate the wave function of the outgoing proton in the ^{26}Al(d, p)^{27}Al reaction.

3.1 Nuclear physics in violent hydrodynamic scenarios

3.1.1 Introduction to stellar cross section rates

In stellar evolution, the star proceeds, as seen in the previous chapter, through different stages of non-degenerate thermodynamic equilibrium in which the (fully ionised) plasma of nuclei and electrons can be considered as a perfect gas following the Maxwell Boltzmann's distribution, which can be expressed at temperature of the star T:

$$\phi(v) = 4\pi v^2 \left(\frac{m}{2\pi k_B T}\right)^{3/2} \exp\left(-\frac{mv^2}{2k_B T}\right), \tag{3.1}$$

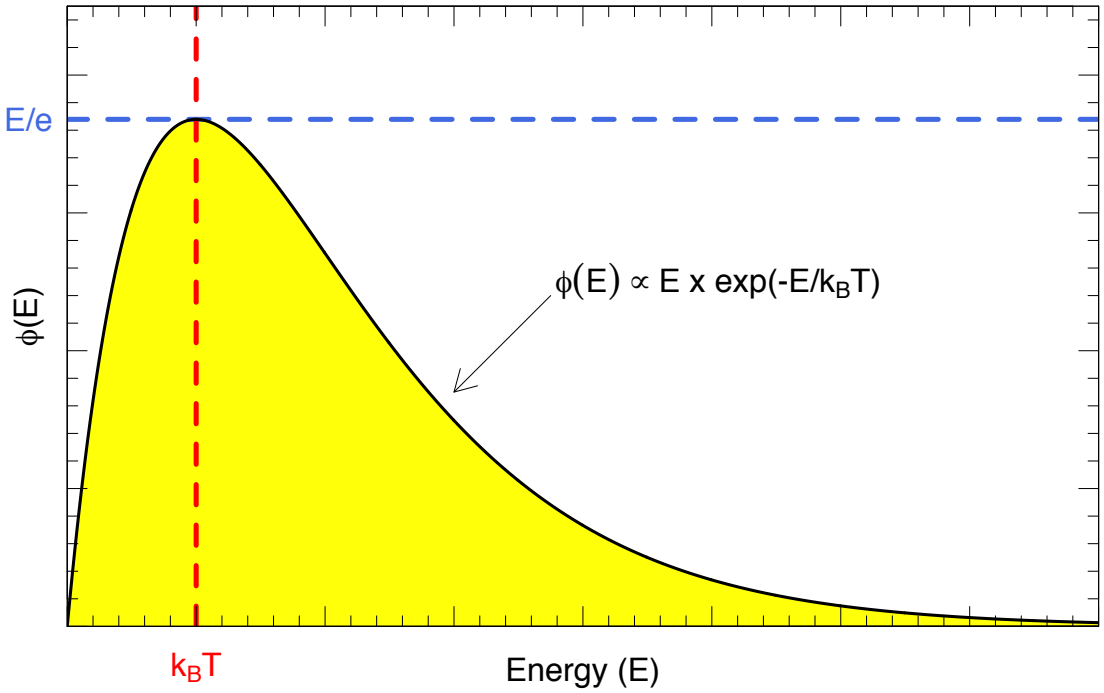

Figure 3.1: Representation of the Maxwell-Boltzmann distribution that depicts the cross section behaviour with energy.

where ϕ represents the particles velocity distribution given v, the relative velocity of the particles, μ, the reduced mass, N_A, Avogadro's mass, and k_B, the Boltzmann's constant. Using the kinetic energy, E, of the particle:

$$E = \frac{mv^2}{2}, \tag{3.2}$$

Equation 3.1 can also be written as:

$$\phi(E) = \sqrt{\frac{m}{k_B T}} \times \sqrt{\frac{2}{\pi}} \times E \exp\left(-\frac{E}{k_B T}\right). \tag{3.3}$$

A standard Maxwell-Boltzmann's distribution is shown in Figure 3.1 where it can be seen that the distribution of energies peaks for $E = k_B T$. Now consider the reaction of two particles such that:

$$a + A \rightarrow b + B. \tag{3.4}$$

The reaction rate between a and A is, the the product of the relative velocity distribution and the cross section at the corresponding energy. The rate of the

two particles reacting at that energy is then:

$$\langle \sigma v \rangle = N_a N_A \times \int_0^\infty v \phi(v) \sigma(v) \mathrm{d}v, \tag{3.5}$$

which becomes, following the above discussion:

$$N_A \langle \sigma v \rangle = N_A \left(\frac{8}{\pi \mu m_N (k_B T)^3} \right)^{1/2} \int \sigma(E) E \exp\left(-E/k_B T\right) \mathrm{d}E. \tag{3.6}$$

In stars, particles fuse at velocities below those necessary to overcome the electromagnetic repulsion that exist between them. They fuse at sub Coulomb energies (below the "barrier"), via quantum tunnelling, where the cross section may be approximated as follows:

$$\sigma(E) \propto \exp(-2\pi\eta)/E, \tag{3.7}$$

where η is the Sommerfield parameter:

$$\eta = \frac{Z_a Z_A e^2}{\hbar v}, \tag{3.8}$$

and Z_1 and Z_2 the atomic number of a and A. Consequently the combination of the cross section behaviour, vanishing at high energies, and the velocity distribution of the particles in the star at temperature T, very low at low energies, creates what is called the Gamow window, shown in Figure 3.2. Note that the Gamow window peaks at energy E_0 that can be determined using the dependency of the cross section given in Equation 3.7 into the reaction rate of Equation 3.6:

$$E_0 = \left\{ \pi \frac{Z_a Z_A e^2}{\hbar c} k_B T \sqrt{(\mu m_N c^2/2)} \right\}^{2/3} \tag{3.9}$$

$$\approx 0.122 \mu^{1/3} (Z_a Z_A T_9)^{2/3} \text{ MeV}. \tag{3.10}$$

The window's width is obtained by taking the difference of the energy values at which the distribution is $1/\exp(1)$:

$$\Delta E_0 \approx 0.237 (Z_a Z_A \mu T_9^5)^{1/6} \tag{3.11}$$

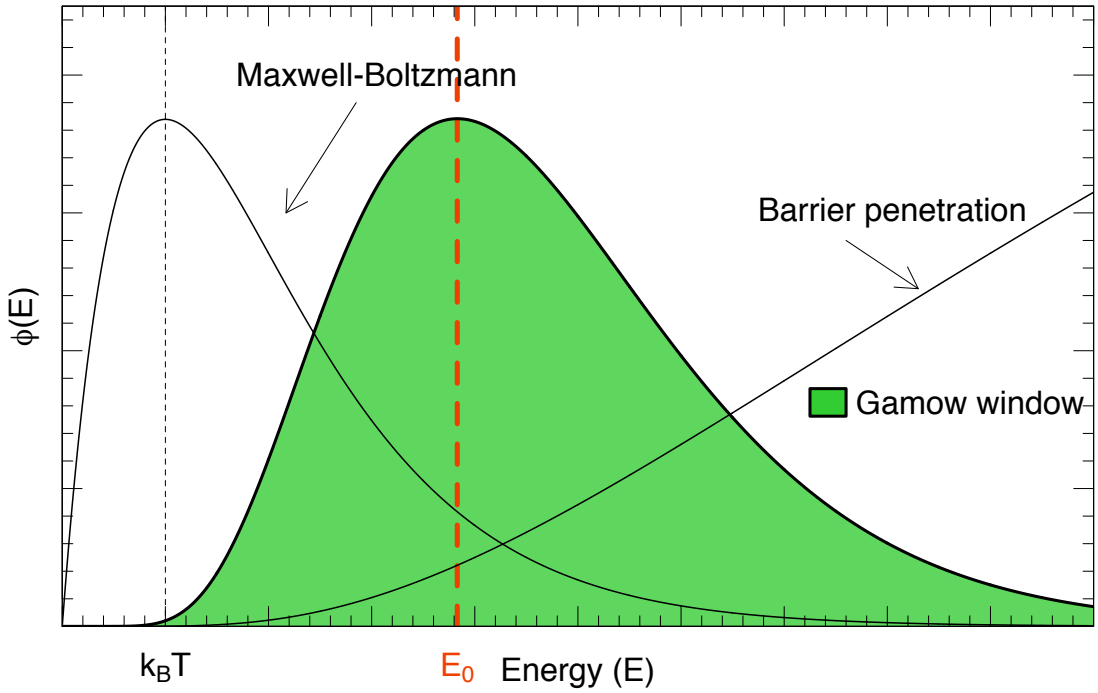

Figure 3.2: Combination of the Maxwell-Boltzmann distribution for the cross section and of the probability to penetrate through the Coulomb barrier with energy resulting in the so-called Gamow window.

3.1.2 The effect of resonances in stellar reaction rates

Resonances occur when the compound nucleus, C, in the fusion of a and A survives in an excited state, above the threshold for spontaneous emission of a which is the separation energy S_a, before decaying to two species b and B:

$$a + A \rightarrow C^*(E_x > S_a) \rightarrow b + B. \tag{3.12}$$

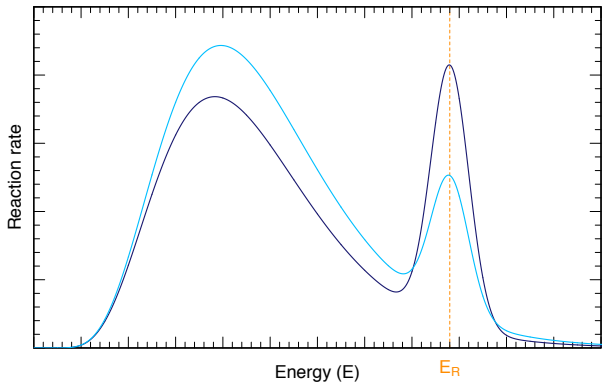

Figure 3.3: Effect of a narrow resonance on a reaction rate. The lighter blue curve shows the effect at a lower star temperature than the darker blue curve.

Assuming, for simplicity, that the heavy nucleus B is formed in its ground state, the difference with a direct reaction is the energy and the width of particle b, those are linked to the resonance energy and width in C. Competitive decay paths from C^* must exist, albeit possibly at an extremely low branching ratio, unsuited for measurements, such as γ-ray decay to the ground state if allowed. In

a first order approach, taking the general case where the resonance energy E_R is higher than E_0 (the Gamow window maximum),[1] see Figure 3.3, but that $E_R \gg \Gamma$, the cross section can be described by the Breit-Wigner formula:

$$\sigma_R(E) = \frac{\pi}{\sqrt{2\mu E}} \times \frac{2J+1}{(2j_a+1)(2j_b+1)} \times \frac{\Gamma_a \times \Gamma_b}{(E-E_R)^2 + \Gamma^2/4}, \tag{3.13}$$

where Γ_a and Γ_b are the width of the entrance and exit channel, respectively, j_a and j_b the spin of the entrance and exit channel, respectively, J the spin of the resonance which by angular momentum conservation obeys:

$$\overrightarrow{J} = \overrightarrow{j_a} + \overrightarrow{j_b} + \overrightarrow{\ell_{a \leftrightarrow A}}, \tag{3.14}$$

where the $\overrightarrow{\ell_{a \leftrightarrow A}}$ is the orbital angular momentum between the reacting species a and A. Equation 3.13 can be inserted into Equation 3.6 as follow:

$$N_A \langle \sigma v \rangle_R = N_A \left(\frac{8}{\pi \mu m_N (k_B T)^3} \right)^{1/2} \int_0^\infty \sigma_R(E) E \exp\left(-E/k_B T\right) \mathrm{d}E \tag{3.15}$$

$$= N_A \left(\frac{2\pi}{\mu m_N k_B T} \right)^{2/3} \hbar^2 \times \frac{2J+1}{(2j_a+1)(2j_b+1)} \tag{3.16}$$

$$\times \int_0^\infty \frac{\Gamma_a \Gamma_b}{(E-E_R)^2 + \Gamma^2/4} \exp\left(-\frac{E}{k_B T}\right) \mathrm{d}E, \tag{3.17}$$

if the resonance is narrow enough, $E_R \gg \Gamma$, this further reduces to:

$$N_A \langle \sigma v \rangle_R = N_A \left(\frac{2\pi}{\mu m_N k_B T} \right)^{2/3} \hbar^2 \omega\gamma \exp\left(-\frac{E_R}{k_B T}\right). \tag{3.18}$$

The factor $\omega\gamma$ is the resonance strength:

$$\omega\gamma = \frac{2J+1}{(2j_a+1)(2j_b+1)} \times \frac{\Gamma_a \times \Gamma_b}{\Gamma_a + \Gamma_b}, \tag{3.19}$$

The dependency of Equation 3.18 on the star's temperature T is shown in Figure 3.3. Usually one reaction has several resonances that are narrow and isolated then their contribution to the reaction rate is simply summed:

$$N_A \langle \sigma v \rangle_R = N_A \left(\frac{2\pi}{\mu m_N k_B T} \right)^{2/3} \hbar^2 \sum_i (\omega\gamma)_i \times \exp\left(-\frac{E_{Ri}}{k_B T}\right). \tag{3.20}$$

In this work, two types of reactions are investigated: (α, p) and (d, p), the latter

[1] Note that the case $E_R \approx E_0$ will not be discussed here.

one being used as an indirect method for studying a (p, γ) reaction, this will be explained in more detail below. However, only the (d, p) reaction is aimed at studying individual resonances. The ^{44}Ti(α, p)^{47}V reaction has too low a yield to allow for the study of potential resonances and, as will be shown in later sections, establishing experimental procedures for investigating potential resonances in ^{48}Cr, is delicate. In the following the focus is therefore on (p, γ) and (d, p) reactions.

Going back to Equation 3.19 for the resonance strength, it is obvious that if one of the decays, *e.g.* the decay to the b channel (which is the exit channel) highly dominates, $\Gamma_b \gg \Gamma_a$, the width factor in Equation 3.19 is reduced to Γ_a. For example for a γ-ray decay, the standard mean time of $\approx 10^{-15}$ s, corresponding to the unhindered electromagnetic period, results in a γ-ray partial width of $\Gamma_\gamma = \hbar/\tau \approx 1$ eV. Note that hindrance results in longer lifetimes and will lower the width.

In the (p, γ) reactions that occur in stars, resonances lie above the particle emission threshold which means that the γ-ray branching ratio is extremely low as the proton decay is evidently favoured, the resonance width provides a window for γ-ray decay to "go" and thus for creation of the nucleus in its ground state. The resonance strength is therefore controlled by the proton width:

$$\omega\gamma = \frac{\Gamma_p \times \Gamma_\gamma}{\Gamma_p + \Gamma_\gamma} = \omega\Gamma_p. \tag{3.21}$$

In the case of an odd-Z nucleus, such as $^{27}_{13}$Al, it is considered that the decay is due to the behaviour of the single odd-proton in a spherical field generated by the $A-1$ nucleons. Then consider a nucleus with A nucleons and angular momentum ($I_A M_A$) where M_A is the z-projection of I_A. To describe this system as a sum of a nucleus with $A-1 = A_-$ particles and an orbiting valence nucleon x (p or n), the angular momentum of A_- ($i_{A_-} m_{A_-}$) and x ($i_x m_x$) must be such that:

$$m_{A_-} + m_x = M_A \tag{3.22}$$

$$\text{and } |i_{A_-} - i_x| \leqslant I_A \leqslant i_{A_-} + i_x. \tag{3.23}$$

Consequently the wave function for A, in this model and using the isospin formalism of indistinguishable nucleons, may be represented by the sum of all possible combinations of $m_{A_{-1}}$ and m_x that respect those requirements:

$$\psi_{IM}(A_-, x) = \sum_{m_{A_-} m_x} \left\{ j_{A_-} j_x m_{A_-} m_x | IM \right\} \left[\phi_{j_{A_-} m_{A_-}}(A_-) \otimes \phi_{j_x m_x}(x) \right], \tag{3.24}$$

where the coefficients $\left\{j_{A_-} j_x m_{A_-} m_x | IM\right\}$ are the so-called Clebsch-Gordan coefficients that represent the overlap between A and $(A_- + x)$ ($\phi(A_-)$ and $\phi(x)$ are orthonormal):

$$\left\langle \left[\phi_{j_{A_-} m_{A_-}}(A_-) \otimes \phi_{j_x m_x}(x)\right] | \psi_{IM}(A_-, x) \right\rangle = \left\{j_{A_-} j_x m_{A_-} m_x | IM\right\}. \tag{3.25}$$

It is now obvious that $\left\{j_{A_-} j_x m_{A_-} m_x | IM\right\}^2$ is the associated probability of the overlap. For simplicity Clebsch-Gordan coefficients will be written as $C_{A_- x}$ in the following.[2] The application of this picture to the case of the (p, γ) reaction results in that the width Γ_p can be rewritten:

$$\Gamma_p = C^2_{p\gamma} S \times \Gamma_{s.p.}, \tag{3.26}$$

where $\Gamma_{s.p.}$ represent the width of the single-particle decay in a shell model picture. S is the single-particle spectroscopic factor which arises in the normalisation of the one-nucleon wave function: for a given N-body system, the normalised wave function $\widetilde{\phi}(N)$ can be written:

$$\widetilde{\phi}^m_{n\ell j}(N) = \sqrt{\frac{S}{N}}\, \phi^m_{n\ell j}(N). \tag{3.27}$$

The normalisation factor reduces to $\sqrt{S}$ in the case of a one-nucleon wave function. The factor $C^2_{p\gamma} S$ is called proton spectroscopic factor. It is sometimes abbreviated to $S^p_{\ell j}$ as it depends on the momentum transfer ℓ and the spin of the proton $\overrightarrow{j} = \overrightarrow{\ell} + \overrightarrow{s}$. The single-particle width $\Gamma_{s.p.}$ can be written [Lane 1960]:

$$\Gamma_{s.p.} = 2\frac{\hbar^2}{\mu a_c^2} P_c \theta^2_{s.p.}, \tag{3.28}$$

where μ is the system reduced mass, a_c the interaction radius, P_c the penetrability factor and $\theta_{s.p.}$ is the (dimensionless) single-particle reduced width:

$$\theta^2_{s.p.} = \frac{a_c}{2}\left(\phi^m_{n\ell j}(a_c)\right)^2. \tag{3.29}$$

[2] In case of non-isospin formalism the Clebsch-Gordan coefficients are replaced by coefficient of fractional parentage, see, for example, Ref. [Lawson 1980]

3.2 Mirror nuclei: the isospin quantum number and introduction of the (d, p) reaction

The idea that the behaviour of nuclei is governed by a charge independent strong interaction leads to the concept that the proton and the neutron may be seen as two different states of the same particle, the nucleon. Experimental evidence have long supported this concept, to a certain level this concept, with, for example [Henley 1969]:

$$\frac{\mathcal{V}_{nn} - \mathcal{V}_{pp}}{\frac{1}{2}(\mathcal{V}_{nn} + \mathcal{V}_{pp})} = 0 \pm 0.8\%, \tag{3.30}$$

where $\mathcal{V}_{nn}$ represents the strong interaction potential between two neutrons and $\mathcal{V}_{pp}$ that is formed in the exclusive presence of two protons. Consequently a fifth coordinate, the isospin, t_z, taking the value $+1/2$ for a neutron and $-1/2$ for a proton is introduced. Then one can derive the isospin quantum number $T_z = (N - Z)/2$. A classic use of the isospin is for the consideration of so-called "mirror nuclei", which have the same mass A (they are isobars) but exchanged numbers of protons and neutrons. Isospin symmetry is mainly broken by the electromagnetic interaction, since one nucleus in the pair of mirrors will have more protons resulting in a lowering of the energy of its level structure compared to the neutron rich mirror. Typical examples are the mirror nuclei ^{27}Al ($Z = 13$) and ^{27}Si ($Z = 14$) in which most of the states with a given J^π in one nucleus are observed in the other, with a very similar level structure, with similar branching ratios measured. For the present case it was shown in detail by Lotay *et al.* [Lotay 2011], see Figure 3.4. The later study was critical for the investigation of the properties of nuclear states in ^{27}Si in astrophysical environment. Indeed the study of the resonances driving the reaction of interest, the proton radiative capture ^{26}Al(p, γ)^{27}Si, is massively hampered by the dramatic lowering of the cross section for beam energies well below the electromagnetic repulsion (the Coulomb barrier) between the two reacting species. This is where the mirror nuclei approach, coupling to the findings of Lotay *et al.*, proves powerful, as it provides a means to obtain the nuclear properties, in particular the spectroscopic factors, of the (proton unbound) resonances in the ^{26}Al+p system by studying those values for neutron bound mirror states of ^{27}Al=^{26}Al+n. It has been shown indeed that the C^2S for mirror analog states are expected to agree to within 20% [Timofeyuk 2003, Timofeyuk 2006]. This, thanks to experimental developments that will be explained in Chapter 4, can be performed using the ^{26}Al(d, p)^{27}Al transfer reaction.

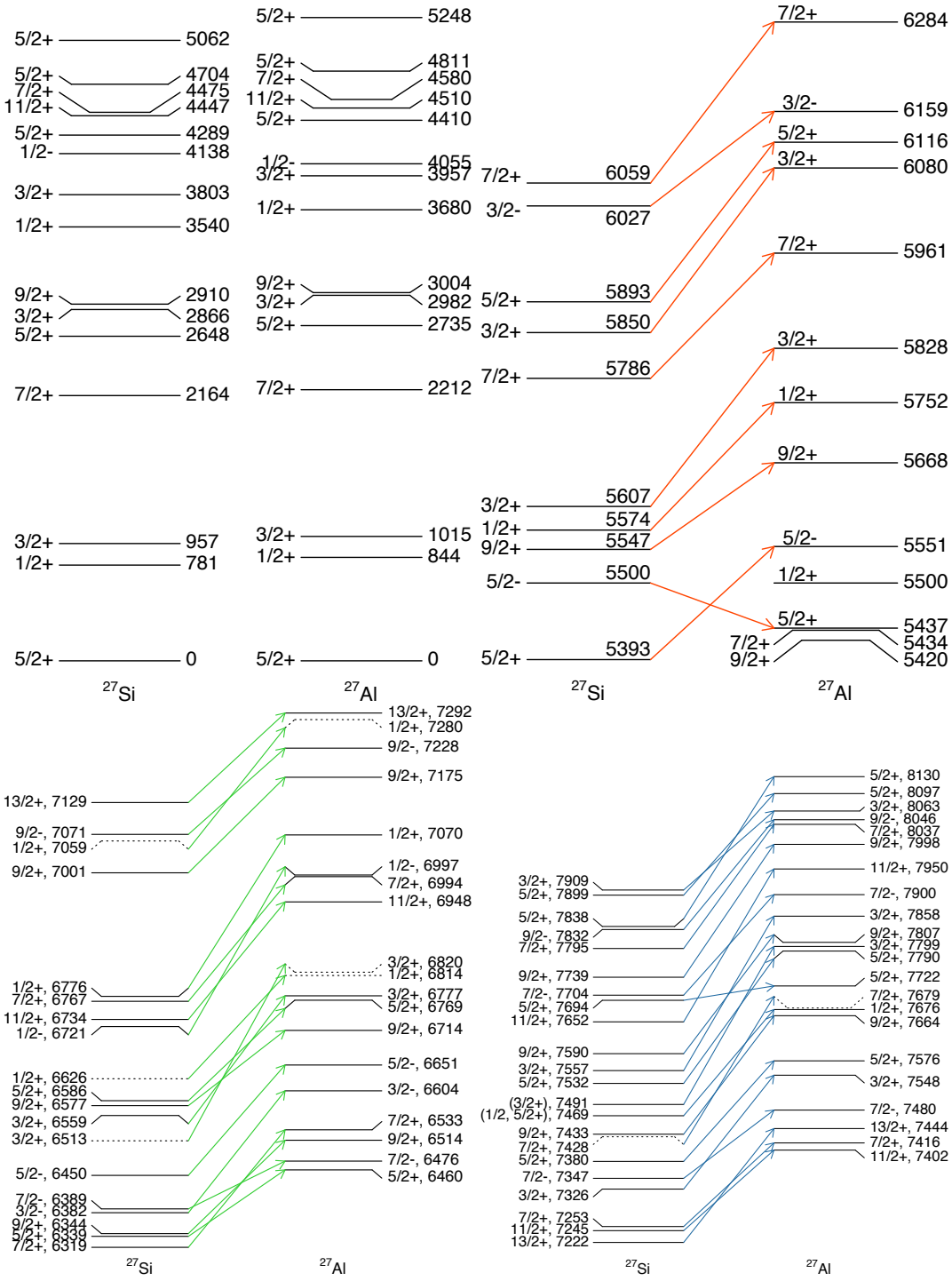

Figure 3.4: Level structures of ^{27}Si and ^{27}Al, mirror nuclei with 14 and 13 protons, respectively. The assignment of mirror states above 5 MeV, symbolised by the arrows, is from Ref. [Lotay 2011].

3.3 Transfer reactions

The spectroscopic factor, C^2S, may be extracted from a transfer reaction experiment and theory as follows:

$$\left.\frac{\mathrm{d}\sigma}{\mathrm{d}\Omega}\right|_{exp.} = C^2S \times \left.\frac{\mathrm{d}\sigma}{\mathrm{d}\Omega}\right|_{th.}. \tag{3.31}$$

In this section, the theory of the transfer cross section is presented first. Thereafter, different approaches for the calculation of the theoretical differential cross section are discussed with the use of the code `TWOFNR`. Finally the latter code will be used to discuss previously published data from (d, p) and (p, d) reactions and guidance for analysing the ^{26}Al(d, p)^{27}Al experiment.

3.3.1 Theory of the (d, p) transfer reactions

Theoretical description of the transfer cross section

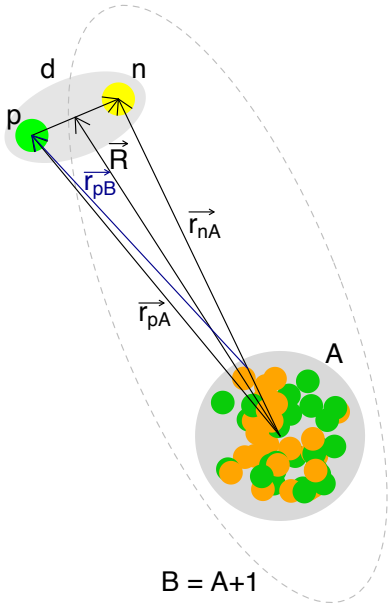

Figure 3.5: Representation of the vectors used in the present section. Note that the origin centre of has been shifted for clarity as it would nearly overlap.

In order to describe the reaction process, consider the reaction A(d, p)B. The deuteron wave function in the entrance channel may be written as:

$$\psi^{(+)}_{d,\,\vec{k}_d} = \exp(\imath\,\vec{k}^{(+)}_d.\vec{r}), \tag{3.32}$$

where $k^{(+)}_d$ is the deuteron wave number. After the reaction has occurred at long distance ρ, using the fact that the interaction potential is short range, the deuteron wave function may be written as:

$$\psi^{(-)}_{d,\,\vec{k}^{(-)}_d} \propto \exp(\imath\,\vec{k}^{(+)}_d.\vec{\rho}) - \vartheta_\ell(\theta) \times \frac{\exp(\imath\,\vec{k}^{(-)}_d.\vec{\rho})}{\rho}, \tag{3.33}$$

where θ is the scattering angle. Consequently the ℓ-integrated cross section may be written as:

$$\frac{1}{N}\sigma(\theta) \propto \sum_\ell (2\ell+1)(1-|\vartheta_\ell(\theta)|^2) = \sum_\ell (2\ell+1)\,|T_\ell(\theta)|^2\,, \tag{3.34}$$

where N is the number of neutrons of the target A. It is indeed assumed here that all neutrons contribute equally to the final cross section. The transmission coefficient $T_\ell(\theta)$ can also be

expressed by considering the overlap between the entrance and exit channel:

$$T_\ell = \left\langle \chi_p^{(-)} \Phi_B \right| \mathcal{V}_{(d,\ p)} \left| \psi_d^{(+)} \Phi_A \right\rangle, \tag{3.35}$$

where $\chi_p^{(-)}$ represents the exit channel proton wave function, and $\mathcal{V}_{(d,\ p)}$ the transfer operator. It can be noted here that since B has one less neutron compared to A ($\Phi_A = \Phi_B \otimes \phi_n$), the overlap between entrance and exit channel in the development of Equation 3.35 contains implicit structure information, the (neutron) spectroscopic factor. Consequently the transmission coefficient can be rewritten:

$$T_\ell = \sqrt{S_\ell^n} \times \left\langle \chi_p^{(-)} \right| \mathcal{V}_{(d,\ p)} \left| \psi_d^{(+)} \right\rangle = \sqrt{S_\ell^n} \times \widetilde{T}_\ell. \tag{3.36}$$

This input may be deduced experimentally as shown in Equation 3.31. $\mathcal{V}_{(d,\ p)}$ can be expressed *prior* to the reaction as $\mathcal{V}_p(\overrightarrow{r_{pA}}) + \mathcal{V}_n(\overrightarrow{r_{nA}}) - \mathcal{U}_{prior}$ and in the aftermath of the reaction (*post*) as $\mathcal{V}_p(\overrightarrow{r_{pB}}) + \mathcal{V}_n(\overrightarrow{r_{nA}}) - \mathcal{U}_{post}$, where $\mathcal{U}_{prior}$ and $\mathcal{U}_{post}$ are optical potentials that are used to generate $\chi_p^{(-)}$ and $\psi_d^{(+)}$. The vector parametrisation is represented in Figure 3.5.

Representing potential $\mathcal{V}_{(d,\ p)}$ and the entrance and exit wave functions

To calculate the transfer amplitude of Equation 3.35, the potential $\mathcal{V}_{(d,\ p)}$ representing the interactions that takes place in the reaction must be expressed. In the entrance channel, there are 2(+1) entities to consider. The target A, and the deuteron d, which is made of one proton and one neutron. Consequently the representation requires, at least, a potential for the target $\mathcal{V}_A$, for the deuteron $\mathcal{V}_d$, and for the the interaction $d \leftrightarrow A$, $\mathcal{V}_{dA}$. There are two different approaches to the problem of representing the deuteron and its interaction with the target. Historically, the distorted wave - Born approximation (DWBA) method was used, however, more recently, the adiabatic wave approximation (ADWA) has been developed and is now the preferred method. Schematically the difference between those two approaches of the entrance channel is shown in Figure 3.6. In the DWBA method the scattering is only between the target A and deuteron d such that there is only one coordinate $\overrightarrow{R}$ corresponding to the interaction distance (in the centre of mass) between the deuteron and A. Consequently there is no more $\mathcal{V}_p(\overrightarrow{r_{pA}})$ and $\mathcal{V}_n(\overrightarrow{r_{nA}})$. The entrance channel wave function is written:

$$\psi_d^{(+)}(\overrightarrow{r},\ \overrightarrow{R}) = \chi_d^{(+)}(\overrightarrow{R})\phi_d(\overrightarrow{r}), \tag{3.37}$$

such that the the action of the deuteron Hamiltonian $\mathcal{H}_d$ are on the unique deuteron wave function ϕ_d is:

$$\mathcal{H}_d|\phi_d\rangle = -\epsilon_d|\phi_d\rangle, \tag{3.38}$$

where ϵ_d is the bounding energy of the deuteron. The DWBA transfer amplitude becomes:

$$\widetilde{T}_\ell^{\,DWBA} = \left\langle \chi_p^{(-)} \,\middle|\, \mathcal{V}_{(d,\ p)} \,\middle|\, \chi_d^{(+)}(\overrightarrow{R})\phi_d(\overrightarrow{r}) \right\rangle. \tag{3.39}$$

What is needed to express the $\mathcal{V}_{prior}$ is:

- a distorted potential to describe the $d \leftrightarrow A$ interaction: $\mathcal{V}_{dA}(\overrightarrow{R})$, and,
- a binding potential for the deuteron $(p+n)$.

In the exit channel $\mathcal{V}_{post}$ requires

- a distorted potential to describe the $p \leftrightarrow B$ interaction: $\mathcal{V}_p(\overrightarrow{r_{pB}})$,
- a nucleus nucleus interaction for $p \leftrightarrow A$, and,
- a binding potential for the newly formed $(n+B)$.

In the ADWA approach, the break up of the deuteron is considered, therefore the two scattering centres are considered and the incoming wave function may be approximated as:

$$\psi_d^{(+)}(\overrightarrow{r},\ \overrightarrow{R}) = \chi_d^{(+)}(\overrightarrow{R})\phi_d(\overrightarrow{r}) + \sum_{i=(p,\ n)} \chi_i^{(+)}(\overrightarrow{R})\widehat{\phi}_i(\overrightarrow{r_i}), \tag{3.40}$$

since p and n must stay within the deuteron boundary (that is even if the energy of the transferred neutron, n^*, is such that the constructed deuteron from $d^* = p + n^*$ is unbound, it must still be in a continuum coupled to the ground state of the deuteron) the $\widehat{\phi}_i$ are constrained to $|\overrightarrow{r_i}| \leqslant \left|\overrightarrow{R}\right|$. This means that the wave functions vanish at the point of examination of the entrance channel (*prior*) and exit channel (*post*), because those methods look for overlap of the tail of the wave functions at large radii. Nevertheless, considering the break up of the deuteron into a proton and a neutron, means that the action of the deuteron Hamiltonian $\mathcal{H}_d$ on the deuteron wave function ϕ_d is decomposed into a global action on the $(p+n)$ system:

$$\mathcal{H}_d|\phi_d\rangle = -\epsilon_0|\phi_d\rangle, \tag{3.41}$$

and secondary actions on the individual constituents:

$$\mathcal{H}_d|\widehat{\phi}_i\rangle = -\widehat{\epsilon}_i|\widehat{\phi}_i\rangle, \tag{3.42}$$

where the $\hat{\epsilon_i}$ are the energies of p and n. In the adiabatic approach, the $\widehat{\epsilon_i}$ are ignored and $\mathcal{H}_d$ is replaced by ϵ_d, such that there is no method-inherent gain of energy in the deuteron system by considering the break up (hence the method is "adiabatic"). Consequently building $\mathcal{V}_{prior}$ requires:

- a distorted potential to describe the $p \leftrightarrow A$ interaction: $\mathcal{V}_{pA}(\overrightarrow{R})$,
- a distorted potential to describe the $n \leftrightarrow A$ interaction: $\mathcal{V}_{nA}(\overrightarrow{R})$, and,
- a method to construct the adiabatic deuteron potential from the two above distorted potentials.

(Note that $\mathcal{V}_{post}$ remains the same as in the DWBA method). The adiabatic deuteron potential is written:

$$\mathcal{V}_d^{adiab.} = \int \left\{ \mathcal{V}_n(\overrightarrow{r_{nA}}) + \mathcal{V}_p(\overrightarrow{r_{pA}}) \right\} \delta(\overrightarrow{r}).\mathrm{d}\overrightarrow{r}, \tag{3.43}$$

where $\delta(\overrightarrow{r})$ is the Kronecker symbol. Thus for a zero range approximation the adiabatic potential is just $\mathcal{V}_{pA}(\overrightarrow{R}) + \mathcal{V}_{nA}(\overrightarrow{R})$, *i.e.*, the proton and neutron optical potentials are evaluated at the same point. In this work finite range ADWA calculation will be used for description of the experimental data, the description of this method is not developed here in the interest of space but one is invited to read the description of such method by Johnson and Tandy [Johnson & Tandy 1974], which is subsequently the method used for all calculations in analysing the ^{26}Al(d, p)^{27}Al data, see Section 5. Finally note that, as depicted in Figure 3.6, the DWBA and ADWA methods do not include an intermediary step, *e.g.* a resonance in the compound system. Instead it is assumed that the transfer reaction is a direct process:

$$A + d \rightarrow B + n, \tag{3.44}$$

which is to be compared with Equation 3.12. In this work this is not an issue. However, it must be noted that it is assumed that in the exit channel, B and the transferred neutron n are bound. This is the case for the excited states in ^{27}Al. The mirror states in ^{27}Si from, for example, the ^{26}Al(^{3}He, d)^{27}Si reaction are unbound and therefore these two methods cannot be used to calculate differential cross section for those states. Incidentally, in this work, there will not be an attempt at fitting the results of Vogelaar *et al.* [Vogelaar 1996] anew, although they have been put into questions by Parikh *et al.* [Parikh 2014] and will be in tension with the results presented in Section 5.

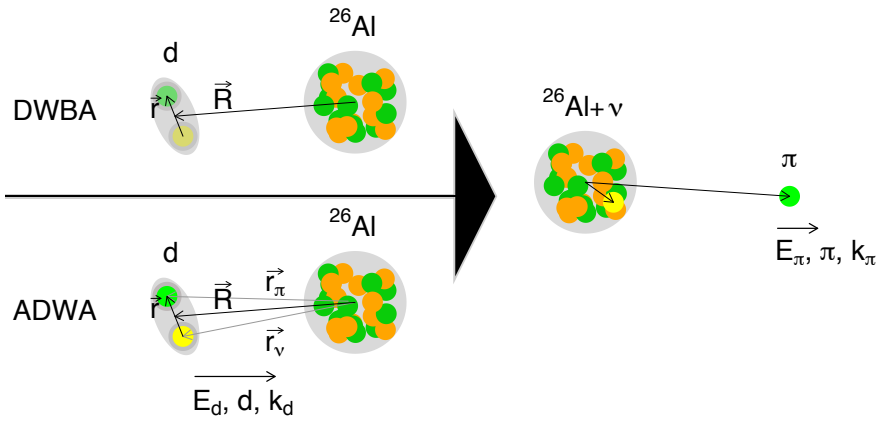

Figure 3.6: Schematic representation of the adiabatic (bottom) and distorted wave (top) approximations for the description of the deuteron projectile and ^{26}Al nucleus target in the entrance channel and of the exit channel.

3.4 The TWOFNR code

In this section, a shortened version of the TWOFNR code developed by Jeff Tostevin from the Surrey group [Tostevin], for calculating cross section of a large array of reactions (in particular when the populated states are bound), is used to explore the effects of parameter changes in the theory. The description of the code itself is beyond the aim of this thesis work, however a comprehensive report by the developers of the full TWOFNR, M. Toyama and M. Igarashi, code is available online [TWOFNR]. Also, upon these choices of parameters, testings of the code and theory against existing data for the ^{26}Mg(d, p)^{27}Mg and the ^{27}Al(p, d)^{26}Al reactions will be presented. Finally some recommendations, elements to keep in mind when analysing angular distribution, are discussed.

3.4.1 Effects of parameter changes in the theory

ADWA vs. DWBA

As said in the previous section, in this thesis deuteron break up is considered through the use of the finite range ADWA method. Here, a comparison is made between ADWA and DWBA calculations for a (fictive) 3 MeV state in ^{27}Al that would be populated in the ^{26}Al(d, p)^{27}Al reaction and for different angular momentum transfer: $\ell = 0$ ($J^\pi = 9/2^+$), $\ell = 1$ ($J^\pi = 9/2^-$), and $\ell = 2$ ($J^\pi = 5/2^+$).

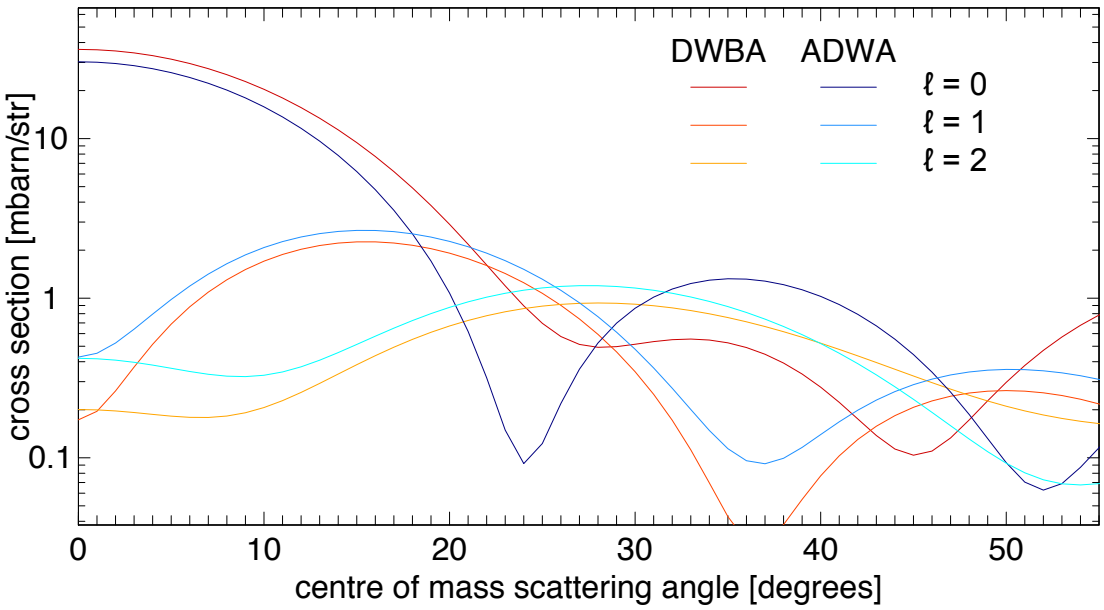

Figure 3.7: Comparison between ADWA and DWBA calculations, for a (fictive) state with $E_{exc} = 3$ MeV in ^{27}Al and different spin and parity, corresponding to $\ell = 0$ ($J^\pi = 9/2^+$), $\ell = 1$ ($J^\pi = 9/2^-$), and $\ell = 2$ ($J^\pi = 5/2^+$). The exit channel is set identically in both calculations, the deuteron potential for the DWBA calculation is from Ref. [Daehnick 1980] while the $p/n \leftrightarrow^{26}$Al potentials and the method to build the deuteron potential uses the Koning-Delaroche potential [Koning & Delaroche 2003], see Section 3.4.1.

In the DWBA calculation, in order to represent the $d \leftrightarrow^{26}$Al interaction, the Daehnick global potential [Daehnick 1980] is used. It is derived from fitting many existing experimental data with a set of parameters, obeying predefined functions given the studied system; this will be discussed later. The differences between the two methodologies are presented in Figure 3.7

"Elastic" potential

The most effective way to explore the interaction between two nuclei is to measure the elastic cross section, ideally at the same energy as that of the transfer reaction that will be studied. A fit of the cross section will then allow derivation of a (experimental) real potential in the form of a Woods-Saxon shape:

$$V(R) = \frac{V_r}{1 + \exp\left(\frac{R - r_r}{a_r}\right)}, \tag{3.45}$$

where r_r is the distance of closest approach, *i.e* the sum of the two nucleus' radii, $r_r = r_f \times (A_1^{1/3} + A_2^{1/3})$, for two nuclei with a number of nucleons, A_1 and A_2 respectively, here r_f is the Fermi radius, usually taken as 1.2 fm. In

the case of $(d,\ p)$ transfer reaction, the experimental study of the elastic $(d,\ d)$ reaction allows for a determination of such potential. If such data are available one must use the DWBA method as in the ADWA method the consideration for independent potentials for the $p \leftrightarrow A$ and $n \leftrightarrow A$ interactions cannot represent the elastic reaction. In the case of the ^{26}Mg$(d,\ p)^{27}$Mg study by Meurders and van der Steld [Meurders & van der Steld 1974] elastic deuteron scattering data was taken and therefore a specific potential for the $d \leftrightarrow^{26}$Mg interaction could be developed. If such data are not available, as is the case in the present study of the ^{26}Al$(d,\ p)^{27}$Al reaction, then optical model potentials must be used.

Optical model potentials

The effective interaction between a nucleus, A, and a nucleon, p or n, can be represented by complex mean-field potentials. These potentials have a real part, often denoted V, and an imaginary part, often denoted W, such that the potential is $\mathcal{V} = V + iW$. These allow for separating the elastic part and the non-elastic channels. The optical name comes from the similarity with how a light wave passing through a medium is treated. Both V and W are mostly described in the shape of a Woods-Saxon potential, similar to that of Equation 3.45. (In the DWBA case, the potential must describe the interaction $d \leftrightarrow A$, and is therefore expressed as shown in the previous point.) Additionally, both real and imaginary potentials are divided into volume potentials, their first derivatives the surface potentials, and the spin-orbit potentials. In the case of charged particles there is also the addition of a Coulomb potential. These potentials are derived from fitting large sets of experimental data for different masses of the target and energy of the beam, with parameters that only evolve with E_{beam}, the target mass A and charge Z_A, and the excitation energy E_x of the populated state in $B = A + 1$. Writing the form factor as a Woods-Saxon shape depending on the interaction distance r, the radius and diffuseness of the nuclei, r_0 and a_0:

$$f(r,\ r_0,\ a_0) = \frac{1}{1 + \exp\left(\frac{r - r_0}{a_0}\right)}, \tag{3.46}$$

the optical potentials are, for a given beam energy E [Koning & Delaroche 2003]:

$$\mathcal{V}(r,E) = -\left(V_V(E) + \imath W_V(E)\right) \times f(r,\ R_V,\ a_V) \tag{3.47}$$

$$+ \imath \times 4a_D W_D(E) \frac{\mathrm{d}}{\mathrm{d}r} f(r,\ R_D,\ a_D) \tag{3.48}$$

$$+ \{V_{SO}(E) + \imath . W_{SO}\} \times \left[\frac{\hbar}{m_p c}\right]^2 \frac{1}{r}\frac{\mathrm{d}}{\mathrm{d}r} f(r,\ R_{SO},\ a_{SO}) \times \mathcal{I}.\sigma \tag{3.49}$$

$$+ V_C(r), \tag{3.50}$$

where m_p is the mass of the proton, $\mathcal{I}$ is the matrix of inertia, σ is the spin operator and V_C is the Coulomb potential:

$$V_C(r) = \frac{Z_A z e^2}{2R_C}\left(3 - \frac{r^2}{R_C^2}\right),\ \text{for } r \leqslant R_C, \tag{3.51}$$

$$= \frac{Z_A z e^2}{r},\ \text{for } r > R_C, \tag{3.52}$$

where the Coulomb radius is $R_C = r_f \times A^{1/3}$, Z_A the charge of A, and z the charge of the beam (here the deuteron and/or the proton)[3]. From global fits of existing data several phenomenological optical parameters are available for the representation of the interaction $d \leftrightarrow^{26}$Al, $p \leftrightarrow^{26}$Al, $n \leftrightarrow^{26}$Al and $p \leftrightarrow^{27}$Al. Here two will be investigated, the Koning-Delaroche (KD02) potential [Koning & Delaroche 2003], which spans a mass region $24 \leqslant A \leqslant 209$ and a beam energy range 1 keV $\leqslant E_{beam} \leqslant$ 200 MeV, and the Chapel-Hill 89 (CH89) potential [Varner 1991], which covers a mass range from $A = 40$ to $A = 209$ and a beam energy region from 10 to 65 MeV/u. Note that ^{26}Al is slightly outside the suggested range of applicability of the CH89 potential in addition the deuteron beam energy is 6 MeV/A which is also below the indications. Yet, it is widely accepted that this potential should perform still respectably well in the aluminium region and at such energies, and, at the very least, it shall be used for informative comparisons [Tostevin communic.]. Both those potentials are included in the front head code for TWOFNR [Tostevin] which builds the input file for TWOFNR. It is shown in Figure 3.8 the effects of only changing the global potentials in an ADWA calculation for a (fictive) 3 MeV state in ^{27}Al that would be populated in the ^{26}Al(d, p)^{27}Al reaction and for different angular momentum transfer: $\ell = 0$ ($J^\pi = 9/2^+$), $\ell = 1$ ($J^\pi = 9/2^-$), and $\ell = 2$ ($J^\pi = 5/2^+$). The calculation shows little changes to the final angular distributions, with the $\ell = 0$ distributions virtually identical up to ≈30 degrees. This demonstrates the effectiveness of global potentials, as for example CH89 is not designed to work in the present

[3] In the exit channel the projectile is the outgoing proton.

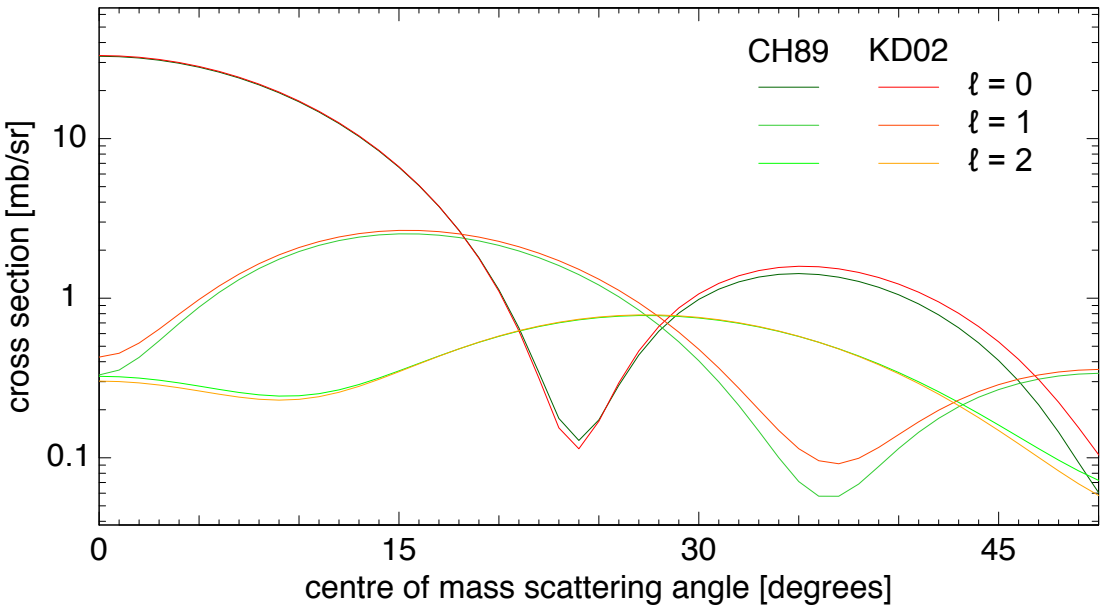

Figure 3.8: Comparison between the uses of the CH89 and KD02 potentials (all other parameters are kept identical), for a (fictive) state with $E_{exc} = 3$ MeV in ^{27}Al and different spin and parity, corresponding to $\ell = 0$ ($J^\pi = 9/2^+$), $\ell = 1$ ($J^\pi = 9/2^-$), and $\ell = 2$ ($J^\pi = 5/2^+$).

case. Indeed it is advised to use global optical potentials where no experimental data is known rather than an experimentally derived potential from even the neighbouring nucleus. In the following of this thesis, the KD02 potential will be consistently used.

Folding the deuteron adiabatic potential

In order to build the deuteron potential from the consideration presented above, a folding potential is needed that reconstruct the *np* system. In this work the Argonne v_{18} potential [Wiringa 1995] has been used.

The neutron geometry

Modelling the neutron potential is a complex part of building a theory of transfer reaction and is one of the main source uncertainties. This is because, being charge-less, the neutron radius and diffuseness (or the root mean square radius, see Figure 3.10.a)) are not well known, furthermore they vary depending on the quantum numbers (n, ℓ) [Gade 2008]. There are several ways to set r_0 and a_0. The first is to use the present work on the ^{26}Al(d, p)^{27}Al reaction. The available shells near $N = 13$ and $Z = 13$ are shown in Figure 3.9, and, as shown in Chapter 2 the ground state spin and parity of ^{26}Al is 5^+. Now considering the

Table 3.1: KD02 optical potential parameters for the adiabatic wave approximation representation of the ^{26}Al(d, p)^{27}Al reaction. Values obtained from the parametrisation given in Ref. [Koning & Delaroche 2003].

Channel	V_V (MeV)	W_V (MeV)	r_V (fm)	a_V (fm)	W_S (MeV)	r_{wS} (fm)
^{26}Al+d: proton (39%)	55.194	0.498	1.167	0.674	7.053	1.295
^{26}Al+d: neutron (61%)	51.988	0.580	1.167	0.674	7.528	1.295
^{27}Al+p	50.485[a]	1.763	1.169	0.674	7.737	1.295
^{26}Al+n	varied[b]		1.275[c]	0.675[c]		
Channel	a_{wS} (fm)	V_{SO} (MeV)	W_{SO} (MeV)	r_{SO} (fm)	a_{SO} (fm)	r_C (fm)
^{26}Al+d: proton (39%)	0.532	5.672	-0.024	0.967	0.590	1.33
^{26}Al+d: neutron (61%)	0.540	5.615	-0.033	0.967	0.590	1.33
^{27}Al+p	0.533	5.373	-0.090	0.970	0.590	1.33
^{26}Al+n	$\ell.\sigma = 6$					

[a] Value corresponding to the 3.004 MeV state, i.e. proton energy 19.67 MeV, otherwise varied to match the state energy.
[b]
[c] For the neutron geometry the radius and diffuseness were set as shown in Table 3.2.

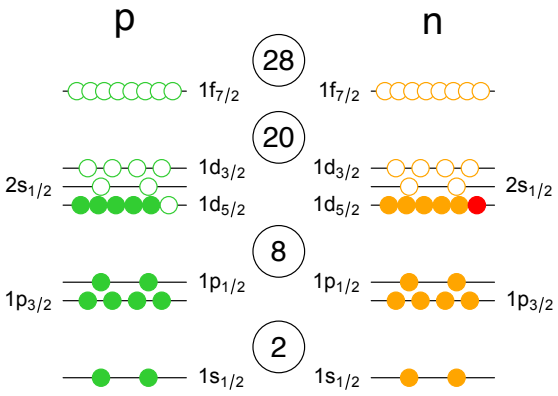

Figure 3.9: Shell model picture of $^{26}_{13}\mathrm{Al}^{13}$, $^{27}\mathrm{Al}$ is made with the inclusion of an extra neutron (in red in the picture). Particles unfilled represent holes and are available for the odd-neutrons upon non-resonant excitations below S_n, the neutron separation energy.

target mass dependency, the rms radius can be set using the best available angular distribution, *i.e.* that with the largest angular coverage and the better statistics, and a χ^2 fit of its distribution. In this study, the level with the best angular distribution is the 3.004 MeV, $9/2^+$ state, for which an $\ell = 0$ transfer means that the neutron transferred is on the $2s_{1/2}$ orbital, and an $\ell = 2$ transfer means that the neutron transferred is on the $1d_{5/2}$ orbital. The angular distribution may therefore be fitted as follows:

$$\left.\frac{\mathrm{d}\sigma}{\mathrm{d}\Omega}\right|_{exp.} = C^2S(\ell=0) \times \left.\frac{\mathrm{d}\sigma}{\mathrm{d}\Omega}\right|_{\ell=0} + C^2S(\ell=2) \times \left.\frac{\mathrm{d}\sigma}{\mathrm{d}\Omega}\right|_{\ell=2}, \tag{3.53}$$

where in each of the two theoretical cross sections the rms radii are independent of each other. Considering the complexity of the theory one must generate the output files from `TWOFNR` for a range of rms radii and then apply a χ^2 fit for several independent parameters. The results for the fit of the 3.004 MeV state are shown in Figure 3.11. From this method the rms radius are 3.64 fm ($2s_{1/2}$, which corresponds to, *e.g.*, r_0 = 1.25 fm and a_0 =0.70 fm) and 3.42 fm ($1d_{5/2}$, which corresponds to, *e.g.*, r_0 = 1.25 fm and a_0 =0.57 fm). However the results greatly vary with the distributions used for the optimisation. Furthermore the generation of the different calculation files and then the individual χ^2 fits make this method computationally

Table 3.2: Neutron radius and diffuseness parameters for different ℓ transfers, from HF calculation [Gade 2008].

ℓ	orbital	r_0 [fm]	a_0 [fm]
0	$2s_{1/2}$	1.159	0.70
2	$1d_{3/2}$	1.279	0.70
2	$1d_{5/2}$	1.263	0.70
3	$1f_{7/2}$	1.180	0.70

time consuming, for results that may not bring much accuracy. Another method is to use a Hartree-Fock (HF) calculation. Such a calculation was performed in Ref. [Gade 2008] for the one-neutron removal from the ground states of ^{23}Si and ^{23}Al. Consequently, in this work, the results of Gade *et al.* are adopted, see Table 3.2. (Note that because the $1p_{1/2}$ is unbound in ^{27}Al the HF calculation cannot estimate the rms radius and the general prescription $r_0 = 1.25$ fm and $a_0 = 0.65$ fm is adopted here.) A consequence of this choice of parametrisation for the neutron geometry is that no systematic uncertainty from that parameter will be carried to the final spectroscopic factors given in the analysis chapter. The impact of such a choice on the $\ell = 0$ and $\ell = 2$ transfer to the 3.004 MeV state in ^{27}Al is shown in Figure 3.12.

3.4.2 Testings and recommendations

Before this work, there had been no reported data on the ^{26}Al(d, p)^{27}Al reaction. Consequently the model and its parametrisation discussed above cannot be tested against existing data. The model performance against existing data is briefly investigated in the following. In particular, this is done with the data available on the ^{26}Mg(d, p)^{27}Mg and the ^{27}Al(p, d)^{26}Al reactions. (Note that the ground state of ^{27}Al has $J^\pi = 5/2^+$, ^{26}Mg is even-even).

Study of the ^{26}Mg(d, p)^{27}Mg and the ^{27}Al(p, d)^{26}Al reactions.

Figure 3.13 shows a comparison between the distribution obtained with TWOFNR for the 985, 1699, 3476, 3562, 3761, 3787, 4150 keV states in ^{27}Mg populated in the ^{26}Mg(d, p)^{27}Mg reaction at $E_{beam} = 12$ MeV. The experimental data comes from the study of Meurders and van der Steld [Meurders & van der Steld 1974]. In the later experimental study the distributions were fitted with a DWBA calculation, using recommended neutron parameters at $r_0 = 1.25$ fm and $a_0 = 0.65$ fm and an *experimental* deuteron potential due to the availability of a data set for the elastic ^{26}Mg(d, d)^{26}Mg reaction [Meurders & van der Steld 1974]. Here the ADWA calculation performed uses all the parameters chosen in the previous section, with the exception of the neutron parameters since they are the main source of uncertainty in the neutron spectroscopic factors. What can be observed is the similarity between the experimental results and the ADWA calculation, see Table 3.3. Furthermore the ADWA calculation seems very efficient at reproducing the angular distribution in the centre of mass region 0 to 30 degrees. At $E_{beam} = 12$ MeV, the angular coverage of the experimental set up presented in this thesis will not exceed 30 degrees, see Chapter 4. Consequently the vaguest

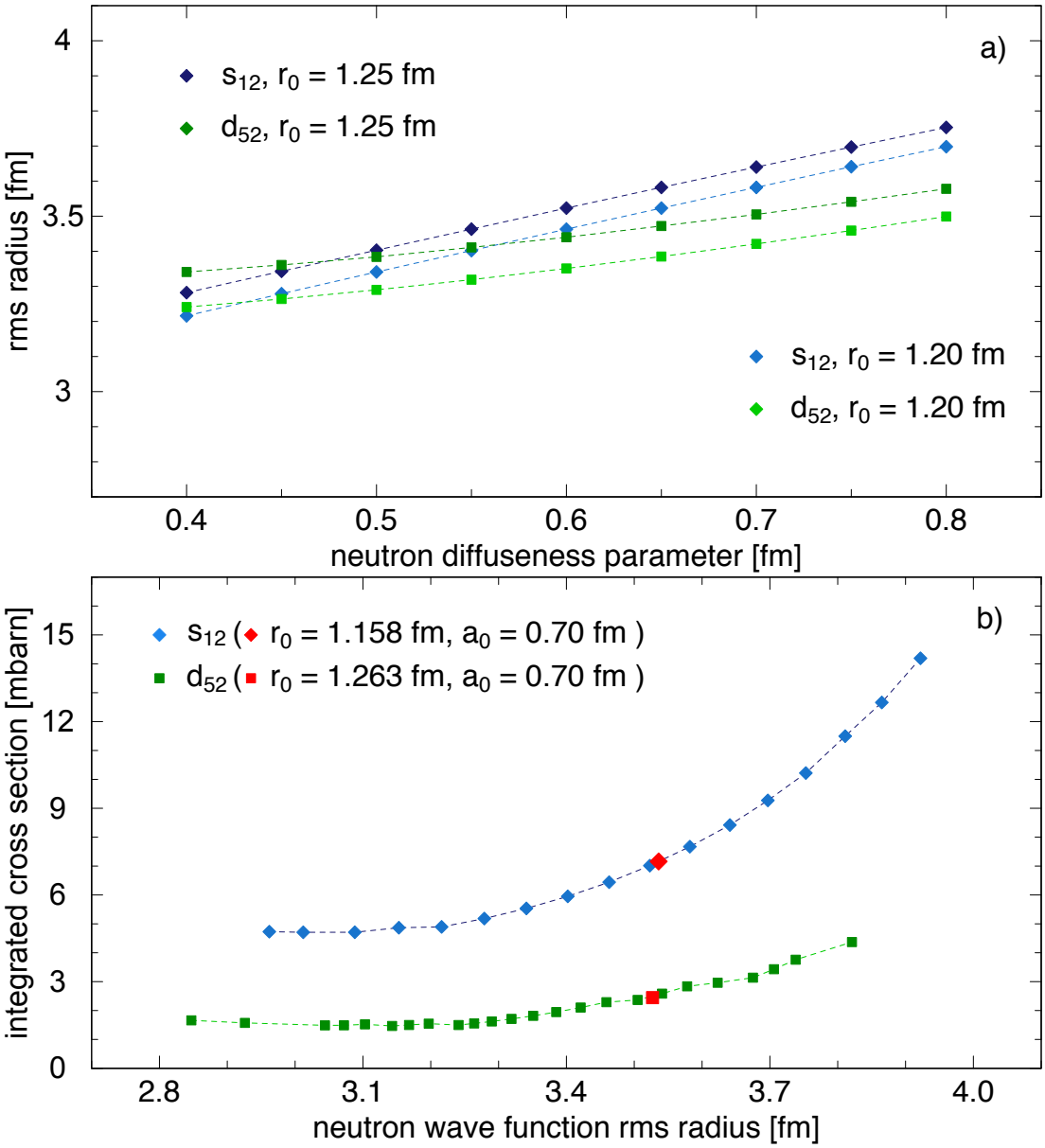

Figure 3.10: a) Dependence of the neutron rms radius on the diffuseness parameter of the neutron potential, for radii 1.20 and 1.25 fm and for $2s_{1/2}$ and $1d_{5/2}$ waves; and b) of the angle-integrated cross section on the neutron rms radius for $2s_{1/2}$ and $1d_{5/2}$ waves. The calculation is made for a state with $E_x = 3$ MeV. The dashed lines are drawn to guide the eye.

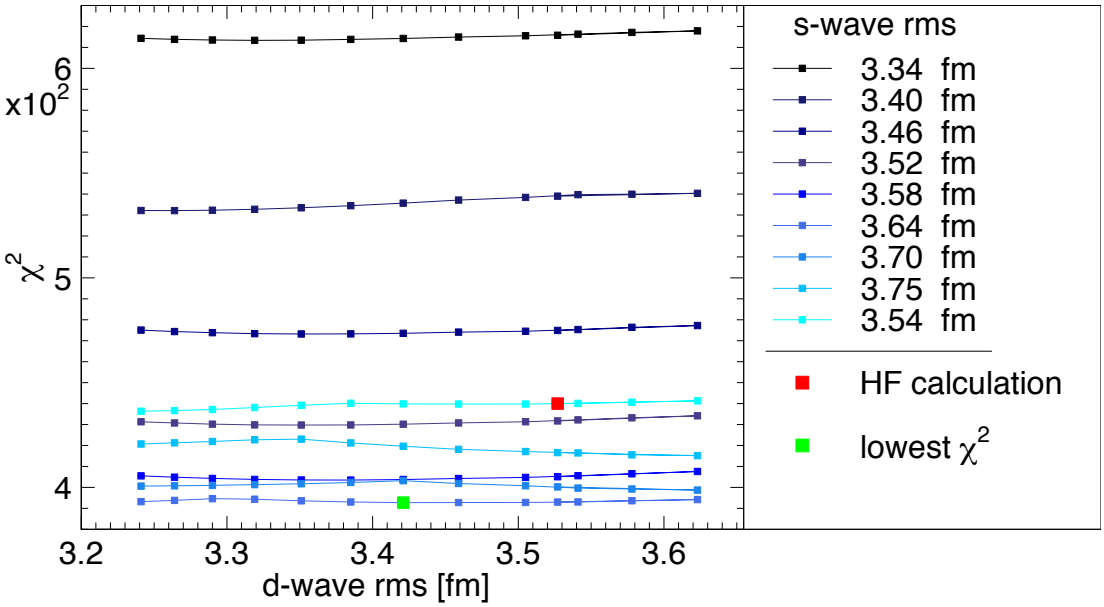

Figure 3.11: χ^2 optimisation of the s- and d-wave neutron rms. The red point shows the χ^2 value obtained using the neutron parameters from the HF calculation, while the green point shows the lowest χ^2 obtained in the optimisation.

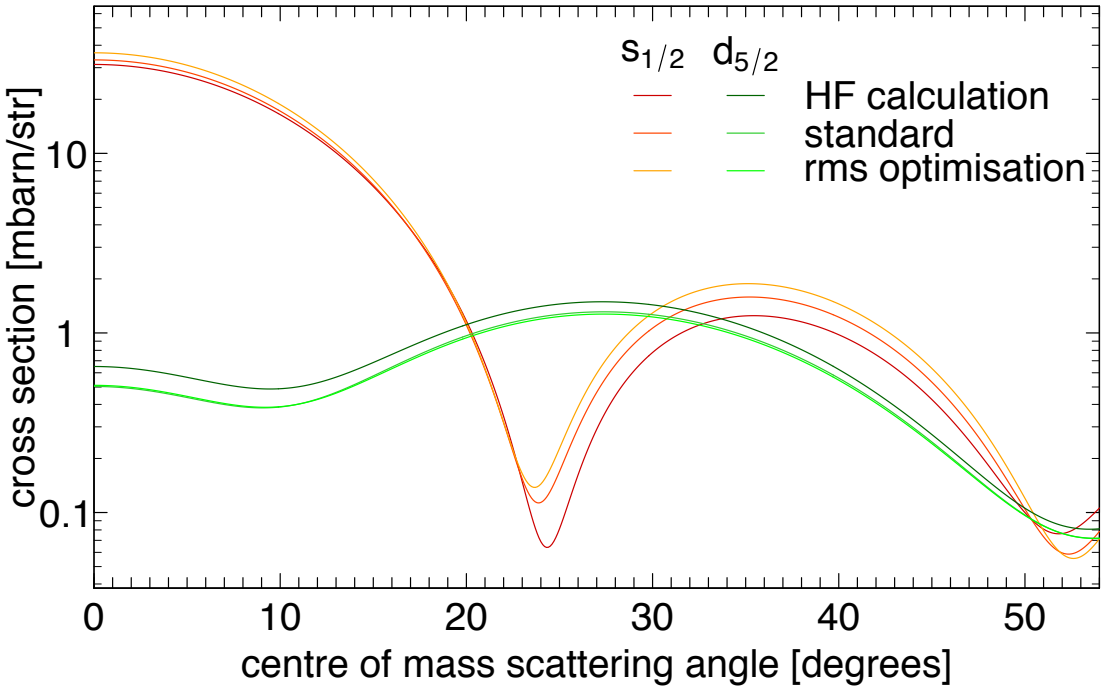

Figure 3.12: Impact on the different choices of neutron parameters between the values of an HF calculation (see text), the standard values (r_0 = 1.25 fm, a_0 = 0.65 fm) and the values obtained from a χ^2 optimisation of the incoherent sum of the $2s_{1/2}$ and $1d_{5/2}$ constituents of the $\ell = 0$ transfer to the 3.004 MeV state in ^{27}Al (see text).

agreement obtained at larger angles is not relevant to the present work.

Table 3.3: Comparisons of the neutron spectroscopic factors in ^{27}Mg, obtained from the ADWA calculation with `TWOFNR` and from the work of Meurders and van der Steld [Meurders & van der Steld 1974].

E_{state}	J^π	ℓ	C2S Meurders *et al.*		C2S `TWOFNR`	
			$2s_{1/2}$ or $1p_{1/2}$	$1d_{5/2}$ or $1f_{7/2}$	$2s_{1/2}$ or $1p_{1/2}$	$1d_{5/2}$ or $1f_{7/2}$
985	$3/2^+$	2		0.6		0.55
1699	$5/2^+$	2		0.13		0.11
3476	$1/2^+$	0	0.29		0.25	
3562	$3/2^-$	1	0.40		0.65	
3761	$7/2^-$	3		0.51		0.48
3787	$3/2^+$	2		0.15		0.1
4150	$5/2^+$	2		0.033		0.025

Figure 3.14 presents the distributions obtained with `TWOFNR` for the ground state and the 228, 417 and 2545 keV states in ^{26}Al populated in the ^{26}Mg$(d, p)^{27}$Mg reaction at E_{beam} = 12 MeV, alongside the experimental data from the study of Show *et al.* [Show 1976]. In Table 3.4 the spectroscopic factor obtained using `TWOFNR` are compared to the results of Show *et al.*. Similarly to the previous observation in the case of neutron spectroscopic factors in ^{27}Mg, it can be seen here that the calculated neutron spectroscopic factors in ^{26}Al using an ADWA calculation (with standard parameters for the neutron geometry) agree well with the DWBA calculation of Show *et al.*. There too elastic scattering data was collected to build the deuteron potential from experimental distribution. At low angles, again, the calculation performs very well with the exception of the 2545 keV state. So consequently, the model chosen to theoretically represent the different interactions occurring in the ^{26}Al$(d, p)^{27}$Al reaction seems to be validated when transposing it to existing data set.

Evolution of the angular cross section with excitation energy

In the previous subsection, it was shown that by comparing the angular distribution obtained using the chosen theoretical model with existing data for neighbouring exciting states, not only was the calculation able to reproduce the low

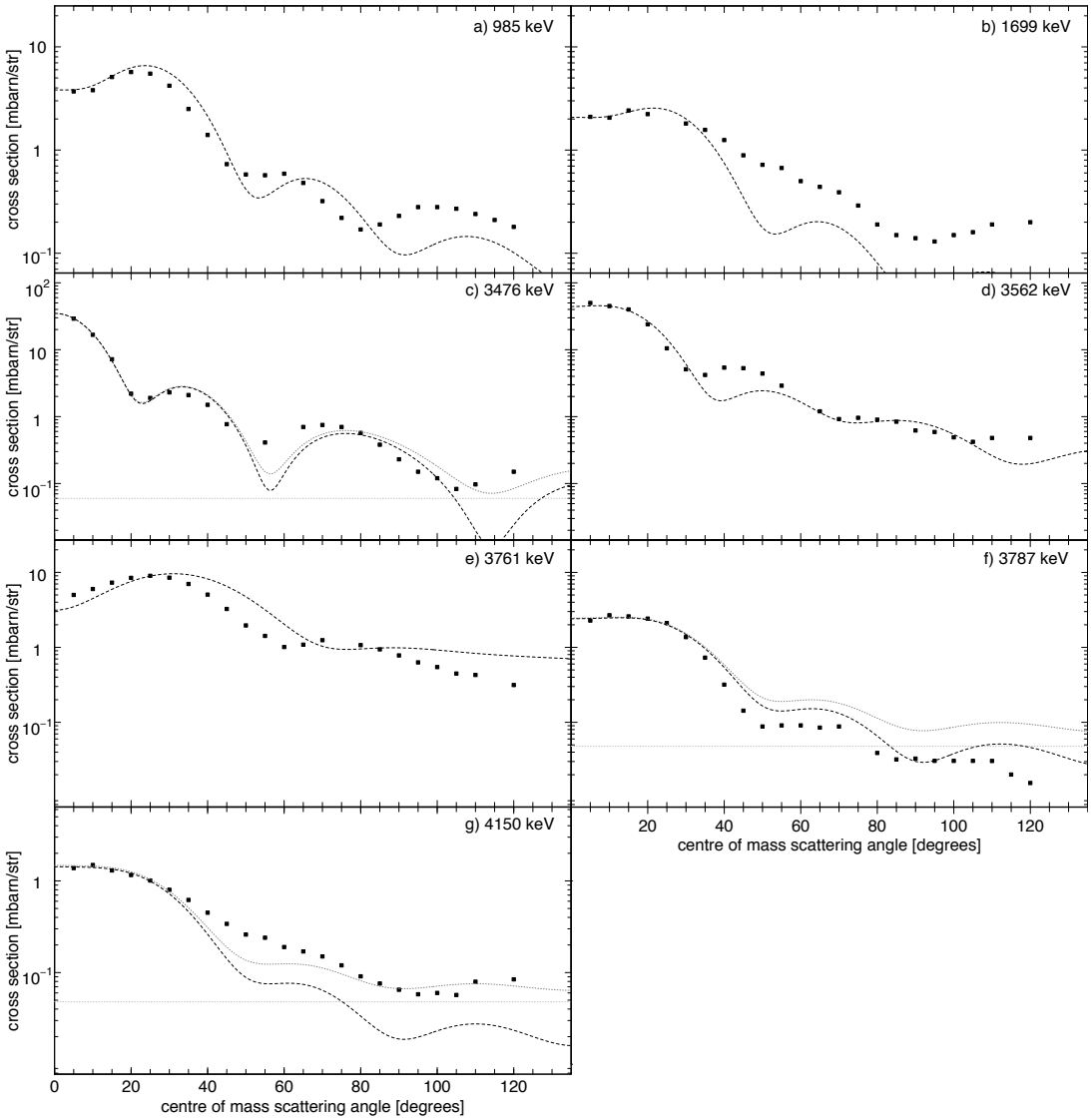

Figure 3.13: Comparison between experimental [Meurders & van der Steld 1974] and ADWA calculations for the distribution of the a) 5^+ 985 keV, b) 0^+ 1699 keV, c) 3^+ 3476 keV, d) 3^+ 3562 keV, e) 3761 keV, f) 3787 keV and g) 4150 keV states in ^{27}Mg populated in the ^{26}Mg(d, p)^{27}Mg reaction at E_{beam} = 12 MeV. The compound nucleus contribution (at $\approx$ 0.06 mb/sr) is added where relevant, the contribution is the light grey dotted line while the ADWA calculation plus this constant is the darker grey dotted line.

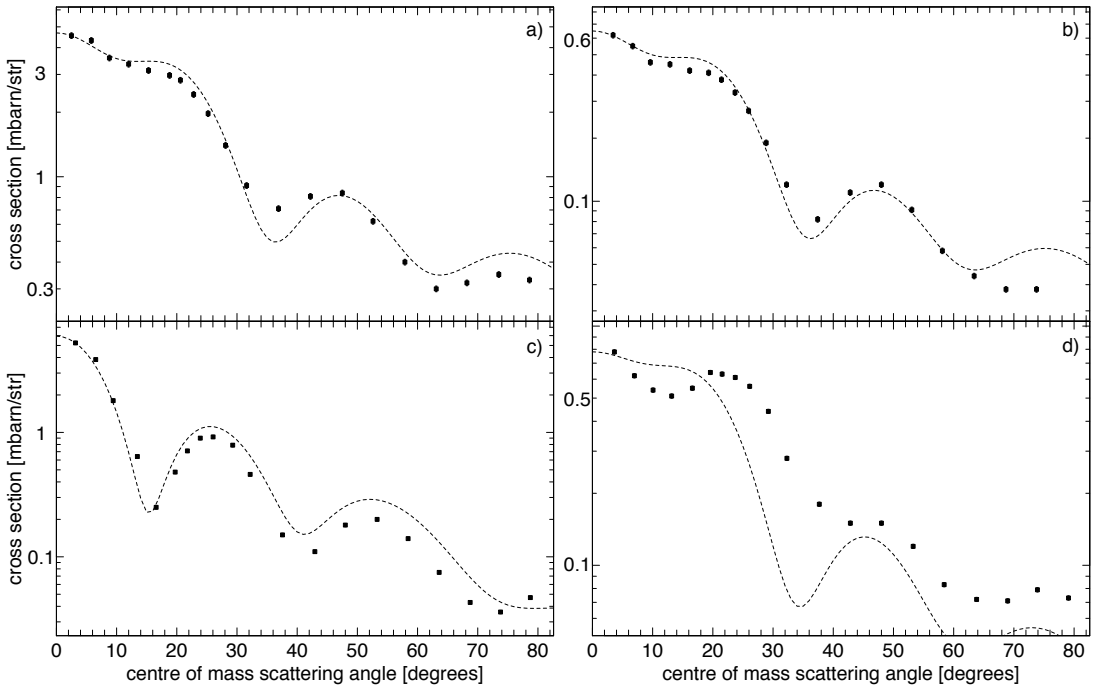

Figure 3.14: Comparison between experimental data [Show 1976] and ADWA calculation for the distribution of a) the 5^+ ground state, b) the 0^+ 228 keV state, c) the 3^+ 417 keV state and d) the 3^+ 2545 keV state in ^{26}Al populated in the ^{27}Al(p, d)^{26}Al reaction at E_{beam} = 35 MeV.

Table 3.4: Comparisons of the neutron spectroscopic factors in ^{26}Al, obtained from the ADWA calculation with `TWOFNR` and from the work of Show *et al.* [Show 1976].

E_{state}	J^π	ℓ	C2S		C2S		C2S	
			Show *et al.*		`TWOFNR`		`TWOFNR` norm.	
			$2s_{1/2}$	$1d_{5/2}$	$2s_{1/2}$	$1d_{5/2}$	$2s_{1/2}$	$1d_{5/2}$
0	5^+	2	/	1.0[a]	/	1.55	/	1.0
228	0^+	2	/	0.14	/	0.21	/	0.14
417	3^+	0	0.21[b]	0.05	0.20	0.07	0.20	0.05
2545	3^+	2[c]	/	0.30	/	0.20	/	0.13

[a] Show *et al.* normalise their $1d_{5/2}$ C^2S such that $C^2S_{g.s.}$=1.0.
[b] The $2s_{1/2}$ C^2S are not normalised.
[c] Shown *et al.* found no experimental evidence of a $\ell = 0$ component.

angle behaviour of the cross section convincingly, but the extracted neutron spectroscopic factors were also in good agreement with the published values where a different model was used. Since the values are nevertheless somewhat different, it is possible that the more accurate description of the deuteron potential results

in more accurate neutron spectroscopic factors. This is however impossible to demonstrate. Here, before analysing at the present data, the evolution of the (theoretical) angular distribution is studied. For ℓ-transfer 0, 1 and 2, the evolution of the cross section as a function of the excitation energy of states in ^{27}Al is shown in Figure 3.15. A striking fact is that as the excited energy approaches S_n, the neutron separation energy, the angular distribution for $\ell = 1$ and $\ell = 2$ transfers become very similar at low angles, with a value at 0 degrees different by only a factor of 3. Consequently the standard behaviour of $\ell = 1$ ("the cross section increases with the scattering angle at low angles") and $\ell = 2$ ("the cross section is relatively flat at low angles") found up to around 9 MeV excitation energy, is not true closer to S_n. This is somewhat expected as $\ell = 1$ and $\ell = 2$ transfers are more peripheral than $\ell = 0$ transfer and consequently are more sensitive to the low energy tail of the spontaneous neutron emission at E$\gtrsim S_n$. However it will prove to be a massive obstacle for assigning the ℓ-values of transfers to a high excitation energy states, where furthermore spin/parities are not known, and, even more, when the angular coverage will not be sufficient to distinguish between $\ell = 1$ and $\ell = 2$ transfers.

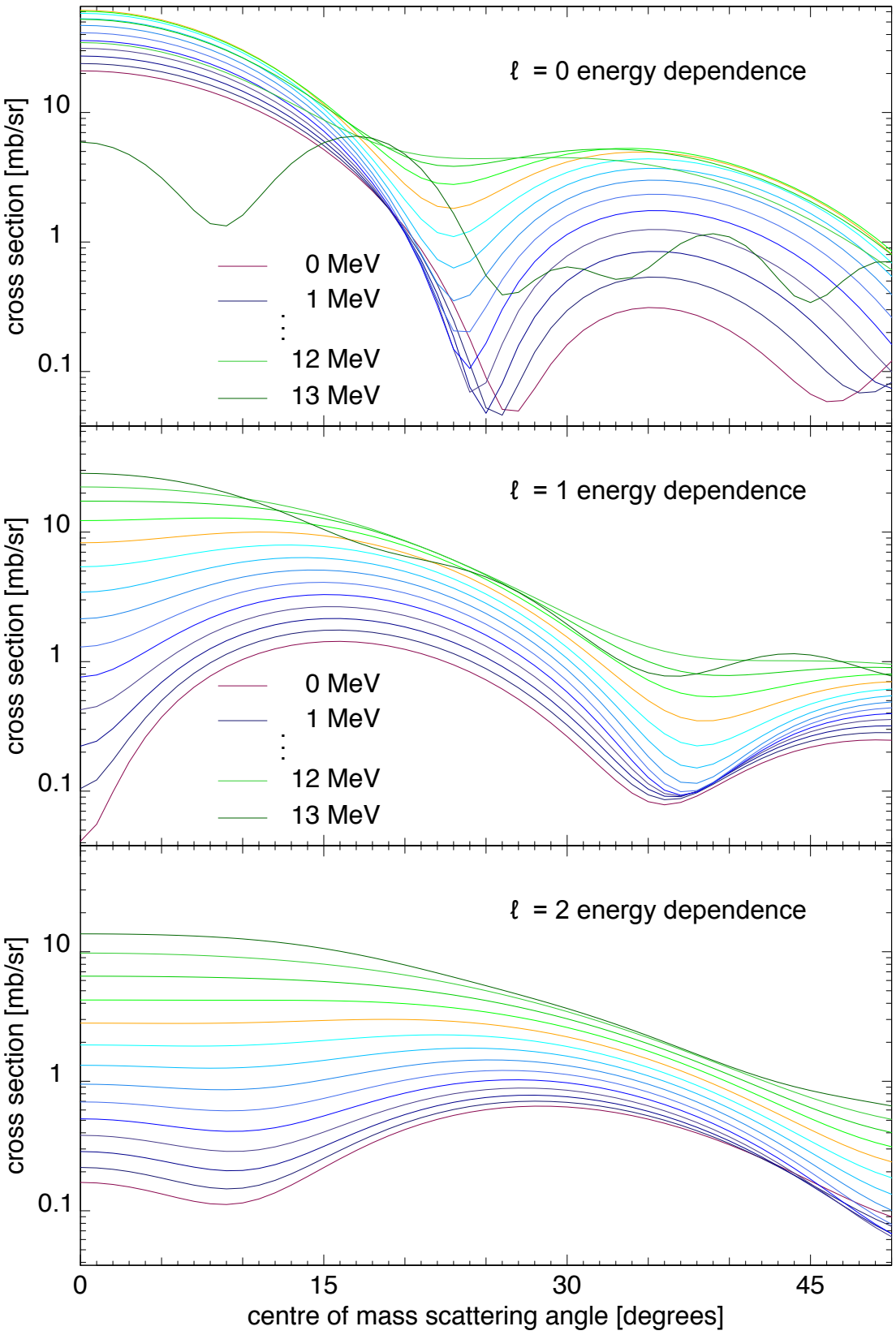

Figure 3.15: Excitation energy dependence of the cross section on the angular momentum transfer for $\ell = 0$ ($1s_{1/2}$), $\ell = 1$ ($0p_{1/2}$) and $\ell = 2$ ($0d_{5/2}$) proton transfer. Colours in the case of $\ell = 2$ represent the same excitation energies as in the above plots.

Chapter 4

Experimental approach

This chapter discusses the experimental methods adopted to perform the study of the two reactions: ^{26}Al(d, p)^{27}Al and ^{44}Ti(α, p)^{47}V. Both experiments used the same type of detector to measure the energy of the ejectile protons, and this is presented in the first section. The remainder of the chapter focus on the particularities of each experiment starting with their respective acceleration facilities, TRIUMF, in Vancouver, Canada and ISOLDE, in Geneva, Switzerland. For the ^{26}Al(d, p)^{27}Al, there is the measurement of the (solid) target thickness as well as the setting of experimental parameters as the data contained evidence that the experiment logbook appears was incoherent. The section on the ^{44}Ti(α, p)^{47}V experimental method focuses of the setting of the reaction energy and on the sourcing of a ^{44}Ti beam material from radioactive waste. This was made via a pioneering method used here for the first time.

4.1 Double sided silicon detectors

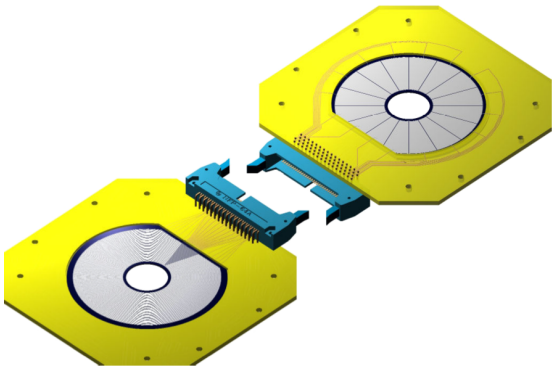

Figure 4.1: MSL type S2 detector.

In this thesis work, the particle detection was made via the use of double sided silicon detectors (DSSD). This is the go-to choice for detection of charged particles in the TUDA array at TRIUMF, Vancouver and for the custom set up that was implemented on the REX-ISOLDE line for the study relevant to ^{44}Ti.

A fundamental difference between the two set of experiments presented is that one study, that of the ^{26}Al(d, p)^{27}Al

Table 4.1: MSL type S2 detector main geometry.

Active inner diameter	2.300 cm	Pitch	491 μm
Active outer diameter	6.984 cm	Distances between strips	0.1 mm

reaction, focusses on measuring differential cross section (*i.e.* angular distribution), while at CERN the objective was to obtain an integrated cross section of the ^{44}Ti(α, p)^{47}V reaction. However, in both cases, the detection of few MeV protons and/or α-particles was required, for which the established silicon detector technology is well suited. Considering that the energy deposited by a particle as it travels through a material is proportional to the square of the atomic number of the element Z^2, the additional presence of a thin layer at the front allows to map the particle species via its energy deposited in this layer, E, and the difference with the energy deposited in the back layer, ΔE, hence the denomination ΔE-E telescope. Here each telescope consists of two Micron Semiconductor Ltd S2-type silicon detectors [MSL S2] of 65 μm and 1000 μm thickness. The two components of the telescope each provided 48 circular strips and 16 azimuthal sectors. The geometric characteristics of the MSL S2 detector can be found in Table 4.1 and it is shown in Figure 4.1. For the data acquisition, RAL108 preamplifiers are fitted to each strips and sectors (i.e. 48+16 RAL108 per detector), such that the signals are amplified and shaped to 86 ns to match the beam RF signal frequency. A logical AND in a 100 ns time window is then used for the trigger of the ADCs. Note that the trigger of the TDCs, which were used in this experiment to clean the data, is based on the ADCs trigger although, as the TDCs are used in stop mode, to ensure that the chronology of events is respected the beam RF is first delayed and then re-timed to the RF when the trigger signal of the ADCs is logically added to the beam RF, see Figure 4.2.

4.2 Experimental details on the ^{26}Al(d, p)^{27}Al reaction

The proton spectroscopy study of the ^{26}Al(d, p)^{27}Al reaction reaction was performed at TRIUMF using the TUDA (TRIUMF UK Data Array) array installed on the ISAC-II (Isotope Separator and Accelerator) line. The experiment was performed in June 2012 after a two year period of set up and tests. As such there is here only a modest introduction to this facility, aiming at presenting the main equipment used for the experiment. More profound details can be found in the

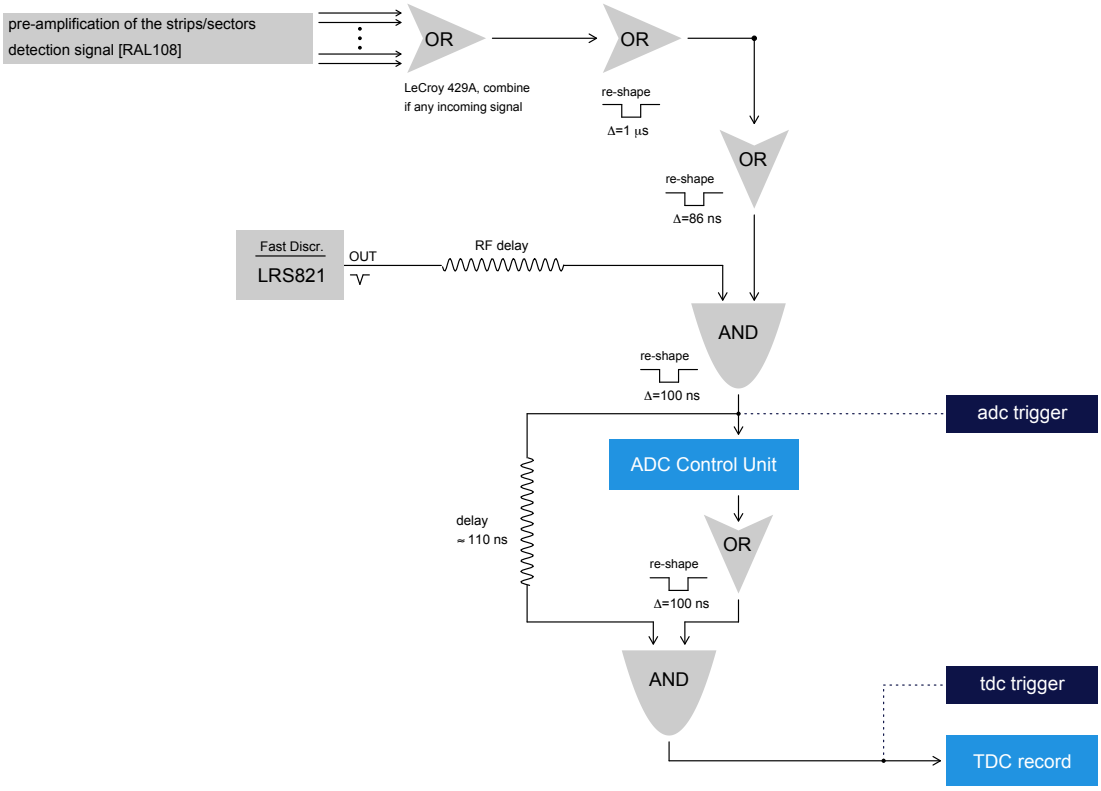

Figure 4.2: Basics of the trigger logics for the data acquisition from the TUDA array detectors.

thesis work of Chris Ruiz [Ruiz 2003], which is more focussed on the development of the facility.

4.2.1 TUDA at ISAC

Radioactive Ion Beams and ISAC-II

The Isotope Separator and ACcelerator (ISAC) facility at TRIUMF is used for post-acceleration of radioactive and stable beams produced using the ISOL technique. Production of online radioactive beams requires first to use a "classic" linear accelerator to impinge a stable beam, in general protons, onto a primary target chosen in oder to create sufficient amount of a desirable isotope, for example ^{26}Al. The spallation reaction fragments are then caught into an ioniser, and extracted into a mass separator, which selects the species according to the sought mass to charge ratio, or A/q. This can be done via a quadrupole by carefully choosing the B_ρ which links the A/q ratio to the curvature of the magnet and consequently over or under bent the contaminants while sending the correct isotope into the beam line. The species is subsequently (post-)accelerated by,

usually, another LINAC.

To produce ^{26}Al beams, a primary beam of 70 μA, 500 MeV H^- ions was produced by the TRIUMF cyclotron and bombarded on a Silicon Carbide, SiC, target (Tantalum or Niobium would also be available for higher mass fragments). After the reaction, the ^{26}Al isotopes are locked in the target cell through which a 55 kV voltage is applied and further laser ionisation (to charge 1^+), which is one of the choices at ISAC-II for low ionisation energy atoms (aluminium has an ionisation potential at 6 eV), is used to extract the ^{26}Al ions at keV/u. Mass separation ensures that only the ^{26}Al ions are extracted. The feeble beam is pre-bunched and transported by the Low Energy Beam Transport towards the RFQ (Radio Frequency Quadrupole) which accelerates the ions up to 150 keV/u. The beam is now said of medium energy, it is chopped, stripped to $A/q \in [3, 6]$ (26/6 in the present work experiment), rebunched and transported to the linear accelerator (Drif-Tube LINAC) that provides the acceleration to the final energy, 6 MeV/u in the present case. The beam intensity delivered by TRIUMF and ISAC-II was found to be 1 pnA.

In this process, two main contaminants can slip through. The isomeric, τ = 9 s, 0^+ state in ^{26}Al, however it was found that it would be produced in a 1:17000 ratio compared to the ground state of ^{26}Al. The second one is 22Na which, in particular, contaminate the ground state line of ^{27}Al as observed in the spectra shown in the next chapter.

TUDA

The array is composed of two parts. Looking up to down the beam stream, the first is the scattering chamber, positioned just after an collimator assembly that, after the last quadrupole, focuses the beam onto the target in the chamber. The collimator can be varied to match the mass and energy of the target to the position of the target. A secondary 10 mm collimator, itself part of the TUDA apparatus, is placed before the beam passes into the detector area, whatever their position with regards to the target, to provide extra protection for the equipment against scattering of the beam. The detector assemblies, perpendicular to the beam axis, are adjustable so they can be mounted upstream or downstream against the target position. And since the most meaningful measurement of (d, p) reactions are upstream compared to the target position and in the laboratory frame, three detectors were positioned at nominal positions of -5.3 (-2.5), -20.3 and -75 cm, fixing the 0 distance at the target position. (Note that positioning the detector upstream means that the clarity of the data prevents the need of particle identification.) There are additional collimators in the scattering chamber positioned

behind the detectors, used as dumps to prevent the primary and scattered beam from hitting the detectors or target assembly. Finally turbo vacuum pumps are used to bring the operating pressure to around 10^{-6} Torr (or mbar). At the back of the scattering chamber, a Faraday cup is installed to allow for beam intensity measurement. In this experiment, where polyethylene (*i.e.* CH_y compound) targets were used, another mean of measuring beam intensity was provided by two photodiodes detectors positioned far downstream and at 3$\circ$ to the target (in the laboratory), which measured elastic ^{12}C from the impingement of the beam onto the target. However, as it was found that the beam was not perfectly aligned and that it was spatially oscillating, this was only used as a check and the Faraday cup values were those conserved for beam intensity measurements.

4.2.2 Target thickness

As said earlier in this section, during the experiment, solid $(CH_2)_n$ and $(CD_2)_n$ polyethylene targets were used. For the particular study of the ^{26}Al(d, p)^{27}Al reaction, the deuterium came from $(CD_2)_n$ targets made by the Daresbury laboratory near Liverpool. The measurement of the thickness of those targets, from which the deuteron content at origination is derived, was made by measuring the α-particle spectrum from a ^{239}Pu, ^{241}Am, ^{244}Cm triple source with and without the targets between the source and the detector. Knowing the energy loss dE/dx, the thickness can be derived. The measurement, which yielded a thickness of 57(9) μg/cm^2 (the nominal thickness as stated by the Daresbury laboratory is 50 μg/cm^2), is presented in Figure 4.3, the corresponding number of deuteron scattering centres is $4.3(7)\times10^{18}$. This number will decrease as the experiment proceeds, mostly because the impinging ^{26}Al particles from the beam will knock the deuterons out of the target, depleting it of its deuterium content. Tracking this feature involves the analysis of the time dependency of a clean line in the measured spectra against the recorded current on the Faraday cup placed at the back of the TUDA array (to obtain an effective unbiased measured of the beam intensity on target). Since a constant value should be measured with no loss of deuteron, the ratio decay will be used as a proxy for the tracking of the deuteron content of the target. This will be shown in Chapter 5.

4.2.3 Determination of experimental parameters

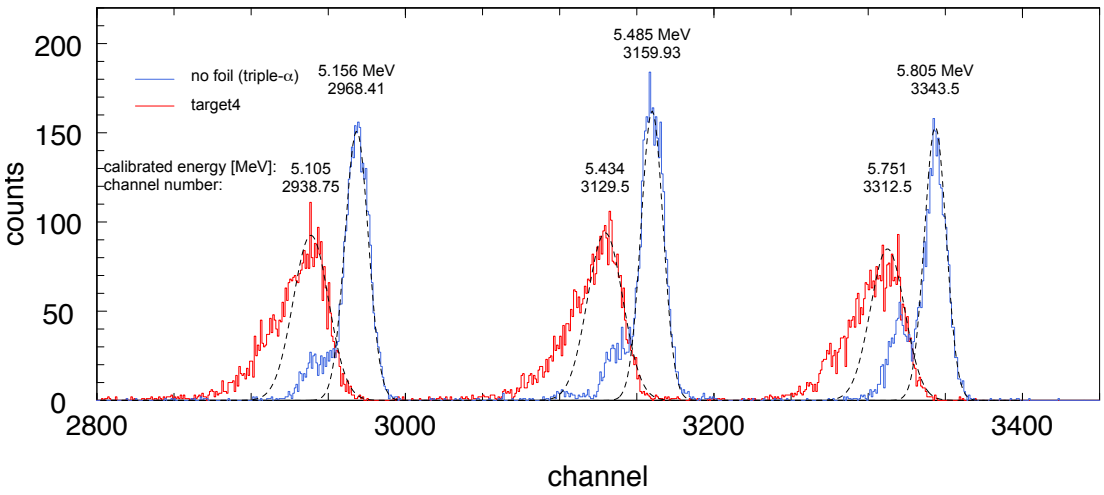

Figure 4.3: Measurement of the energy lost by α-particles from the decay of ^{239}Pu (E_α =5.1566 MeV), ^{241}Am (E_α =5.4856 MeV), ^{244}Cm (E_α =5.8048 MeV) as they travel through target number 4 of the bunch of CD_2 targets provided by Daresbury laboratory.

Table 4.2: Detector distances.

detector	Logbook distances [cm]	Displayed distances [cm]
s2-1	75.0	75.2(2)
s2-2	20.3	20.5(2)
s2-3	5.3	5.5(2)
s2-4	2.5	3.1(3)

During the analysis stage of the experiment, it became apparent that the detector distances recorded in the logbook could not represent the actual physical distances. This was especially obvious for the two closest detectors for which measurement of the distance is harder, but also for which a variation in the distance has the biggest impact on the laboratory scattering angle. Demonstration and correction of the detector distances is made using the most prominent line in the spectra, that corresponding to the 3004 keV, $9/2^+$ state in ^{27}Al. This is one of the very few lines that can be studied at the full angular coverage provided by the detectors, and for which the statistics are high enough for meaningful conclusions to be drawn. Raw output angular distribution from the nominal (logbook) detector distances displays a step between each set of angles corresponding to the different detectors. This is obviously wrong for a derivable physical quantity. In particular from one detector to another there is a step in the y-axis and a change of shape, see Figure 4.4. In the centre of mass, a detector distance change impacts the angle of each strip to the reaction locus as well as the cross section as it changes the Jacobian. The choice of distances used for displaying the distribution was made by investigating the effect of changing them by ± 1 cm and adopting those for which a shape and amplitude agreement could be reached. Those distances are shown in Table 4.2. Uncertainties were

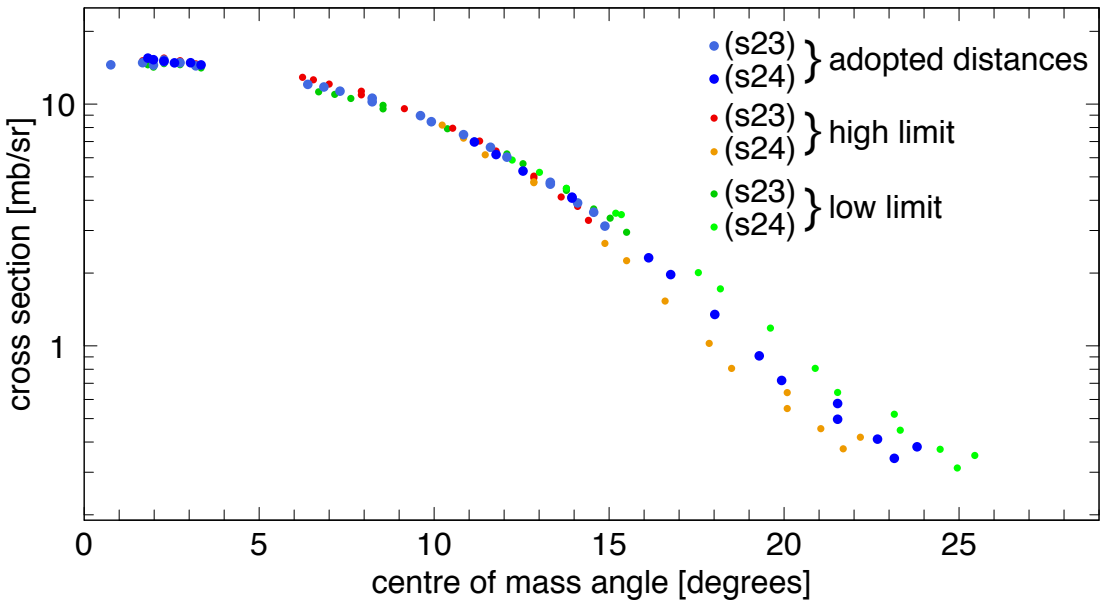

Figure 4.4: Impact of a change in detector distance to the final distribution, in this example, of the 3004 keV state in ^{27}Al. The blue tainted bigger points represent the accepted values (distances s2-1, -2, -3, -4: 75.2, 20.5, 5.5, 3.1 cm), the red tainted smaller points shows the distribution with the low boundary of the distance uncertainties (distances s2-1, -2, -3, -4: 75.0, 20.3, 5.3, 2.8 cm), and the green tainted smaller points shows the distribution with the high boundary of the distance uncertainties (distances s2-1, -2, -3, -4: [75.4, 20.7, 5.7, 3.4] cm). Note the logbook s2-1, -2, -3 and -4 distances are 75.0, 20.3, 5.3 and 2.5 cm, respectively.

also introduced at 2 mm for detector s2-1, -2 and -3, while due to the extra complexity of putting a detector very close to the target an uncertainty of 3 mm is introduced for s2-4. Note that the logbook distances for the case of s2-1, -2 and -3 are correct within uncertainties with this choice. Such a reconciliation was not possible with s2-4.

4.3 Experimental details of the ^{44}Ti(α, p)^{47}V reaction measurement

4.3.1 From radioactive waste to beam source: an alpine journey

In the present study, a ^{44}Ti beam was produced in a novel way. As part of the ERAWAST initiative [Dressler 2012] highly irradiated components from accelerator devices at the Paul Scherrer Institute (PSI) were exploited as a source of exotic ra-

dio isotopes. Radiochemical separations, combining liquid-liquid extraction and ion-exchange chromotography, were used to extract ^{44}Ti from martensitic steel specimens. A sample of around 50 MBq of ^{44}Ti was obtained and dissolved in diluted HF solution (see Ref. [Dressler 2012]). This sample was then evaporated on a molybdenum foil, and transported from PSI to CERN, in order to provide a beam source.

4.3.2 REX-ISOLDE

At CERN the sample was inserted into a standard target container in the ISOLDE Class A target laboratory, connected to a VADIS FEBIAD ion source in the VD5 configuration, and equipped with a large CF4 gas leak to allow for the production of Ti beams as TiF_x molecular ions [Stora 2013]. The unit was then installed on the General Purpose (mass) Separator Front End and a TiF^{3+} molecular beam extracted, before being bunched and cooled in the REX-TRAP Penning trap, see Figure 4.5. (REX-ISOLDE is more frequently used to post-accelerate low energy radioactive beams created by the in-flight method.) This was then dissociated during charge breeding in the Electron Beam Ion Source (EBIS) which is done by electron impact ionisation before acceleration in the LINAC. The LINAC part of REX-ISOLDE [Habs 2000] consists, first, of a radio-frequency quadrupole (RFQ) accelerator which accepts the bunched beams from EBIS/GPS at a very low (hence cooled) energy of 5 keV/u, and brings them to 0.3 MeV/u. The following part contains an interdigital H-type (IH) structure and three seven-gap resonators, which delivers a beam energy selected by the user between 0.8 and 2.2 MeV/u. The IH accelerates the beams to 1.2 MeV/u, so the seven-gap resonators may effectively de-accelerate the beams, if required.

Here, $^{44}Ti^{13+}$ beams of 5×10^5 to 2×10^6 pps, with no apparent isobaric contamination, were provided to the experimental apparatus for 4 days. The beam was accelerated to $\approx$ 2.1 MeV/u and impacted upon on a aluminum windowed gas cell containing $\approx$67 mbar of helium gas.

Finally a High Purity Germanium detector (HPGe) was positioned next to the chamber to monitor γ-ray activity coming off the target.

4.3.3 Gas cell and detector set up

The design of the gas cell must tackle several requirements. In coordination with the available beam energy the gas cell window has to degrade the energy of the beam to the Gamow window, while avoiding such degradation that its energy width in the gas cell would become too big. In this case, the beam energy

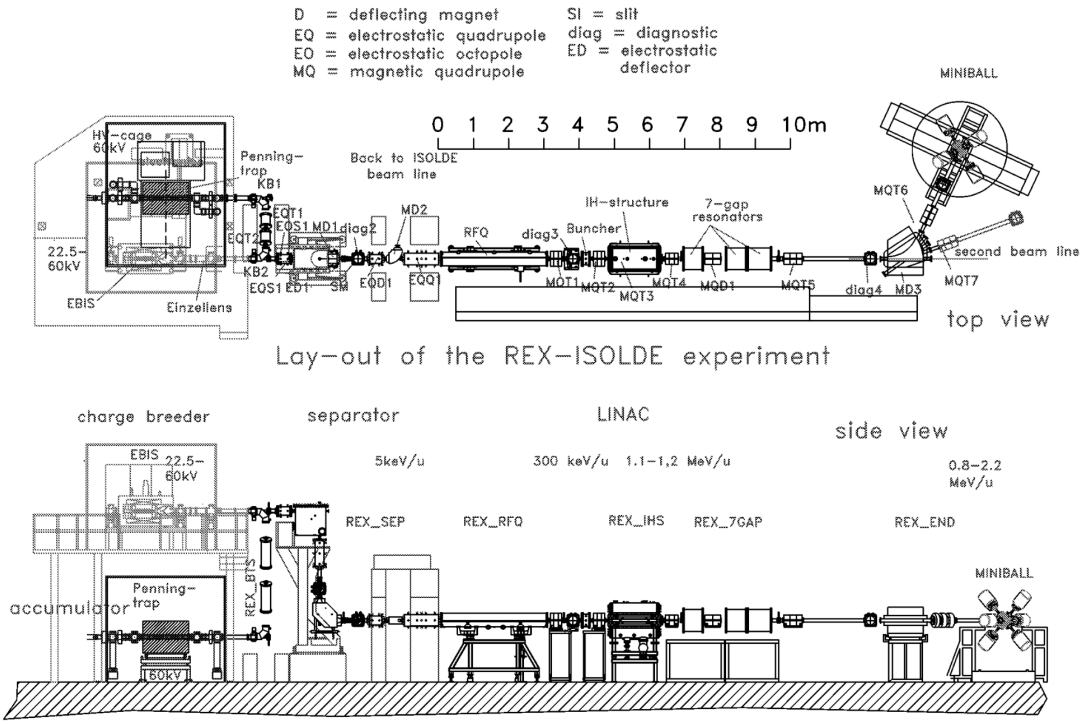

Figure 4.5: Schematic of the REX-ISOLDE experiment at CERN. In the present work the ^{44}Ti ions were fed to EBIS and the detector set up was positioned on the user dedicated second beam line, this figure is taken from Ref. [Habs 2000].

would cover too large an energy region within which the cross section might vary by one or two order of magnitudes. The requirement is therefore to use a thin entrance window. On the other hand, to maximise the number of events at any given energy, a higher gas pressure, and by way of consequence the number of (α-particle) scattering centres, is beneficial. The latter requirement is relatively opposed to the former, to increase the mechanical resistance of the window, a thicker layer of material is required, however to keep the beam width reasonable a thiner layer of material is necessary. The material itself has to be of relatively high Z in order to maximise the Coulomb barrier between the ^{44}Ti beam and the material components, but not so high as for it to increase the energy loss per unit thickness too much. It was decided that aluminium would be the best material to meet most of the requirements. It is also important to note that the use of a windowed gas cell means that water and oil will condensate on the windows during the experiment.

The energy choice is therefore still complex. The energy loss of titanium ions in an aluminium layer rapidly increases with thickness (see Figure 4.6). Consequently, the larger the thickness the higher the initial required beam energy. In fact, if the thickness exceeds 8 μm then fusion between ^{44}Ti particles and both

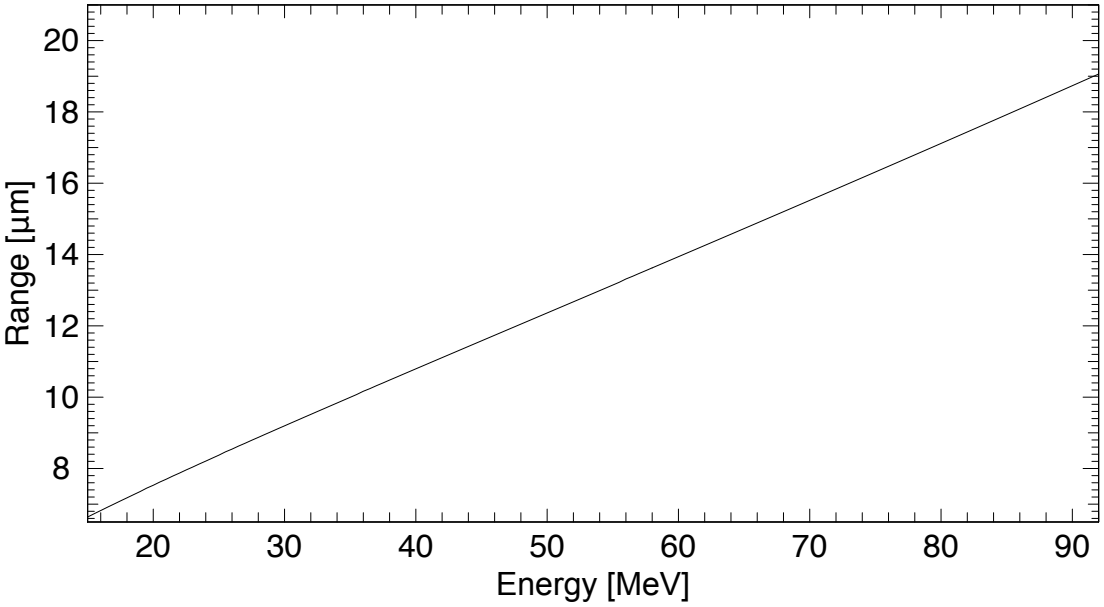

Figure 4.6: Range, in μm, of ^{44}Ti ions penetrating through an aluminium foil as a function of the ^{44}Ti beam energy.

^{12}C and ^{16}O from water and oil condensation will occur. This is due to the rather low Coulomb barrier for the fusion of ^{44}Ti and ^{27}Al (107 MeV), ^{16}O (99 MeV) or ^{12}C (95 MeV). Either of those will principally lead to many protons being produced by fusion evaporation. Channels with the higher cross sections from the fusion of ^{44}Ti and ^{12}C, ^{44}Ti and ^{16}O, and ^{44}Ti and ^{27}Al are shown in Figure 4.7, this is obtained from statistical model calculations performed with the program PPACE, Table 4.3 describe the main channel and the particles emitted.

Window thicknesses of 4 and 6 μm were pressure tested at Edinburgh before the experiment, and it was found that only 6 μm layer could be reliably used after pin hole checks were carefully made. None of the 4 μm windows resisted tests with a gas pressure as low as 15 mbar.

The exit window presents a lesser challenge as the energy loss of light particles, *i.e.* protons and alpha-particles, is negligible for a thin layer of aluminium, such that a thickness of 15 μm was used as it gave a great rigidity and ease of use.

For the detection of light particles a ΔE-E telescope, consisting of two Micron Semiconductor Ltd S2-type silicon detectors as described above, was positioned 12.7 cm downstream with respect to the exit window of the gas cell, providing an angular coverage θ_{lab} = 5.3–15.3°. A quenching factor of 0.986 was then applied to protons [Reichard 2012].

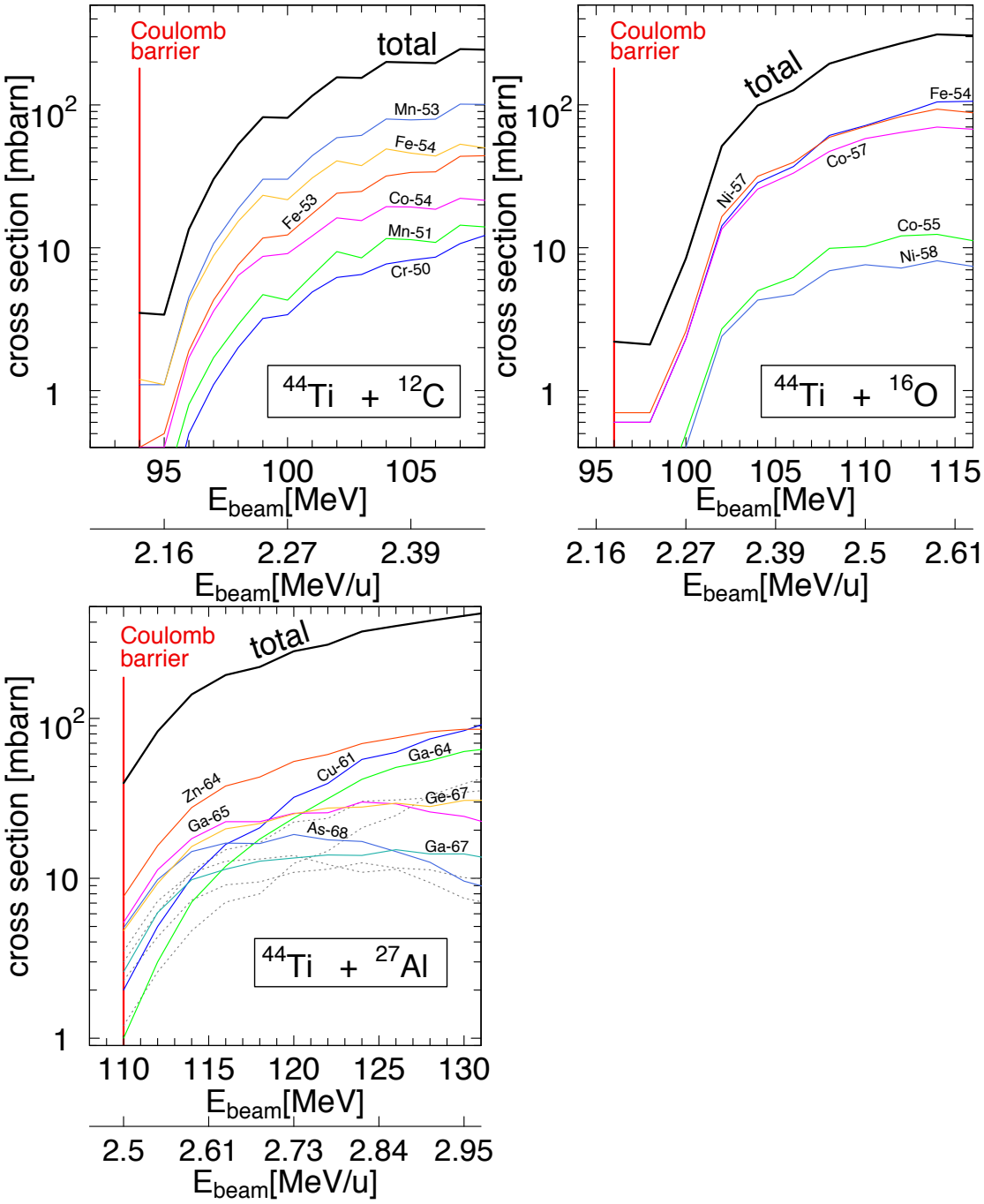

Figure 4.7: Calculated cross sections for the reaction of ^{44}Ti on ^{27}Al (^{71}Br), the windows material, and on ^{16}O (^{60}Zn) and ^{12}C (^{56}Ni) from oil and water condensation on the windows.

Table 4.3: List of fusion reaction and associated prominent evaporation channels potentially occurring when impinging a ^{44}Ti beam on a ^{27}Al window subject to oil and water condensation. The Coulomb barrier energies for those reactions are given in the text.

Reaction	Compound Nucleus	Formed nucleus	Evaporation channel
^{44}Ti+^{12}C	^{56}Ni	^{53}Mn	$3p$
		^{54}Fe	$2p$
		^{53}Fe	$2p1n$
		^{54}Co	$1p1n$
		^{51}Mn	$3p2n/\alpha 1p$
		^{50}Cr	$4p2n/\alpha 2p$
^{44}Ti+^{16}O	^{60}Zn	^{54}Fe	$4p2n/\alpha 2p$
		^{57}Ni	$2p1n$
		^{57}Co	$3p$
		^{55}Co	$3p2n/\alpha 1p$
		^{58}Ni	$2p$
^{44}Ti+^{27}Al	^{71}Br	^{64}Zn	$5p2n/\alpha 3p$
		^{65}Ga	$4p2n/\alpha 2p$
		^{61}Cu	$6p4n/2\alpha 2p$
		^{64}Ga	$4p3n/\alpha 2p1n$
		^{67}Ge	$3p1n$
		^{68}As	$2p1n$
		^{67}Ga	$4p$

Chapter 5

Experimental results for the ^{26}Al(d, p)^{27}Al reaction

In this chapter, the results from the experiment on the ^{26}Al(d, p)^{27}Al reaction conducted at the ISAC-II facility in TRIUMF are shown. Some experimental set up features meant that part of these results had to be used to reconstruct the exact geometry of the set up in Chapter 4. However other experimental details could only be unveiled by a thorough investigation of the experimental data. The chapter starts with such a case as it presents the actual, *i.e.* measurement based, deuteron content of the target that provides the number of scattering centres available during the experiment. Further aspect of the detection set up are then explained. The longest part of this chapter however first discussed assignments of observed lines to known states in ^{27}Al via measurement of their energy and the selectivity of the reaction. Then using theoretical calculations of the angular distribution for observed states, assignments are made using spin/parity consideration. From these assignments, spectroscopic factors are finally deduced.

5.1 Deuteron content of experimental targets

To extract the cross section, both the incident number of particles on target and the number of scattering centres contained in the target must be known. Here to track the deuteron content of the target, the intensity of the most intense line in the observed spectra (that corresponding to the 3004 keV state) was measured in each run, while the beam intensity was taken from integrating faraday cup measurements of the beam current downstream of the target in those same runs. The ratio provides a proxy for the evolution of the deuteron content and can be seen in Figure 5.1. The systematic uncertainty for deuteron content is ≈8%. With a

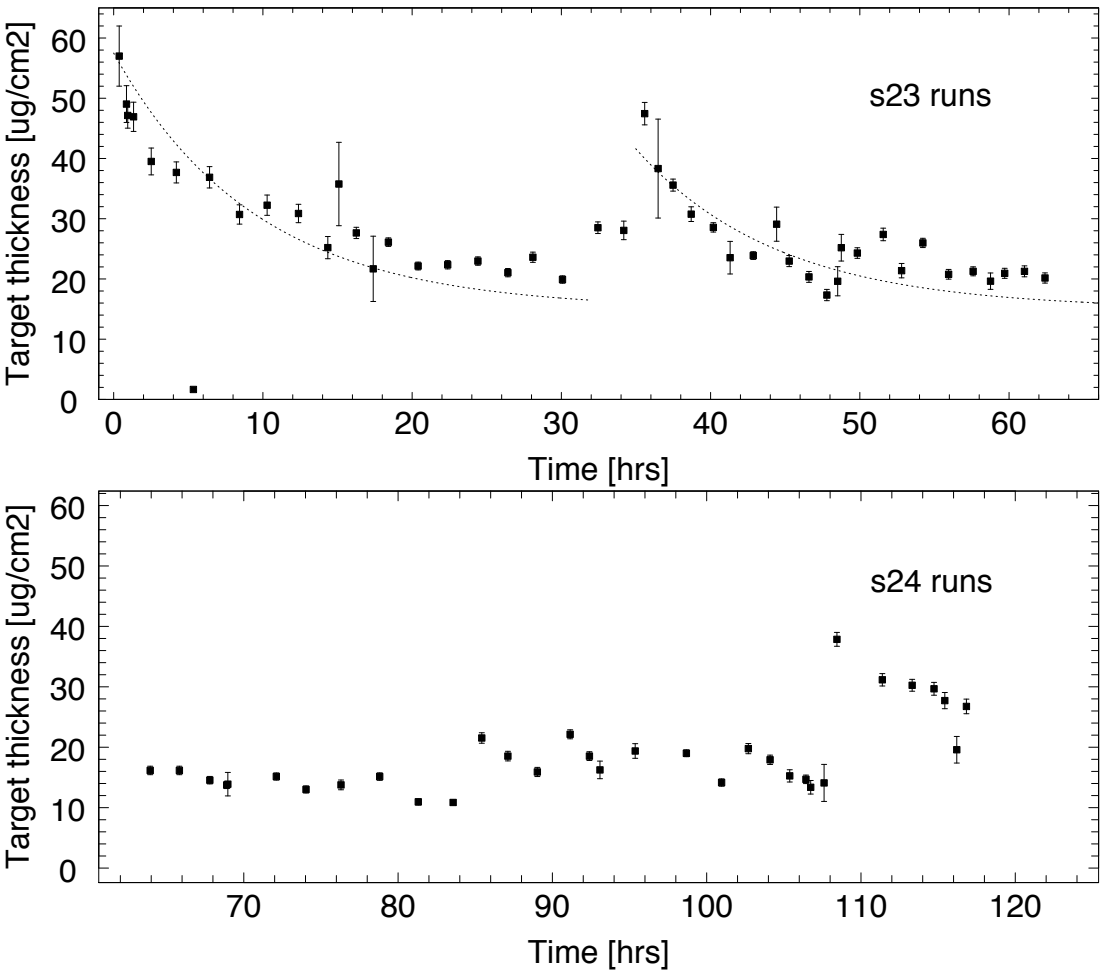

Figure 5.1: Time dependence of the deuteron content of the target during the experiment, obtained by tracking the time evolution of the ratio between the intensity of the 3004 keV line and the faraday cup beam intensity measurement. The dotted lines are exponential decays with a flat background assuming an initial thickness of 57 μg/cm^2, they are drawn to guide the eye.

5% systematics uncertainties on the faraday cup measurements, a 16% systematic uncertainties from the original target thickness measurement (at 57(9) μg/cm^2, see Section 4.2.2) the overall experiment systematics uncertainty is estimated to be 19%.

5.2 Detector shadowing

As can be seen on Figure 5.2 the number of counts in the 3004 keV line steadily evolves. But especially for detector s2-2 (but also s2-1) the outermost annuli are counting too low resulting in a sharp drop of the the line's intensity that would not be explained by solid angle considerations. This is due to detector shadowing.

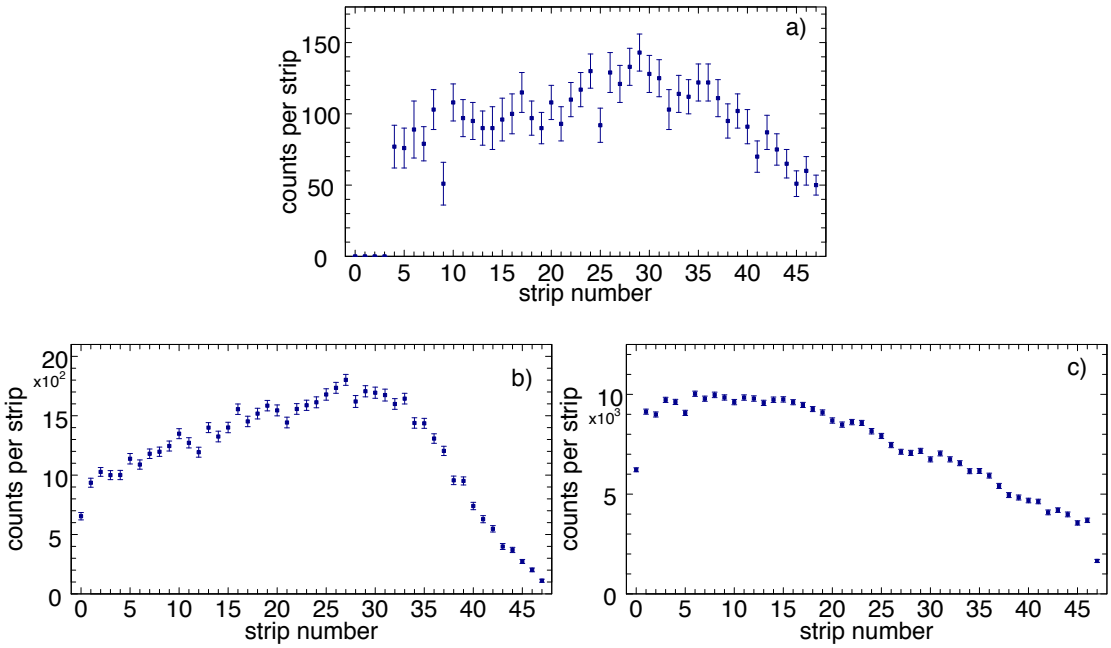

Figure 5.2: Number of counts in the 3004 keV peak per strip for detector a) s2-1, b) s2-2 and c) s2-3. In s2-1 the shadowing is obvious from strip number 37 while the first 4 strips (0 to 3) are not working; in s2-2 the shadowing impacts strip above number 32 while strip number 0 seems to be counting low and is ejected from further analysis; in s2-3 there is, as expected from Figure 5.3, no sign of shadowing but strips 0 and 47 behave sensibly differently from the rest of the detector and are ejected from further analysis.

The shadowing of certain annuli can be explained by two experimental factors. The most prominent effect is due to the use of collimators in order to avoid the detectors being hit by the beam, which incidentally shadows a section of the otherwise available solid angle. Consequently the closest detector to the target – remembering that the detectors were placed upstream – is the most impacted as it is positioned at very low angle from the position of the beam production. This effect is shown schematically on Figure 5.3. The second explanation is a slight non-concentricity of the three detectors. Though this is hard to verify as experimentally it would have similar effect to a non-perfect beam alignment, whose effects will also be discussed in a later section.

In addition to this phenomena, several strips in each detectors (or their associated ADC) are clearly misbehaving, appearing almost dead. Combining this with detector shadowing leads to a selection for the strips that would be considered for further analysis: strips 4 to 36 in s2-1, strips 1 to 31 in s2-2 and strips 1 to 46 in s2-3/4.

Similar shadowing is observed by exposing the detectors to the triple-α source. Due to the lifetime of the species in presence, hyperfine interaction damages

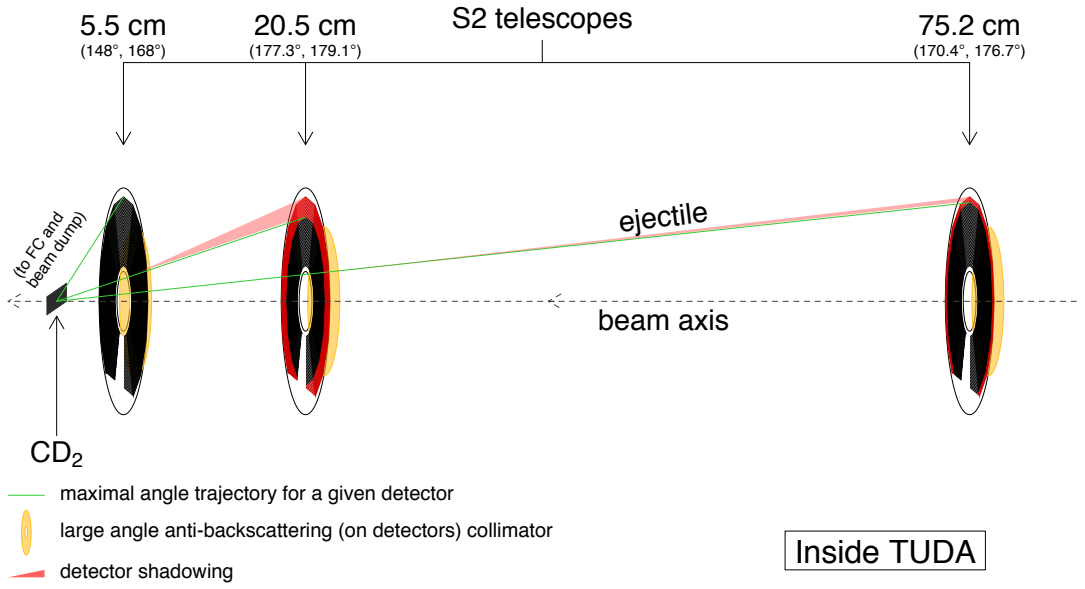

Figure 5.3: Schematic representation of strip shadowing by beam collimators.

the alignment of the emission and the number of counts for α-particles in each strip should only follow the solid angle distribution. It does only vaguely, as can be seen in Figure 5.4, where strips have been grouped together following the acceptance/rejection requirement presented above. Indeed slight but not insignificant differences between the expected solid angles and the α-particles distribution can be seen. Following the lack of explanation on the procedure used to measure the α spectra in the experiment (source position etc.) it was decided to only used solid angles calculated from the geometry of the experiment rather than scaling the distribution of the peaks on that of the α-particles.

5.3 Calibration & gain matching

5.3.1 Gain matching

The amplifier outputs revealed what seems like a functional behaviour for the amplifier offsets, while one expects a random distribution. This could indicate an underlying physical effects. Several options have been considered. It was first thought that this would be the consequence of a non centred beam. A schematic of such an effect is shown in Figure 5.5. The following angle correction was introduced to account for this possibility, using the notation of Figure 5.5:

$$\theta = \arctan\left(\frac{\sqrt{d^2 + r^2 + 2d\ell\cos\left(s_r \times \frac{2\pi}{16}\right)}}{\ell}\right), \tag{5.1}$$

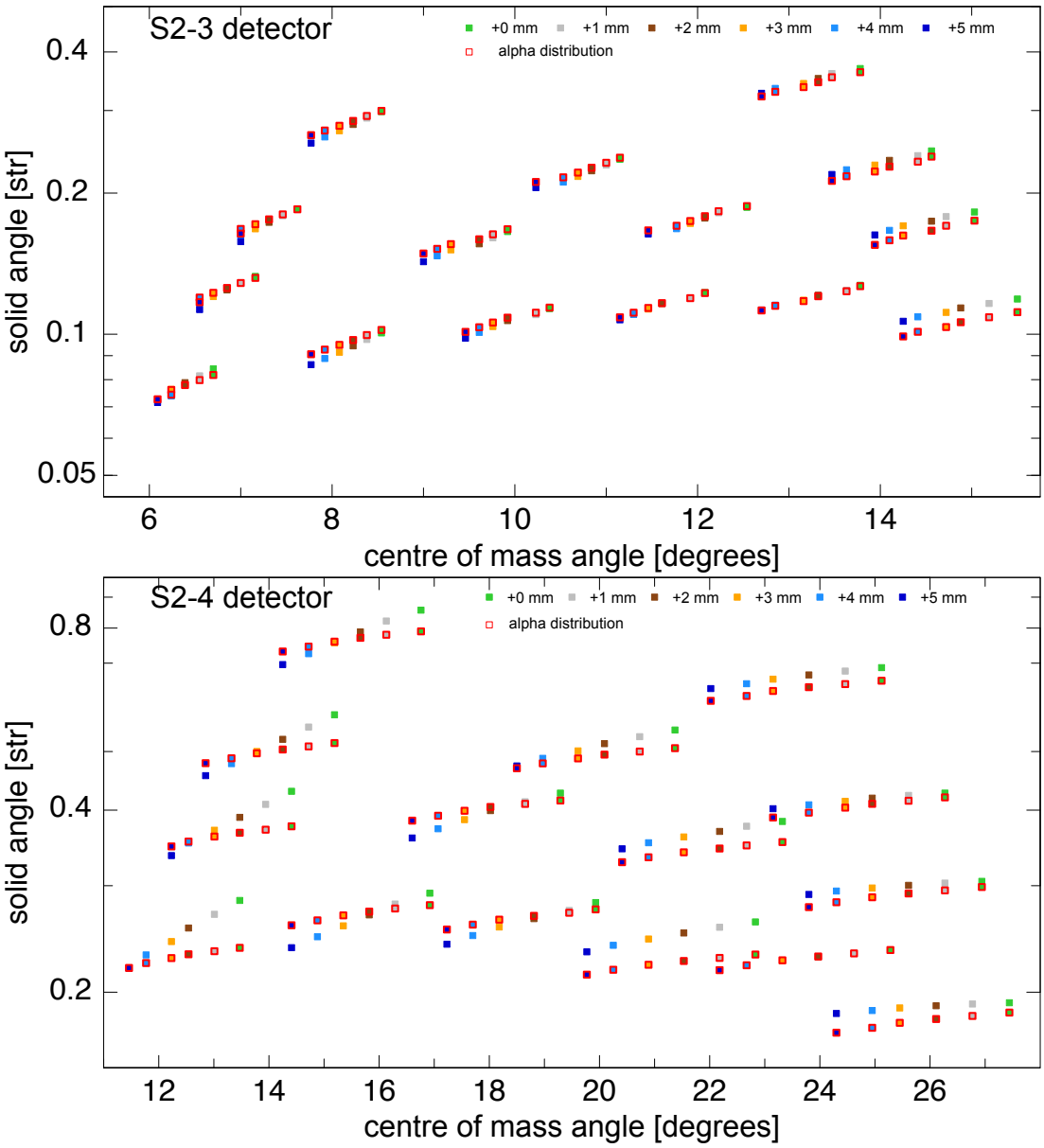

Figure 5.4: Comparison between the angular evolution of the number of counts of α-particles and the geometric solid angle for different group of strips and varying the detector distances compared to the logbook numbers (represented by the +0 mm points). The α-particles count is scaled to the solid angle value for the group of strips 31 to 39 in both s-3 and s2-4 (this sits at 24°).

where ℓ represents the distance from the centre of a collimator to the centre of a detector, d the possible displacement, s_r the sector's number and r the distance to the centre of the detector. Displacements of the beam spot, d, from 0 to 3.2 mm were considered for each sector, but none gave satisfactory reproduction of the observed behaviour. A rough alignment was obtained summing the outputs, but it resulted in measurably broader peaks than obtained in a single annulus. Consequently the annuli were adjusted such that the 3004 and 6512 keV peak would align. Each ADC (amplitude to digital converter) has a zero offset (*i.e.* the 0 energy would not be on 0 channel) and a gain, the number of channels that represent one unit of energy (in keV). By fixing the position of two known and isolated peak to the same channel number in all ADC outputs, a linear correction is obtained for each. This is the gain matching procedure routinely used in γ-ray spectroscopy. When using an array of several detectors, such as CAESAR at the Australian National University (see, for example, Ref. [Margerin 2012]) or GAMMASPHERE at the Argonne National Laboratory, it is critical to perform such alignment since the width of the peaks are often smaller than the maximal difference of the lines' position between two detectors. Here the amplitudes of the variations for the two peaks at 3004 and 6512 keV, were observed to be only 2 to 3 channels, but this corresponds to nearly 30 keV (see the following paragraph on calibration), for detector s2-2 (at 20.5 cm). This is only slightly smaller than the width of the 3004 keV peak, 33 keV, highlighting the need to use of this method.

5.3.2 Calibration

The goal of energy calibration is to translate the signal output of the amplitude to digital converter (ADC), a channel number, into energy. Typically a linear calibration is often sufficient, and, although second degree effects can also arise, the energy calibration was first made using a linear equation:

$$\text{Energy [keV]} = \text{ADC gain [keV/channel]} \times \text{channel} + \text{ADC offset [keV]} \quad (5.2)$$

As the annuli were gain matched on the 3004 and 6512 keV peaks, calibration is expected to be quite accurate between those energies. This can be seen on Figures 5.6.a) & b), with the residuals amplitude below 0.5 and 2 keV, respectively. However, because higher energy peaks are wider and are more weakly populated, their inclusion increases the uncertainty in the calibration. Yet there is no sign of distortion in the residuals when several extra peaks are taken into account, see Figure 5.6.c), although the residuals amplitude reaches 5 keV. For energies below

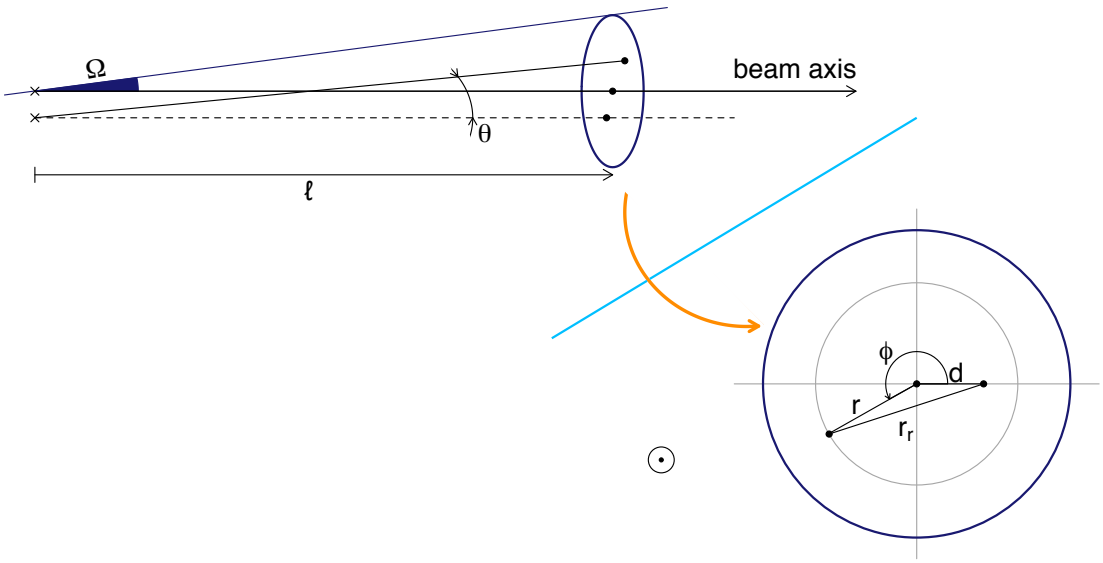

Figure 5.5: Geometry envisaged for explaining the unexpected annuli relationship with the energy of the peaks. The region available for displacement due to the presence of collimators is limited to the corresponding solid angle represented by Ω and the dark blue area on this diagram.

8 MeV, the calibration of Figure 5.6.a) is therefore adopted. Above 8 MeV, and even more above 10 MeV, the situation is more complex, ideally further lines could be included in the calibration. The selectivity of (d, p) reaction, favouring $s_{1/2}$ and to a lesser extent $d_{5/2}$ and $p_{1/2}$ transfers, reduces the number of observed high energy states to around thirty (see next section), but it is of no help here as no spin and/or parity assignments for any states above 10 MeV in ^{27}Al is known whatsoever. Consequently it is not possible to match observed to known states, this will be seen again below, even when the latter are determined to better energy precision. Another effect is that the uncertainty on the excitation energy of states beyond the region of calibration will gradually increase. Adopting the low energy calibration at higher energies further assumes that no distortion in the calibration would be present at low proton energies (high excitation energies). Although there is no sign of such effects, this assumption is not necessarily accurate and many factors could explain a non-linear behaviour of the energy calibration at low proton energies (high excitation energies).

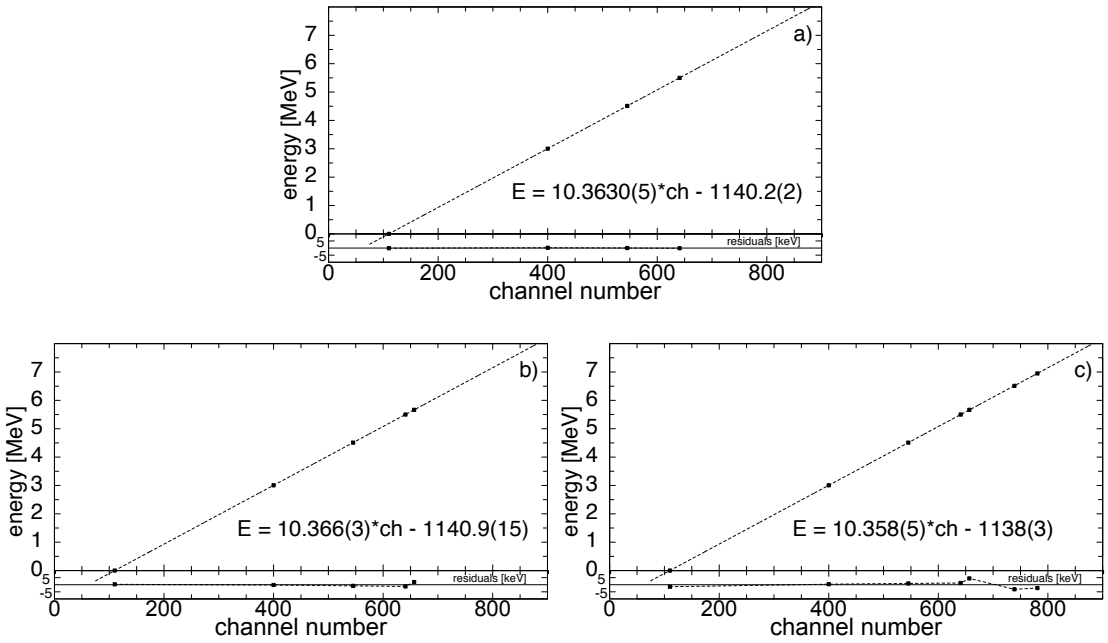

Figure 5.6: Calibration of s2-2 using peaks from 0 MeV (ground state) to (a) 5.500 MeV, (b) 5.667 MeV and (c) 6.948 MeV. The lower part of each plot shows the residuals.

5.4 Proton spectra, identification of observed lines and angular distribution

5.4.1 $\mathbf{E_{exc}}$ = 0 to $\mathbf{S}_p$ = 8.271 MeV

The typical proton spectra for each detectors is presented in Figure 5.7, each figures is made by grouping together the 24 innermost strips of each detectors. As can be seen thereon detectors s2-2 and s2-3 provides the best energy coverage, this is because the energy resolution, the background level and the solid angle are ideal for extracting independent states up to around 8 to 10 MeV. The very low geometric efficiency for detector s2-1 (at ≈75 cm) means that only the strongest lines are observed. The positioning of detector s2-4, at ≈3 cm from the reaction locus, results in a broader width for the detected protons (since the solid angle of each annuli is much larger). Therefore only the two states at 3004 and 4510 keV could be accurately studied in s2-4. Lines at 5500 and 5667 keV states can also be investigated for smaller grouping of the most innermost strips. Nevertheless angular coverage from 0 to 15 degrees in the c.o.m. is achieved for most states from 0 to 8.1 MeV.

Angular distributions for all states in this energy region will be shown in Section 5.5. In the immediate following, only several examples are extracted. A

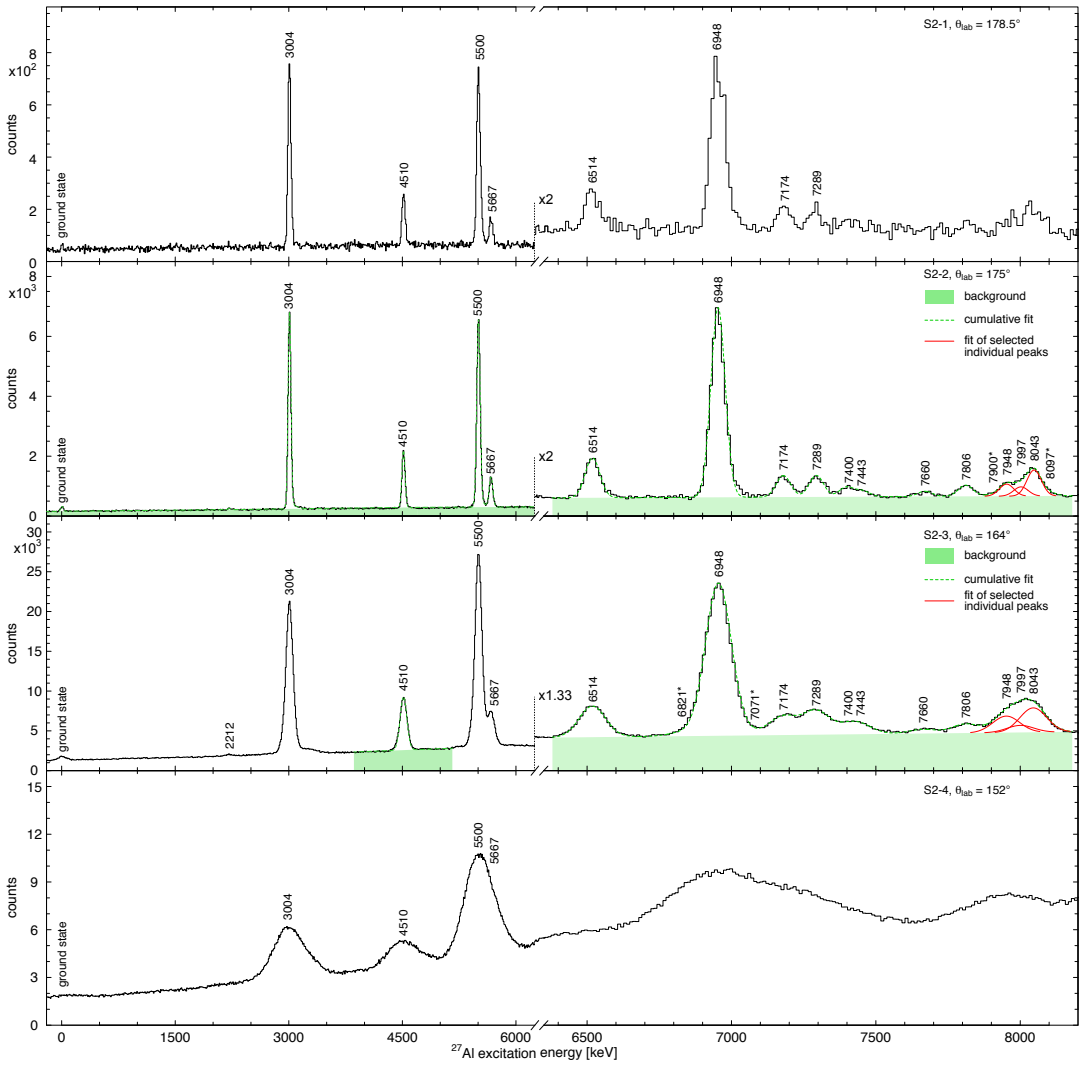

Figure 5.7: Typical excitation spectrum for the energy region $0 \lesssim E_{exc} \lesssim 8.1$ MeV, for each of the 3(+1) detectors. Note that the axes are discontinuous in order to gain clarity in the 6 to 8.2 MeV region.

full list of observed states from 0 to 8.1 MeV is presented in Table 5.1.

The states at 3004 and 4510 keV

The two lines at 3004 and 4510 keV are the only lines seen isolated from other peaks in every spectrum that can be made from the four detectors. Consequently they are very good examples of the effectiveness of the experimental set up. The angular distributions for both states are presented in Figure 5.8. In the plot of the angular distribution for the 3004 keV state, a comprehensive depiction of the effect of the different sources of uncertainty is presented. It can, in particular, be seen that the amplitude of the distribution at low angles ($\approx$0 degree) is mostly unaffected by the detector distance uncertainty while the impact is larger at

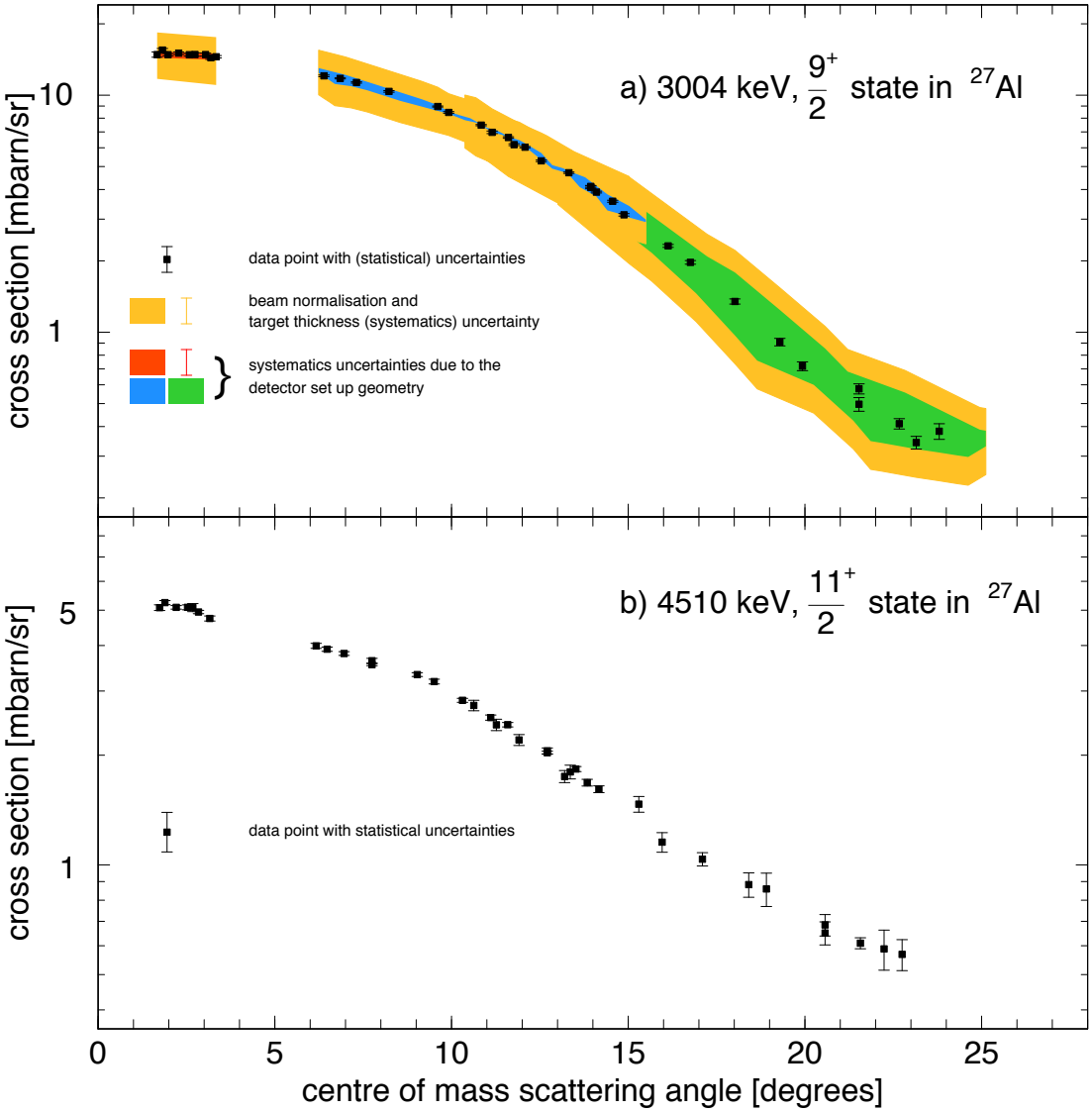

Figure 5.8: Angular distribution for excited stated in ^{27}Al at a) 3004 and b) 4510 keV. In a) both statistical and systematics uncertainties are displayed.

higher angles ($\gtrsim$18 degree).

Main states involved in the destruction of ^{26}Al in AGB and WR stars

In Section 2.1.5, the main (mirror) states involved in the amount of ^{26}Al generated by AGB and WR stars were presented. They are the 7790 keV, $5/2^+$ [Lotay 2011], the 7798 keV, $3/2^+$ [Basunia 2011], the 7806 keV, $9/2^+$, the 7948 keV, $11/2^+$ and the 7997 keV, $(9/2, 11/2)^-$ states. In Figure 5.9, a closer look at the proton spectrum as measured by s2-2, at 175° in the laboratory frame and $\approx$2° (this depends on the line's energy) in the centre of mass frame, is shown with a fit of the observed lines and the associated residuals. Inspection of these

Table 5.1: List of states observed in the energy region $0 \lesssim E_{exc} \lesssim 8.1$ MeV.

E_{state} [keV]	J^π	E_{state} [keV]	J^π
0	$5/2^+$	7289	$(13/2^+)$
2212	$7/2^+$	7400	$11/2^+$
3004	$9/2^+$	7444	$(13/2)^+$
4510	$11/2^+$	7664	$(7/2)^+$
5500	$11/2^+$	7806	$9/2^+$
5667	$9/2^+$	7948	$11/2^-$
6514	$9/2^+$	7997	$11/2^-$
6948	$11/2^+$	8043	$9/2^+$
7174	$9/2^+$		

residuals shows little, if no, signs of any line contaminating the 7806 keV peak. There is a potential 90(60) excess counts at 7773 keV (assuming the excess in residuals represents the peak's height and modelling a peak with such a height given the width of surrounding observed peaks), but this excess is only seen in this spectrum. Nevertheless it illustrates the detection limit of the experiment. The angular distribution obtained from fits of the proton spectra in which the 7806 keV line could be resolved is presented in Figure 5.10.

5.4.2 $S_p = 8.271$ MeV $\lesssim E_{exc} \lesssim 11$ MeV

For higher energy lines the situation gets more complex as the energy calibration deteriorates with energy. Many peaks can yet be fitted using parameters from well known lines at lower energy, such as the energy dependent width, resulting in the general fit of Figure 5.11. To help assigning observed lines to known states, a sorting of states to consider can be made by taking into account the energy accuracy (here from calibration b) of Figure 5.6), and the validity of suggested assignment in known work (see Section and the case of the 7948 keV, $11/2^-$ state):

- the 8403 keV line is likely the 8396(1) keV, (11/2) state [Lickert 1988];
- the 8422 keV line, the 8421(1) keV, $(3/2, 5/2)^+$ [Champagne 1990] which, given the firm parity assignment, would *de facto* suggest $(5/2)^+$ due to the amount of spin transfer ($\ell = 4$) needed to make $3/2^+$;
- the 8490 keV state convincingly agrees with the known 8490(1) keV, $5/2^+$ state [Iliadis 1990, Buchmann 1980, Champagne 1990] and the relative weakness of the peak is not inconsistent with a $d_{5/2}$, $\ell = 2$ transfer;

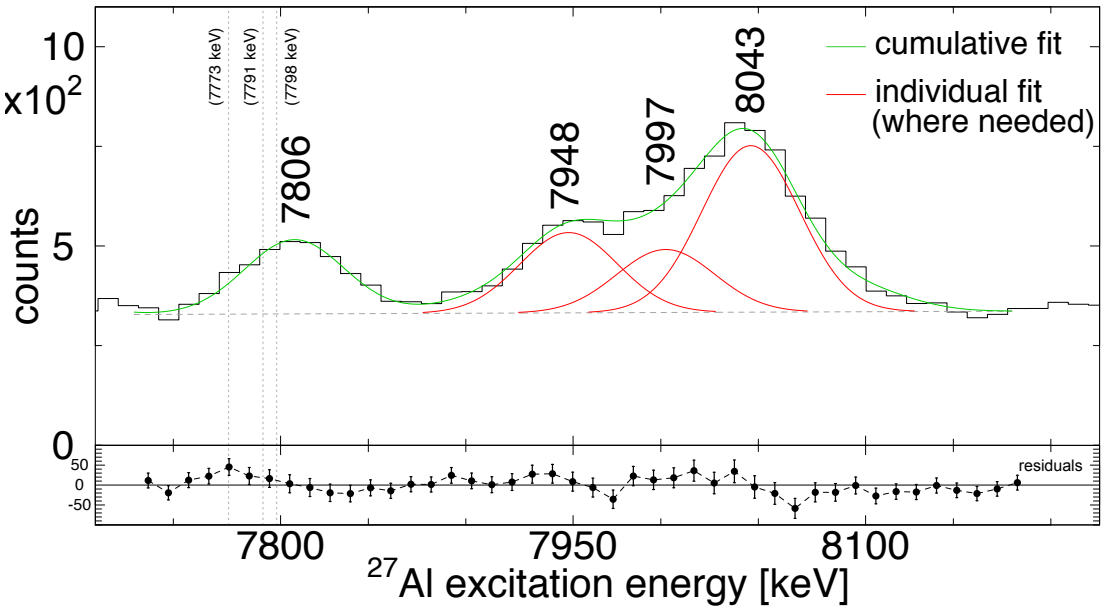

Figure 5.9: Expanded view of the excitation energy spectrum showing states in the region E_{exc} = 7700−8200 keV. The green line shows a cumulative fit to the data. The red lines indicate the individual fits for the 7948, 7997, and 8043 keV levels with fixed peak widths, and the background is displayed by the horizontal dashed lines. Vertical dotted lines show the position of known states of potential significance but not seen in this analysis. Residuals are shown below the spectrum.

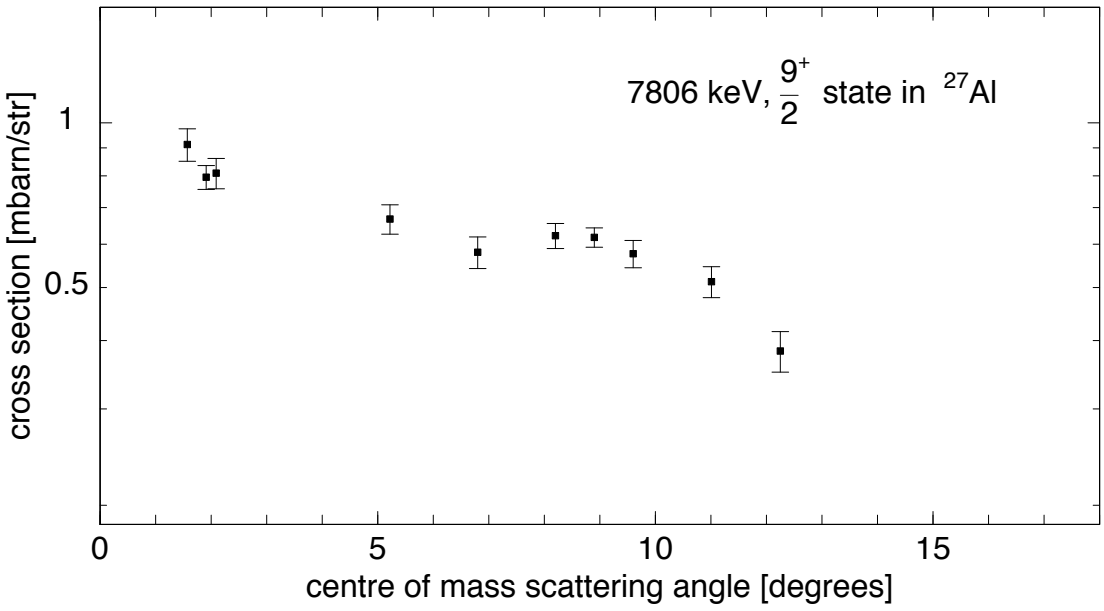

Figure 5.10: Angular distribution for the excited stated in ^{27}Al at 7806 keV.

- a 8521 keV line is observed that could be the 8521(2) keV, (1/2, 3/2, 5/2, 7/2) state [Moss & Sherman 1976];

- a state at 8598(3) keV with a suggested spin (3/2) is known but the parity is firmly assigned as negative [Iliadis 1990, Champagne 1990] and it seems unlikely that such a transfer could be observed with the present (d, p) reaction especially seeing that, at low energy where the spectra are not too busy, known low spin, negative parity states are not observed;

- the line at 8696 keV which sits relatively alone could correspond to the known 8693(3) keV, (9/2, 11/2, 13/2) state [Lickert 1988];

- the line at 9305(10) keV, could be the known 9299(3) keV state [Moss & Sherman 1976] or the 9308(1) keV, ($5/2^+$) state [Smit 1982];

- there is a known state at 9883(3) keV which would agree with the observed 9881 keV line;

- a very intense line at 10340 keV is observed, states at 10338(2) keV with a suggested $J^\pi = (1/2^+)$ and 10348(2) keV with a tentative assignment of $J = (3/2)$ have previously been observed [Smit 1982] but they are unlikely to actually match the state of the present work, due to the required amount of angular momentum to be transferred;

- a state at 10459(2) keV is known [Moss & Sherman 1976] but, due to the spin assignment of $J^\pi = (1/2^-)$, it is certainly not corresponding to the state observed here at 10464 keV;

- the doublet of lines at 10788 and 10830 keV have possible correspondents in the known (or at least reported, see Table 5.2) 10791(3) and 10833(2) keV states, see Ref. [Audi 2003].

Further possible assignments for states below E_{exc} = 11 MeV are shown in Table 5.2. This table include a fit rating which is derived from the stability of the centroid position in the different spectra. For example the line at 9503 keV seems quite strong. However while it is seen as one peak in s2-3, the line is undeniably made of at least two peaks in s2-2. This can visually be inferred by the broader width of the line at 9503 keV compared to neighbouring peaks such as, for example, the line at 9881 keV, see Figure 5.11. Consequently this fit would not be assessed as good, hence rated "red", and is excluded from further discussions. Similarly all red and orange rated peaks will not be subject of further analysis.

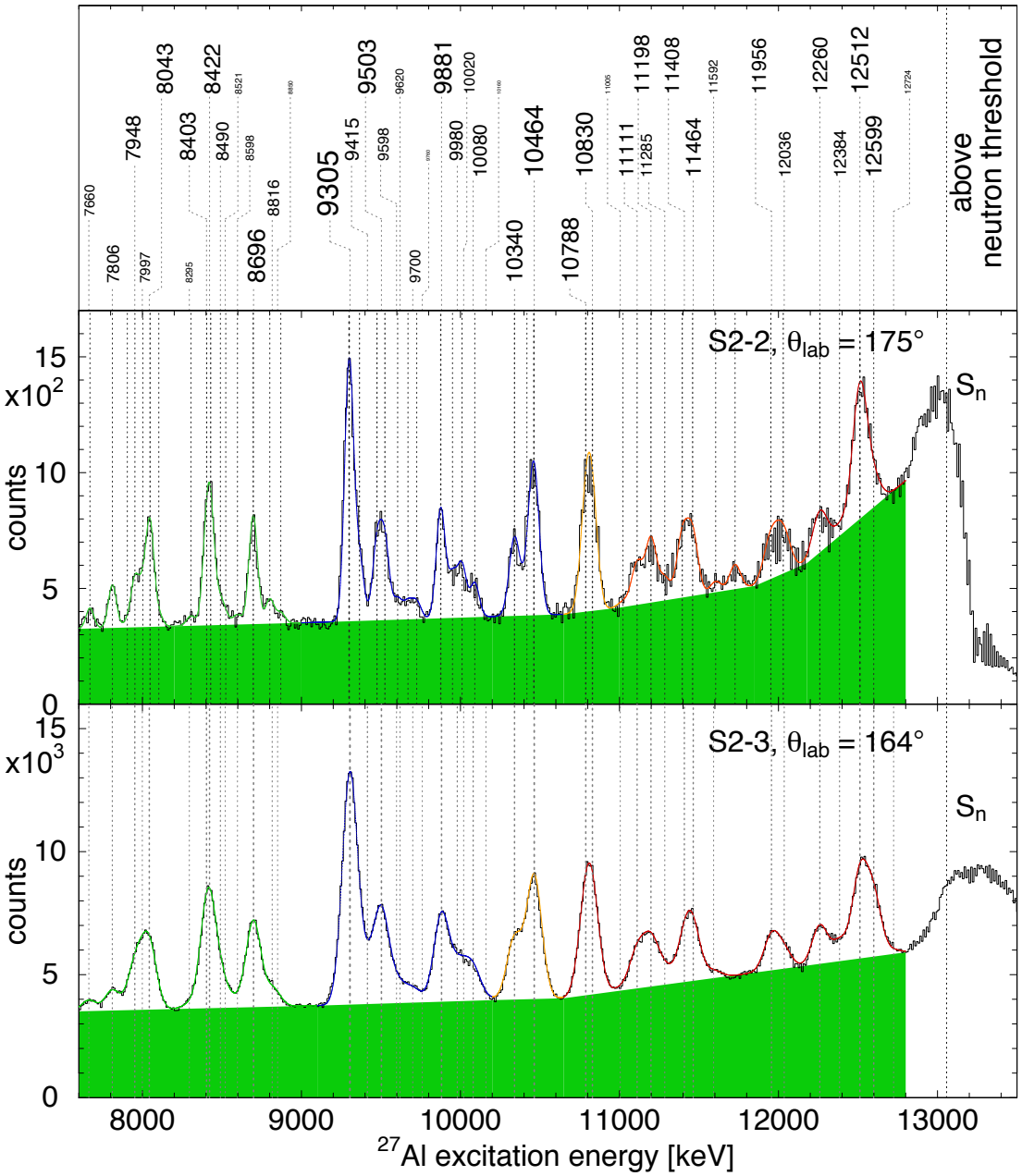

Figure 5.11: Excitation spectra in the energy region from E_{exc} ≈8 MeV to the neutron emission threshold S_n, obtained by clustering the 24 innermost annuli of detectors s2-2 and s2-3. The green shadow indicates the background level, the spectra are superseded by a manual and piece wise fit represented by the variant colours, with each colour attributed for one "piece". The top panel gives the energy values of the lines needed for the fit, the size of the labels is logarithmically weighted on the line intensity as observed, the E_{exc} ≈8 MeV region is shown as an indication of the intensity of the high energy lines.

Table 5.2: List of states whose energy match that of lines required in the general fit of Figure 5.11. The 5$^{\text{th}}$ column represents the fit quality. Only fit rated green will be later discussed. The quoted references are only those where the most elaborated assignment is attempted. Note that known energies refer to the energies in the ENSDF database [Basunia 2011] and not necessarily that of the quoted references.

E [keV] this work	E [keV] known	J^π	Reference(s) (apart from A)	Fit rating
8403	8396(1)	(11/2)	B.a) & B.b) (J)	
8422	8420.7(10)	$(3/2, 5/2)^+$	C ($(J)^\pi$)	
8490	8490.3(12)	$5/2^+$	D (J), E ($J^{(\pi)}$), C (π)	
8521	8521(2)	$(1/2^+$ to $7/2^+)$[a]	B, F	
8598	8598(3)	$(3/2)^-$	D ($(J)^\pi$), C ($(J)^\pi$)	
8696	8693(3)	(9/2 to 13/2)	B.a) (J)	
8850				
9305	9299(3)		F	
	9308.2(9)	$(5/2^+)$	G ((J^π))	
9415				
9503				
9598				
9620				
9700				
9760				
9881	9883(3)		F	
9980				
10020				
10080				
10160				
10340	10338(2)	$(1/2^+)$	G ((J^π))	
	10348(2)	(3/2)	G ((J))	
10464	10459(2)		F	
10788	10791(3)		A[b]	
10830	10833(2)	$(3/2^+, 5/2^+)$	A[b]	
	10835(2)	$(3/2^+, 5/2^+)$		
	10836(2)	$(5/2^-, 7/2^-)$		
	10838(2)	$(3/2^-)$		

[a] This is given in ENSDF [Basunia 2011] and referenced in [Lickert 1988], yet no source for the tentative assignment has been found in the therein references.
[b] No article listed in ENSDF [Basunia 2011] does present any of those energies and J^π assignments...
D. [Iliadis 1990], ^{26}Mg(p, γ)^{27}Al. E. [Buchmann 1980], ^{26}Mg(p, γ)^{27}Al.
C. [Champagne 1990], ^{26}Mg(^{3}He, d)^{27}Al. A. ENSDF [Basunia 2011].
F. [Moss & Sherman 1976], ^{27}Al(p, p')^{27}Al. G. [Smit 1982], ^{26}Mg(p, γ)^{27}Al.
B. [Lickert 1988], a) ^{24}Mg(α, $p\gamma$)^{27}Al, b) ^{26}Mg(p, γ)^{27}Al.

5.4.3 $E_{exc} \gtrsim 11$ MeV

Above 11 MeV, there is no states listed in ENSDF. Several experiments have unveiled states in this energy region, for example the recent ^{27}Al(p, p')^{27}Al experiment reported in Ref. [Benamara 2014], or the older studies of the ^{26}Mg(p, γ)^{27}Al [Westerfeldt & Mitchell 1978] and the ^{23}Na(α, γ)^{27}Al [deVoigt 1971a, deVoigt 1971b] reactions. This energy region will be discussed in more details below with the presentation of angular distributions.

5.5 Transfer assignments and spectroscopic factor measurements

In this Section, angular distributions obtained from analysis of the proton spectra discussed above are compared to the results of a finite range adiabatic wave calculation conducted with the code `TWOFNR`. The details of the calculation, including the choice of parameters, were developed in Section 3.3, and methods for obtaining spectroscopic factors from such calculation were presented therein as well. In summary, the scaling factor that exists between the calculated and the experimental differential cross sections equates the C^2S coefficient. In most cases, the experimental cross sections have pronounced behaviour making the transfer assignment – pure $\ell = 0$, $\ell = 1$, $\ell = 2$, etc. – obvious. In order to extract the spectroscopic factor a χ^2 fit was conducted where deemed reasonable. For high excitation energy states, it becomes increasingly complicated to distinguish between $\ell = 1$ and $\ell = 2$ distribution over the range of angles experimentally covered, see Section 3.4.2 of Chapter 3. Indeed a χ^2 optimisation would not yield any clear direction towards which angular momentum transfer is observed. Consequently fits are just given as an indication and it is not possible to deduced any spin or parity for distribution where $\ell = 1$ and $\ell = 2$ is possible, often the only suitable statement is that the transfer must have $\ell < 3$. The cases for $\ell = 0$ are more stringent. Angular distributions are presented in Figures 5.12 to 5.19 alongside the calculations with the optimised scaling factors, with the list of these presented in Table 5.4.

5.5.1 The 3004 keV state

Figure 5.12 shows the angular distribution for the most strongly populated $9/2^+$ state at 3004(2) keV in ^{27}Al which is predicted to be a relatively pure shell model configuration dominated by $\ell = 0$ transfer, this will be shown later in

Table 5.3: Tentative energy assignments for lines required in the general fit of Figure 5.11. The 5$^{\text{th}}$ column represents the fit quality. Only fit rated green or orange will be later discussed. The quoted references are only those where the most elaborated assignment is attempted, in the column the letters refer to the same letters as in ENSDF, while the detail of the reference are given under the table.

E [keV] this work	E [keV] known	J^π	Reference	Fit rating
	11000(4)		H	
11005	11010(4)		H	
	11010.7(30)	$1/2^-$	I	
	11106.7(30)	$(5/2, 7/2)^-$	I	
11111	11108(4)		H	
	11112(4)		H	
	11115.8(30)	$(3/2^+, 5/2^+)$	I	
11198	11195(4)		H	
11285	11273(4)		H	
11408	11406(4)		H	
11464	11456(4)		H	
11592	11595(4)		H	
11956	11957(4)		H	
12036	12024(4)		H	
12260	12260(4)		H	
12384	12384.0(15)	$11/2^{(+)}$	J	
	12392(4)		H	
	12504(4)		H	
12512	12505(2)	$\gtrsim 7/2$	J	
	12514(4)		H	
	12518(2)	$\gtrsim 7/2$	J	
	12591(4)		H	
12599	12596(3)	$(7/2^+)$	J	
	12603(4)		H	

References:
H. [Benamara 2014], ^{27}Al(p, p')^{27}Al
I. [Westerfeldt & Mitchell 1978], ^{26}Mg(p, γ)^{27}Al
J. [deVoigt 1971a] & [deVoigt 1971b], ^{23}Na(α, γ)^{27}Al

Chapter 7. This low angles distribution is, indeed, well reproduced by the ADWA calculation with pure $\ell = 0$ transfer and a high spectroscopic factor, C^2S= 0.49. The distribution at higher angles can be fitted with the inclusion of a $\ell = 2$ component for the transferred proton. This would be from the $1d_{5/2}$ orbitals and the corresponding C^2S from the fit presented in Figure 5.12 is 0.18.

5.5.2 The 7806, 7948, 7997 and 8043 keV state

Figure 5.14 presents the angular distribution for the $9/2^+$ 7806(3) keV state, which corresponds to the mirror analog of the 127 keV resonance at an excitation energy of 7590 keV in ^{27}Si [Lotay 2009]. From comparison with `TWOFNR` calculations, it is evident that the most forward angle component is predominantly $\ell = 0$ transfer, while an additional $\ell = 2$ component is required in order to accurately reproduce the full distribution at less forward angles. A best fit is obtained combining $\ell = 0$ and 2 transfers with C^2S ($\ell = 0$) of $9.3(19)\times10^{-3}$ and C^2S ($\ell = 2$) of $6.8(14)\times10^{-2}$ for the 7806 keV state. This is significantly higher than the upper limit of 2.2×10^{-3} for $\ell = 0$ proton capture to the 7590 keV resonant state in ^{27}Si obtained in the ^{26}Al(^{3}He, d)^{27}Si study of Vogelaar *et al.* [Vogelaar 1996]. However, Parikh *et al.* [Parikh 2014] have suggested that the experimental limit of C^2S ($\ell = 0$) may be compatible with values up to a maximum of $\sim11\times10^{-3}$ for the 7590 keV state in ^{27}Si when the smallest scattering angle is discarded from the Vogelaar *et al.* data. The present result is, therefore, within the upper range of the value suggested by Parikh *et al.*, and using a C^2S ($\ell = 0$) of $9.3(19)\times10^{-3}$ implies a strength of 0.025(5) eV for the 127 keV resonance in the ^{26g}Al(p, γ)^{27}Si reaction (the error quoted for the strength represents a statistical error; there is also an uncertainty of $\sim$20% associated with possible differences between spectroscopic factors of analog states).

A detailed fit analysis of the 7806 keV peak was further performed to investigate potential excess counts contributing to the differential cross section around the energy region 7790 and 7798 keV, this was reported earlier, noticeably via the residuals in Figure 5.9. The analysis shown that the peak was entirely consistent with a single-state structure at an energy of 7806(3) keV, in agreement with the value of 7807.2(10) keV reported in the γ-ray spectroscopy study of ^{27}Al by Lotay *et al.* [Lotay 2011]. In the energy region of interest for the 7806 keV level in ^{27}Al, there are two potential excited states at 7790.4(7) [Lotay 2011] and 7798(2) keV [Basunia 2011], which have been previously assigned as $5/2^+$ and $3/2^+$, respectively [Lotay 2011]. This detailed analysis indicates there is no significant contribution to the observed differential cross section for the 7806 keV state from these two neighbouring excited levels. The 7790 keV state in ^{27}Al has

been assigned to a mirror analog in ^{27}Si, corresponding to a $5/2^+$ resonance at 68 keV in the ^{26g}Al$(p, \gamma)^{27}$Si reaction [Lotay 2011]. Based on the analysis above, an upper limit for C^2S ($\ell = 2$) of 1.6×10^{-2} is set, corresponding to a resonance strength of $\omega\gamma < 8\times10^{-10}$ eV.

The angular distribution and ADWA calculation for the 7948(3) keV excited state in ^{27}Al is shown in Figure 5.14. As can be seen, the angular distribution is well fitted by a pure $\ell = 1$ transfer with C^2S ($\ell = 1$) of 0.14(3) and is inconsistent with $\ell = 0$, 2 transfer. Such high values for C^2S for negative parity states at high excitation energies in *sd*-shell nuclei have been associated with relatively pure single particle configurations [Brown 2014]. Consequently the distribution and the associated calculation is supportive of an $11/2^-$ assignment.

Figure 5.15 shows the angular distribution together with a fit of the `TWOFNR` calculation to the experimental data for the 7997 and 8043 keV states. In both cases, the situation is relatively straightforward with an apparent $\ell = 1$ transfer for the 7997 keV state with an associated C^2S of 0.12 and $\ell = 0$ & 2 transfers for the 8043 keV state, with proton spectroscopic factor of 0.03 for the $2s_{1/2}$ wave and 0.13 for the $1d_{5/2}$ wave.

5.5.3 States above $E_{exc} = 8043$ keV and below the neutron threshold

The distributions for states above $E_{exc} = 8043$ keV are shown in Figures 5.15, 5.16, 5.18, 5.19 & 5.20. Amongst the lines selected for analysis in Tables 5.2 & 5.3 some have angular distribution clearer than others, allowing for a more comprehensive study than the energy matching assignment presented in the aforementioned tables.

The angular distribution for the transfer to the 8403 keV state is not very precise. Statistically, it could be either $\ell = 1$ or $\ell = 2$, even though one would still expect distinct behaviours at this energy, see Figure 3.15. Either of those assignments do not discard the correspondence to the 8396(1) keV state observed by Lickert *et al* [Lickert 1988]. However, seeing that this γ-ray study yielded a (11/2) suggested spin assignment for this state, $\ell = 1$ is more likely. (Note that to conserve the $\ell = 2$ possibility, it shall be mixed with an $\ell = 0$, this is possible, as it is possible that every $\ell = 2$ contains a very low, unmeasurable at the sensibility of this work, ratio of $\ell = 0$, although enough to change the final state's spin assignment.) This would imply that the spin and parity of the state is $J^\pi = (11/2^-)$.

A 8420.7(10) keV, $(3/2, 5/2)^+$ state was reported in the (^{3}He, d) study of

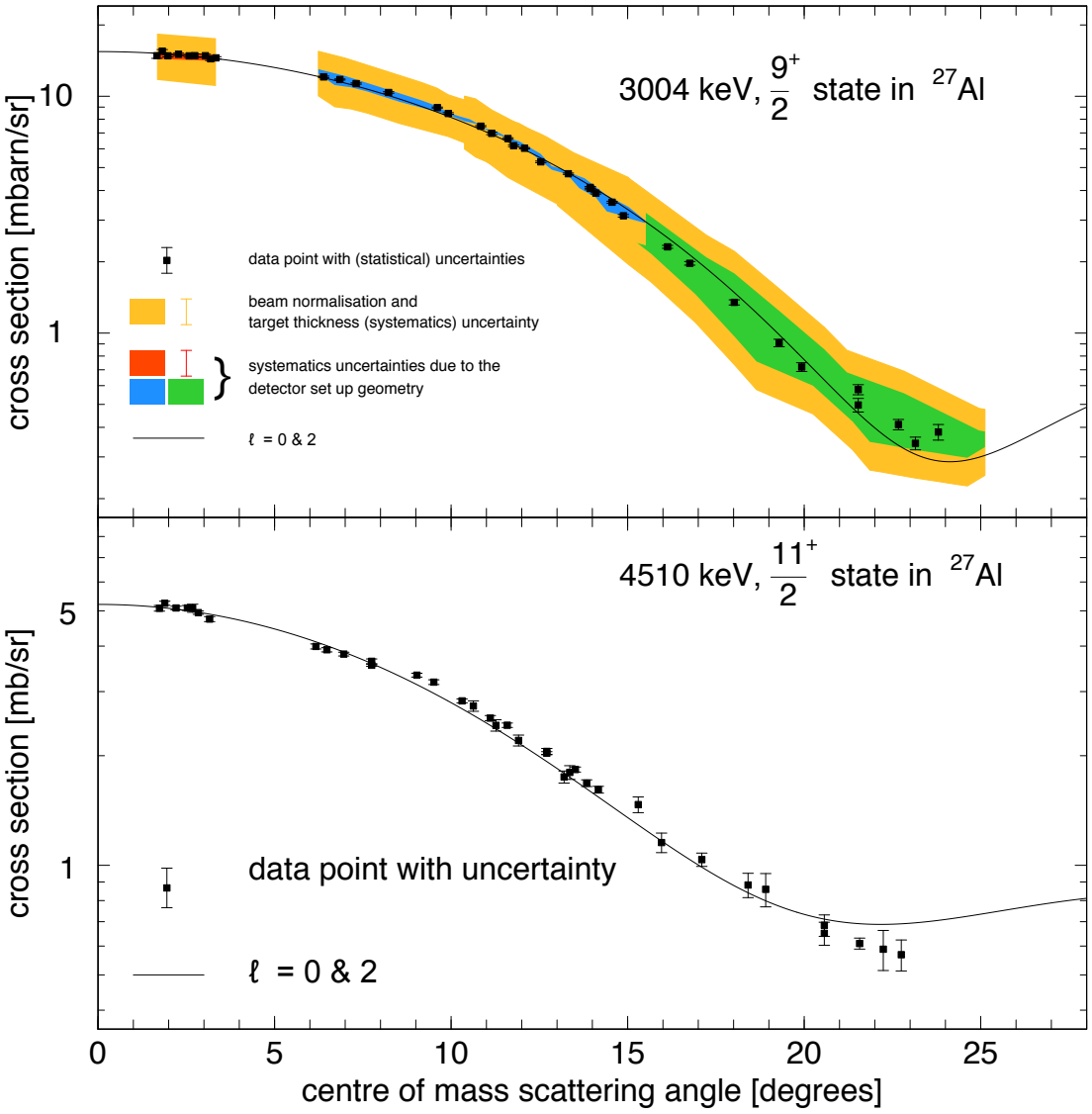
3004 keV, 9+/2 state in 27Al
data point with (statistical) uncertainties
beam normalisation and
target thickness (systematics) uncertainty
systematics uncertainties due to the
detector set up geometry
ℓ = 0 & 2
cross section [mbarn/sr]
10
1
4510 keV, 11+/2 state in 27Al
data point with uncertainty
ℓ = 0 & 2
cross section [mb/sr]
5
1
0
5
10
15
20
25
centre of mass scattering angle [degrees]

Figure 5.12

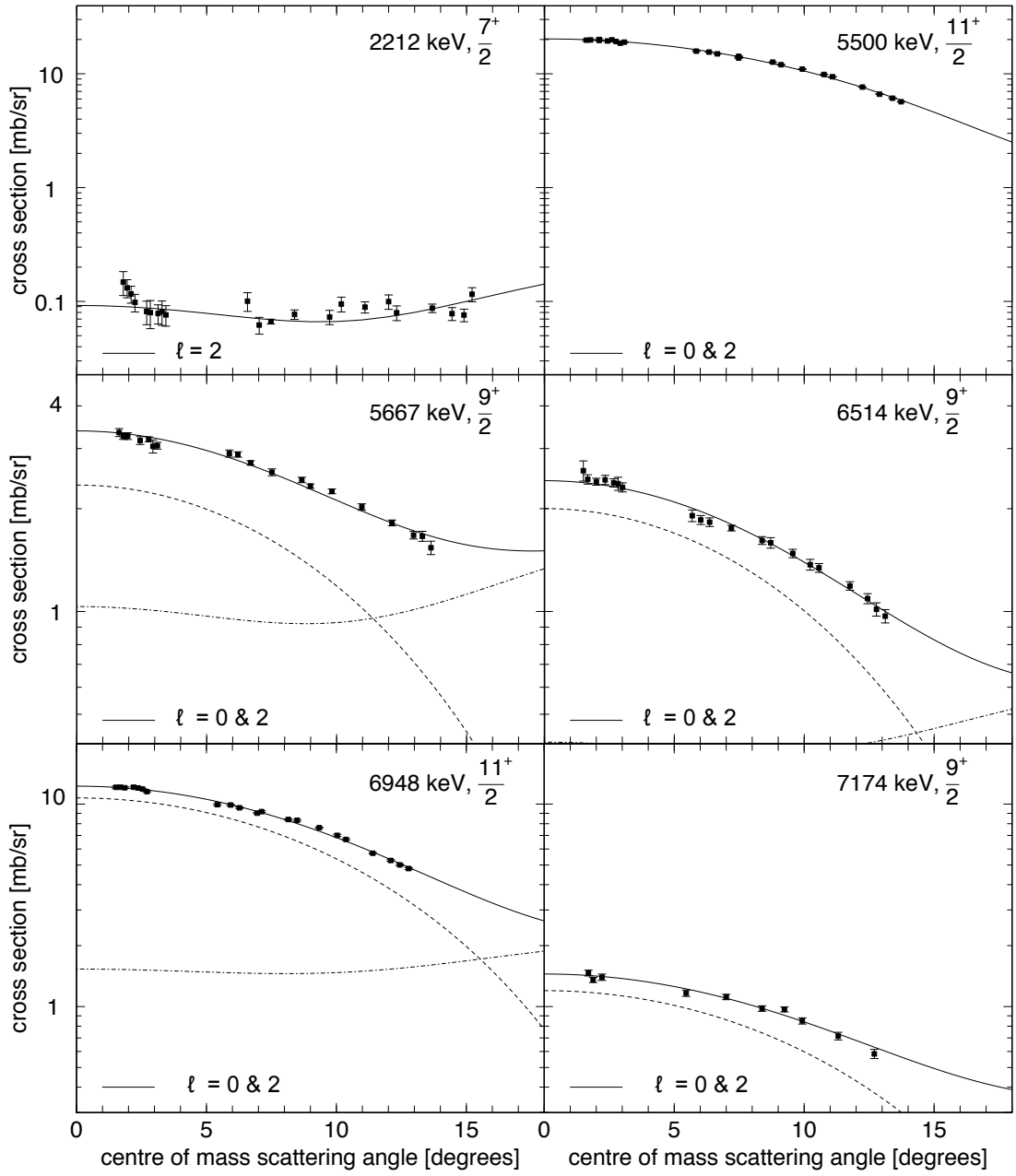

Figure 5.13: Angular distributions of excited states between 2.212 and 7.174 MeV. The spin and parity assignments presented in each figure is based on literature and transfer assignment from this work, and are those used for the TWOFNR calculation that resulted in the solid line in each panel.

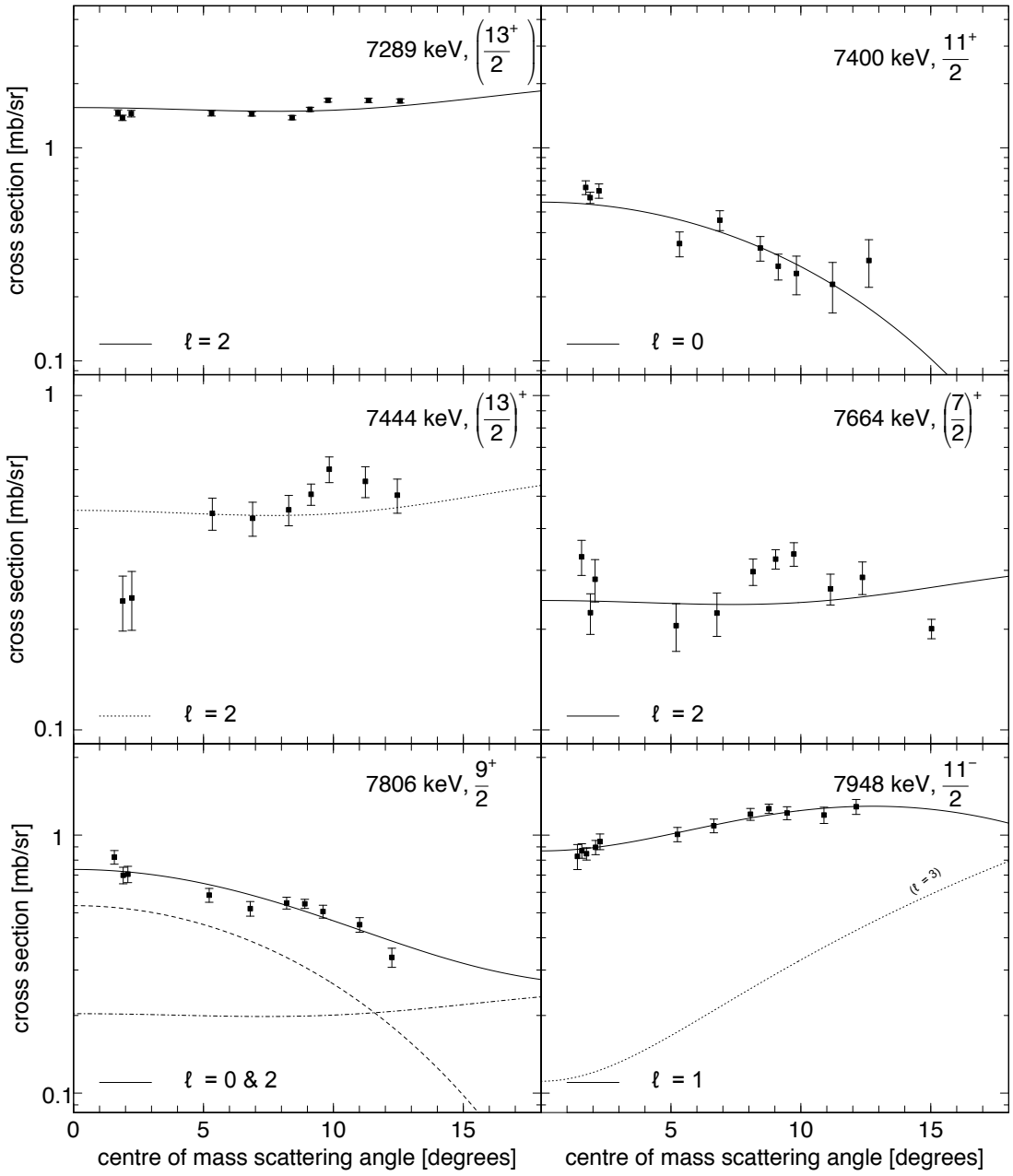

Figure 5.14: Angular distributions of excited states between 7.289 and 7.948 MeV. The spin and parity assignments presented in each figure is based on literature and transfer assignment from this work, and are those used for the TWOFNR calculation that resulted in the solid line in each panel.

Champagne *et al.* [Champagne 1990]. Here, a state at 8422 keV is observed, see Figure 5.15. The angular distribution of the proton transfer to this line is consistent with an $\ell = 2$ transition. An $\ell = 4$ transition would not be strong enough to be observed in (d, p) study, hence the suggested $J^\pi = (5/2)^+$ assignment. Similarly the angular distribution for the transfer to the 8490 keV, see Figure 5.15, does not disagree with the $\ell = 2$ assignment that should be observed if this line were the 8490.3(12) keV, (firm) $5/2^+$ state from Refs. [Iliadis 1990, Buchmann 1980, Champagne 1990].

While quite clearly measured in the proton spectra shown in Figure 5.11 (it skews the low energy side of the proton peak, i.e. the high energy side in the excitation energy of ^{27}Al scale), the 8521 keV was not enough populated to provide for a measurement of an angular distribution.

The angular distribution for the proton transfer feeding into the 8696 keV state in ^{27}Al suggests that it is $\ell = 1$, see Figure 5.15. This reinforces the correspondence to the 8693(3) keV state observed by Lickert *et al* [Lickert 1988], in their γ-ray spectroscopy study of ^{27}Al. Here the angular momentum of the state, $J \in (9/2, 11/2, 13/2)$ cannot be strictly narrowed by the transfer assignment, however, the parity π is very likely negative, although as it is often the case here a larger angular coverage would be required for a firm assignment. The 8693(3) keV state decays into the 8396 keV, (11/2) (and as just presented possibly $(11/2^-)$) and the 6948 keV, $11/2^+$, states, also observed here. The decay to the lower of these two states has a large enough energy, $E_\gamma = 1745$ keV, that many multipolarities could be justified without measurable lifetimes, but the γ-ray decay to the 8396 keV state requires a (non-forbidden) $E1$ or $M1$. If the spin were to be 11/2, then the 297 keV γ-ray from the 8693 to the 8396 keV would be a $J \rightarrow J$ transition, the A_2 and A_4 Legendre polynomials extracted from the angular distribution of the γ-rays emitted from the initial state would therefore be characteristics of $\Delta J = 0$, see, for example, Ref. [Margerin 2012]. Unfortunately if angular anisotropies were recorded by Lickert *et al* [Lickert 1988] none are reported for the decays of the 8693(3) keV state.

Two states are known with energies within the energy uncertainty of the observed 9305 keV state, they are at 9299(3) keV [Moss & Sherman 1976] and 9308.2(9) keV [Smit 1982]. The latter state was assigned with $J^\pi = (5/2^+)$. Here $\ell = 2$ cannot be strictly rejected but an $\ell = 1$ assignment for the transfer is more plausible, see Figure 5.16. Consequently it could be the 9299 keV state rather than the 9308.2 keV state. Note that the Moss & Sherman study is that of a (p, p') reaction, which is often used for its lack of selectivity, *i.e* it populates all spin regardless.

In Figure 5.16, the angular distribution for the 9881 keV line is presented alongside the fits for the $\ell = 1$ and 2 transfer calculations. It can be seen that discrimination between the two possibilities is not significant. And, when the potential match in the literature only has an energy assignment, here at 9883(3) keV [Moss & Sherman 1976], but no spin/parity information is provided, then drawing a tangible assignment is not plausible. This will be the case for all further lines even when only $\ell = 2$ or $\ell = 1$ is drawn in the corresponding figure.

The angular distributions for the 10340 and 10788 keV states observed in this work are extremely similar, with in both cases a mixed $\ell = 0$ & 2 transfer suggested in similar ratio of the $C^2S(\ell = 0)$ to $C^2S(\ell = 2)$, 0.04/0.08=0.5 and 0.06/0.1=0.6, respectively. For such mixed transfers the states must have $J^\pi \in (9/2, 11/2)^+$ (the parity is firm). There is no known states with this spin/-parity suggestion in the vicinity of 10340 keV, see Table 5.2. Potentially it is a new previously unknown state. A state at 10791(3) keV is reported in the ENSDF database [Basunia 2011] but no other information is known. Perhaps the 10788 keV state reported here, and that 10791(3) keV state are the same, perhaps they are not.

Observed between the two previously discussed states is the 10464 keV line. The angular distribution presented in Figure 5.16 for this state, tends to indicate it might be a mixed $\ell = 0$ & 2 transfer, although the ratio would be lower than for the 10340 and 10788 keV states. This can be seen visually as the drop in cross section, as the reaction becomes more peripheral, appears smoother for the 10340 keV than for the 10340 and 10788 keV lines. Here again a state is reported in the ENSDF database [Basunia 2011], $E_x = 10459(2)$ keV, but no other information has yet been obtained, such that it is not possible to assess whether this would be the same state as the one observed here at 10464 keV.

Between 11 MeV and the neutron separation energy

Most of the states above 11 MeV are known from the ^{27}Al(p, p')^{27}Al study of Benamara *et al.* [Benamara 2014]. The level of non-selectivity of the (p, p') can be appreciated to its true value on Figure 5.17 which presents the levels reported in the work of Benamara *et al.* and those observed in this thesis work. And only when the $\ell = 0$ behaviour is strong enough can distributions be separated between the possible transfers, $\ell = 0$, 1, 2 or mixed 0 & 2. Keeping this is mind, the most stringent cases are 11198, 11285, 11408 and 11464 keV, see Figure 5.18, 11956 and 12512 keV, see Figure 5.19. For each the angular distribution is clearly enough dominated by an $\ell = 0$ behaviour, which is obvious from the sharp drop in cross section as the centre of mass angle increases. Consequently for each of

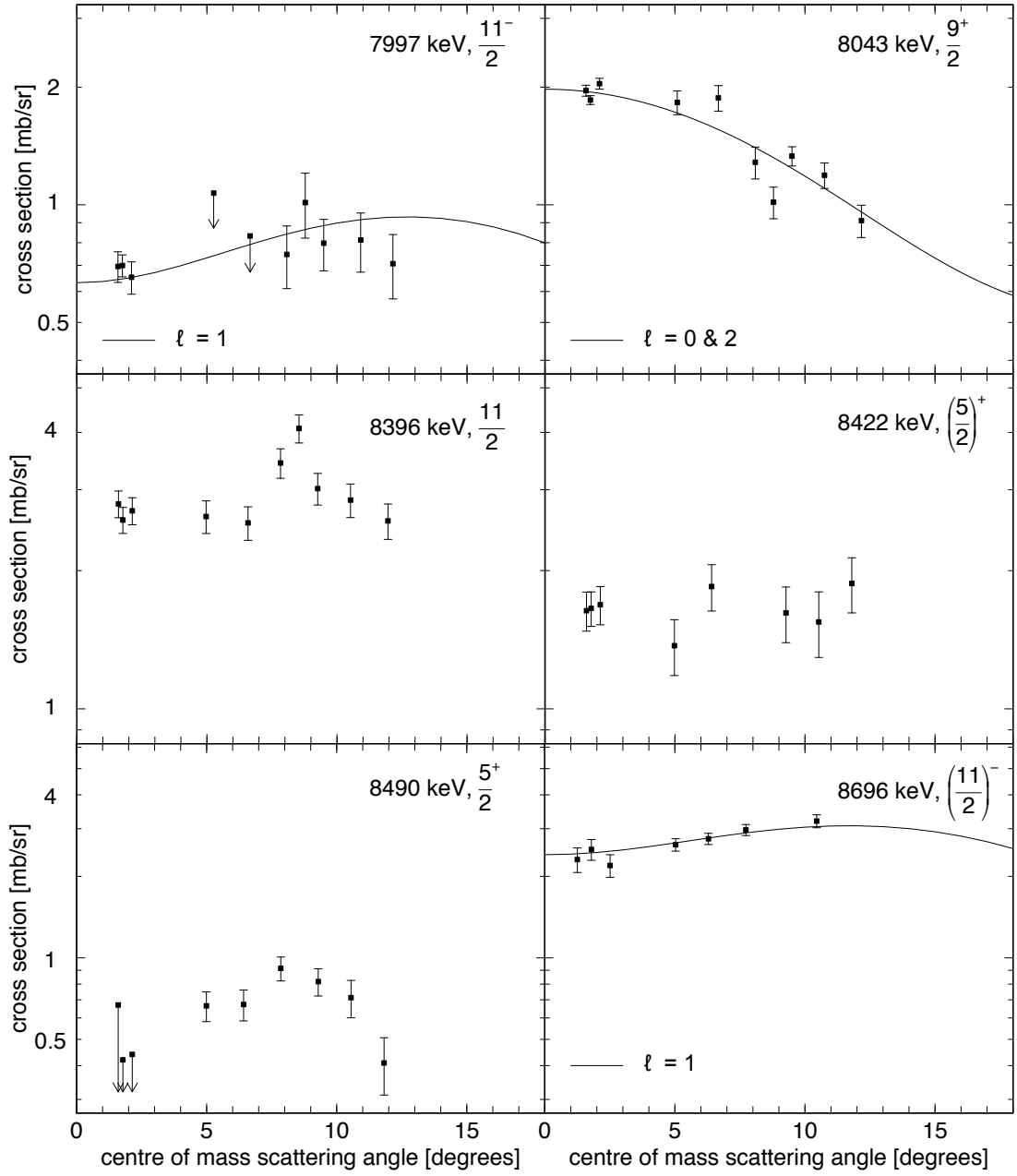

Figure 5.15: Angular distributions of excited states between 7.997 and 8.696 MeV. The spin and parity assignments presented in each figure is based on literature and transfer assignment from this work, and are those used for the TWOFNR calculation that resulted in the solid line in each panel. Note that in the case of poor quality distribution no theoretical cross section is presented.

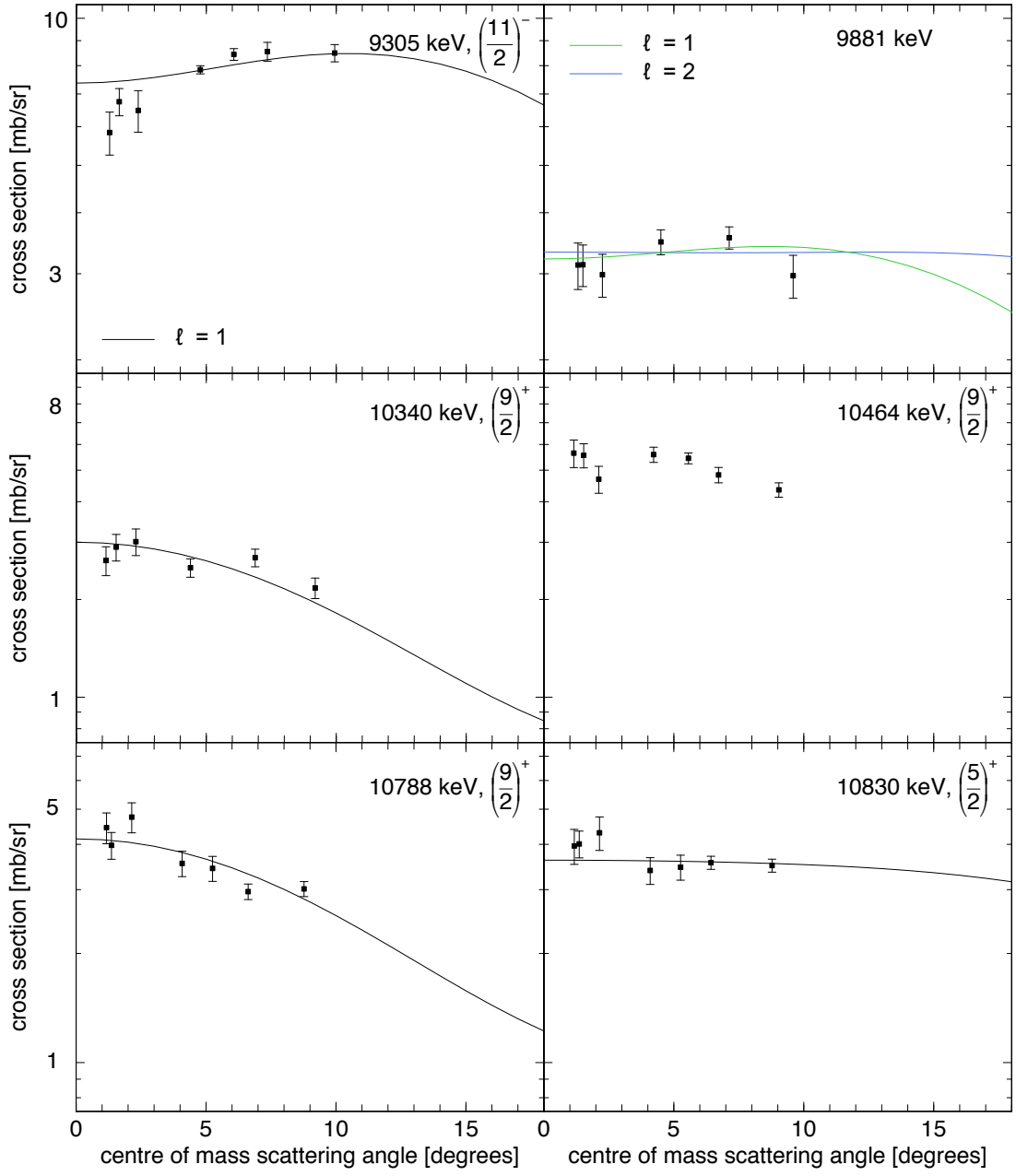

Figure 5.16: Angular distributions of excited states between 9.305 and 10.830 MeV. The spin and parity assignments presented in each figure is based on literature and transfer assignment from this work, and are those used for the `TWOFNR` calculation that resulted in the solid line in each panel. Note that in the case of poor quality distribution no theoretical cross section is presented.

those six states the suggested assignment is $J^{\pi} \in (9/2,\ 11/2)^{+}$ where the parity assignment is firm. All of the states identified within the energy uncertainty of the 11198, 11285, 11408, 11464, 11956 and 12512 keV lines are from the $(p,\ p')$ study where angular distributions cannot be measured. So the spin/parity information provided in this work cannot be strictly assigned to the corresponding states in Table 5.3.

In Figure 5.18, the angular distribution for the 11005 keV line is highly tentative, and the $\ell = 0$ & 2 suggestion has the odds that bookmakers gave to Leicester winning the British Premier League 2015/16 at the start of that season.

The angular distribution for the lines at 11384 and 11592 keV can be fitted by $\ell = 2$ transfers, although $\ell = 1$ would be as convincing, as explained when analysing the 9881 keV distribution.

The three 12036, 12260 and 12512 keV lines have an angular distribution that can be fitted by a mixed $\ell = 0$ & 2. However as shown in Figure 5.20 with the angular distribution of the 12599 keV line, at those energies any of the $\ell = 0$, 1, 2 or 0 & 2 is as good as the other one. Though often the presence of a $\ell = 0$ means that the measured C^2S will be lower, this is because of the factor of around 100 between the cross section for $\ell = 0$ and $\ell = 2$ with C^2S factors of 1 at the same energy. So very little $\ell = 0$ and very little $\ell = 2$ may be required to fit a given line around 12 MeV when too high a $\ell = 1$ C^2S would be implied by such an assignment. This is hand-wavy but should be kept in mind when assessing the suggestion made throughout this section.

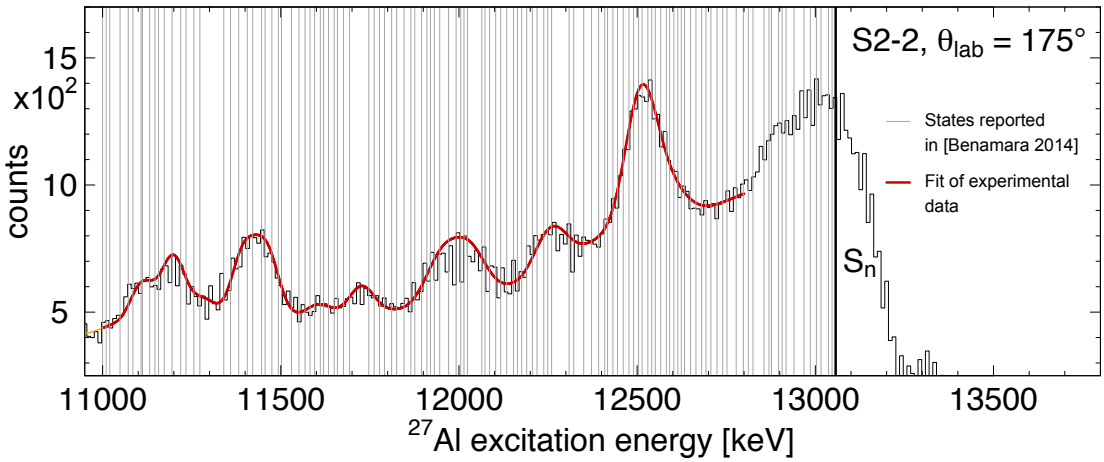

Figure 5.17: Superposition of a spectrum from this work, obtained at $\theta_{\mathrm{lab}} = 175°$ in s2-2 and of the lines observed in Ref. [Benamara 2014] (in light grey). The red line represents a fit to the experimental data.

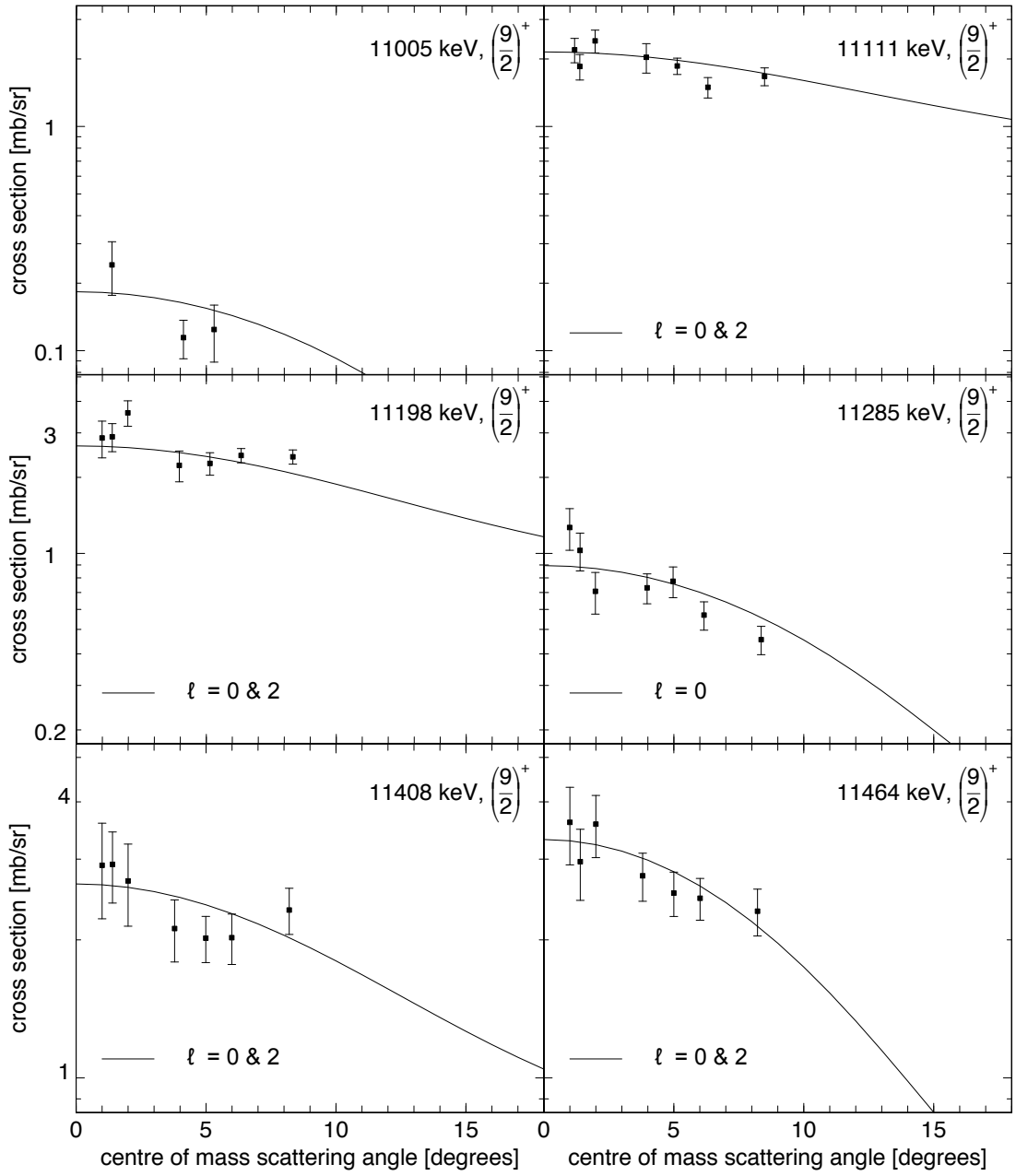

Figure 5.18: Angular distributions of excited states between 11.005 and 11.464 MeV. The spin and parity assignments presented in each figure is based on literature and transfer assignment from this work, and are those used for the TWOFNR calculation that resulted in the solid line in each panel.

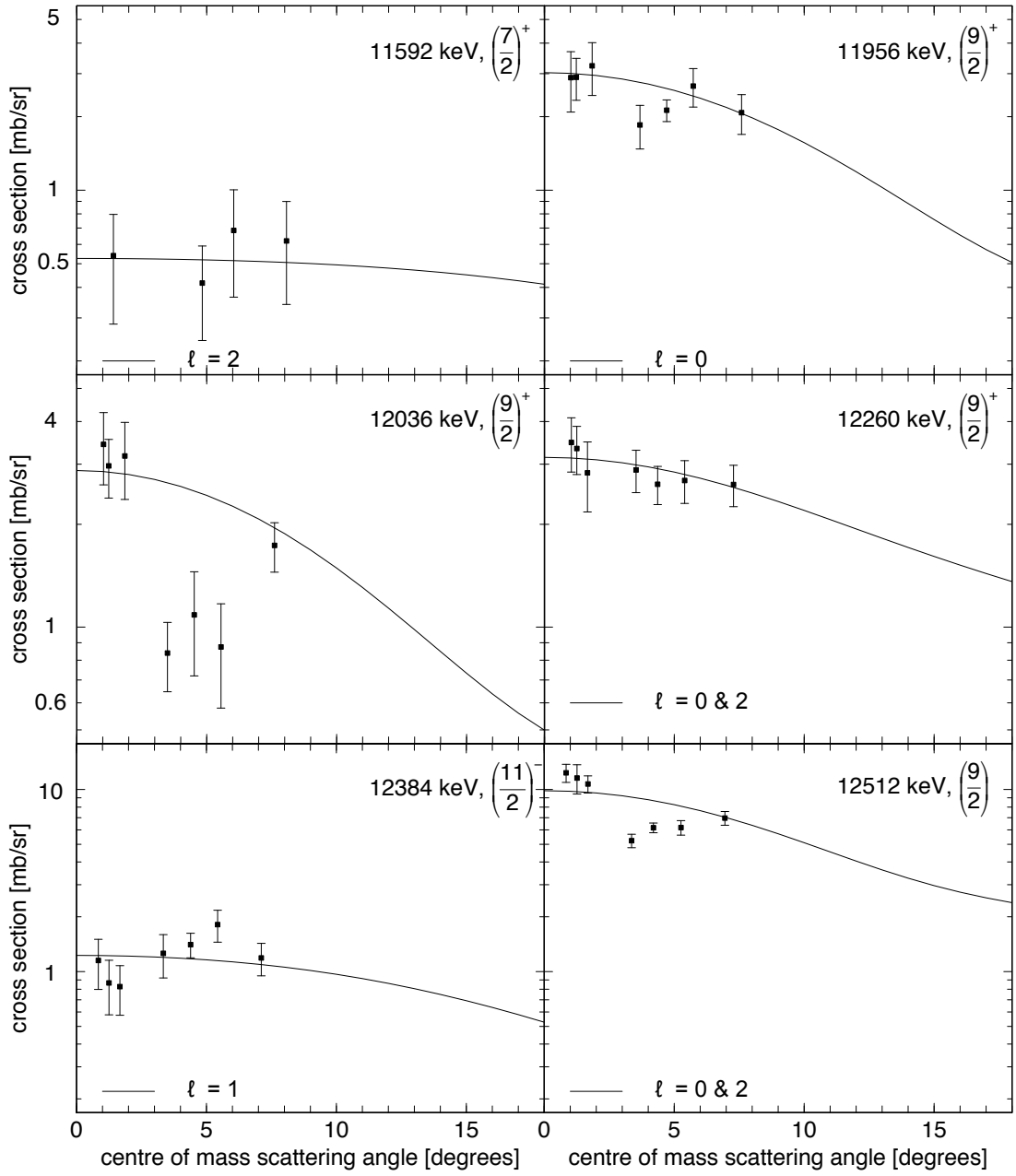

Figure 5.19: Angular distributions of excited states between 11.592 and 12.512 MeV. The spin and parity assignments presented in each figure is based on literature and transfer assignment from this work, and are those used for the TWOFNR calculation that resulted in the solid line in each panel.

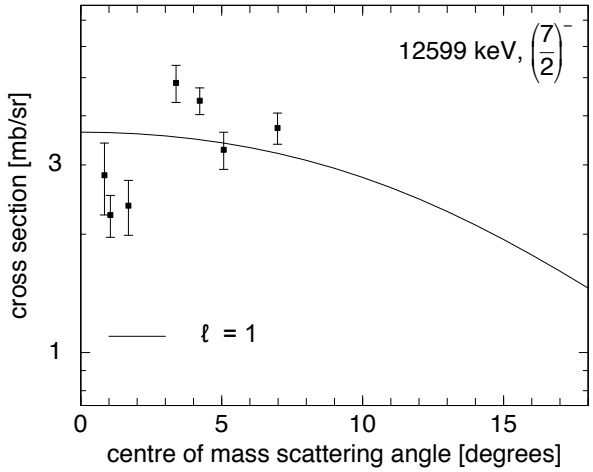

Figure 5.20: Angular distributions of the state at 12.599 MeV. The spin and parity assignment presented in the figure is based on literature and transfer assignment from this work, and are those used for the `TWOFNR` calculation that resulted in the solid line.

Table 5.4: List of experimental spectroscopic factors obtained from fitting the ADWA transfer calculations to the measured angular distributions.

E_{state}	J^π	ℓ	C^2S			χ^2	
			$2s_{1/2}$	$1d_{5/2}$	$2p_{1/2}$	total	/ndf
2212	$7/2^+$	2		0.23		36	1.6
3004	$9/2^+$	0 & 2	0.49	0.18		440	12
4510	$11/2^+$	0 & 2	0.11	0.33		165	4.5
5500		0 & 2	0.37	0.53		229	10
5667		0 & 2	0.053	0.76		59	2.7
6514		0 & 2	0.040	0.23		18	0.9
6948		0 & 2	0.17	0.61		89	4.2
7174		0 & 2	0.022	0.11		13	1.3
7289		2		0.450		76	7.6
7400			0.0083			18	1.8
7664			0.091			64	5.8
7806	$9/2^+$	0 & 2	0.0093	0.068		18	1.8
7948	$11/2^-$	1			0.14	5	0.42
7997		1			0.117	8	0.8
8043			0.0272	0.130		26	2.6
8396							
8422							
8490	$5/2^+$						
8696	$(9/2)^-$	1			0.33	4	0.6
—	$(11/2)^-$	1			0.28	4	0.6
9305	$(9/2)^-$	1			0.79	16	2.3
9305	$(11/2)^-$	1			0.66	16	2.3
9881	$(5/2^+)$	2		0.82		6	1
—	$(9/2^-)$	1			0.27	5	0.8
10340	$(9/2^+)$	0 & 2	0.04	0.08			
10464							
10788	$(9/2^+)$	0 & 2	0.06	0.1			
10830	$(5/2)^+$	2		0.60		5	0.7
11005	$(9/2^+)$	0	0.004				
11111	$(9/2^+)$	0 & 2	0.02	0.1			
11198	$(9/2^+)$	0 & 2	0.03	0.1			
11285	$(9/2^+)$	0	0.019				
11408	$(9/2^+)$	0 & 2	0.04	0.08			
11464	$(9/2^+)$	0 & 2	0.07	0.01			
11592	$(7/2^+)$	2	0.04			1	0.4
11956	$(9/2^+)$	0 & 2	0.09				
12036	$(9/2^+)$	0 & 2	0.09				
12260	$(9/2^+)$	0 & 2	0.06	0.08			
12384	$(11/2^-)$	1			0.05	8	1.1
12512	$(9/2^+)$	0 & 2	0.45	0.004			
12599							

Chapter 6

Experimental results for the ^{44}Ti(α, p)^{47}V reaction

This Chapter presents the results from the measurement of the cross section of the ^{44}Ti(α, p)^{47}V reaction. The associated experiment was performed, as shown before, at the REX-ISOLDE facility at CERN. The detector set up utilises one S2 detector placed at 12.7 cm downstream of a helium gas filled cell. The first sections of this chapter focus on the calibration of the detector and the particle identification before a measurement of the cross section for the reaction can be conducted in the later sections.

6.1 Energy calibration

The principles of energy calibration were explained in Section 5.3. Note that here gain matching was not required.

Energy calibration is made strip by strip within the only S2 detector used. In order to perform such calibration, a quadruple-α source was positioned on the target holder, it contains samples of ^{239}Pu (E_α =5.1566 MeV), ^{241}Am (E_α =5.4856 MeV), ^{244}Cm (E_α =5.8048 MeV) and ^{148}Gd (E_α =3.1827 MeV). The zero offset and the linearity of the ADCs can also be determined with a pulser walk-through, as shown in Figure 6.1, a faked series of energy signal *equally spaced* generated by a BNC PB-4 module plugged in at the input of the preamplifier unit. The amplitude of the pulse generator was set such that a sufficient number of pulses would be observed in each strips, *e.g.* 9 in strip number 10 showed in Figure 6.1. Verifying the effective spacing between each pulse from the output of the ADCs therefore provide an indication of the linearity (are the output pulses *equally spaced*?) and of the zero position (what is the non-locality in channels?).

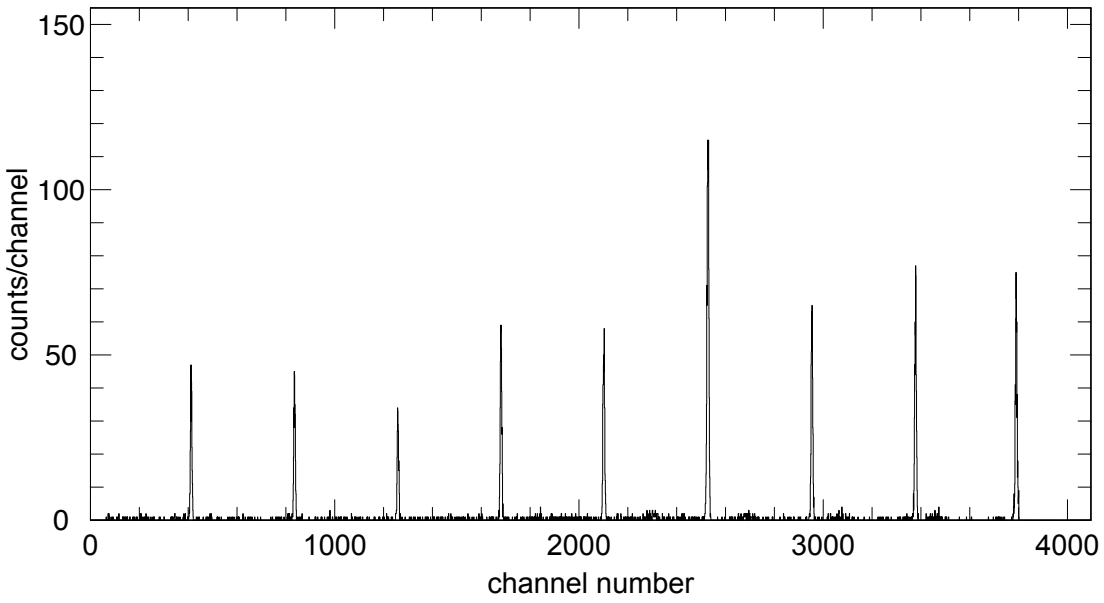

Figure 6.1: Spectrum of the pulser walkthrough for strip number 10.

However, provided that the ADCs behave linearly, the offset is better determined using the quadruple α-source and a full energy calibration.

6.2 Event identification

6.2.1 Event selection

The first step in identifying the observed features on a raw E-ΔE plot is to check that all events are true events resulting from the impingement of ^{44}Ti particles onto the ^{4}He gas, and the hydrogen contained on the window, and a subsequent reaction. Electric noises can generate undesired events which tends to mainly populate the region near 0 in the ΔE and/or E but can also create fake signal elsewhere in the E-ΔE plan, see Figure 6.4. Elimination of those events could be achieved by requiring that events were two folded with specifically one hit in the ΔE side and one in the E side, and that those hits would be geographically localised within a physical geometry. In other words putting a requirement that the dispersion between the two hits respected a physical straggling of protons and α-particles. This is shown in Figure 6.5 and the hit pattern in the E detector for selected hit-sectors and hit-strips in the ΔE detector is shown in Figure 6.6. This has proved to be extremely powerful, with a clean up of the data apparent from comparison of Figures 6.4 & 6.7 very effective yet not destructive of true physical events, as the number of counts in the α locus is unaffected by the process.

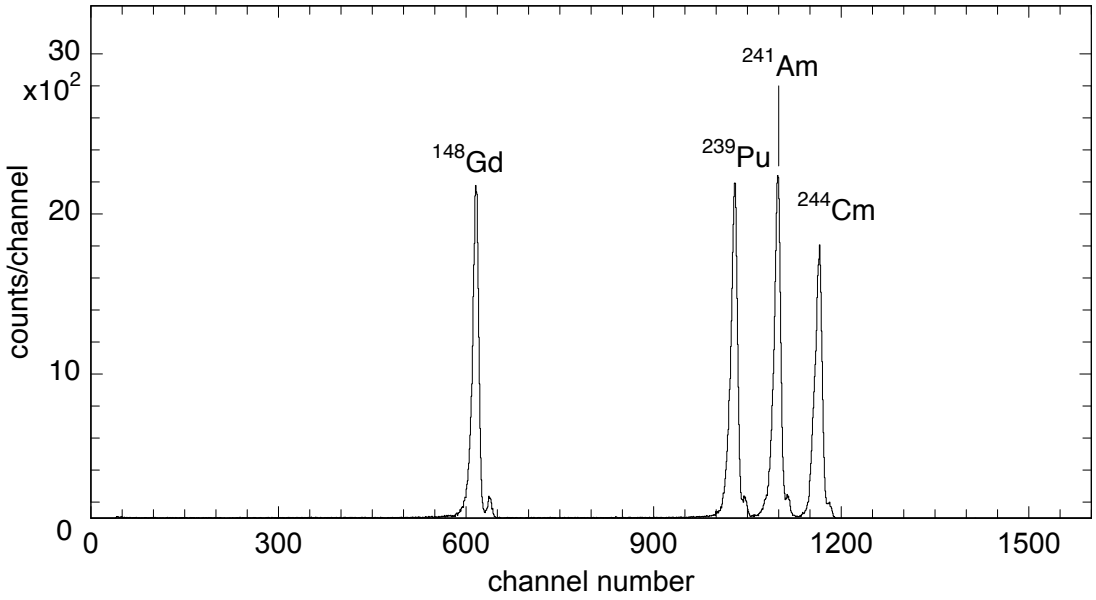

Figure 6.2: Uncalibrated spectrum of the emission lines from the α-decay of ^{239}Pu (E_α =5.1566 MeV), ^{241}Am (E_α =5.4856 MeV), ^{244}Cm (E_α =5.8048 MeV) and ^{148}Gd (E_α =3.1827 MeV).

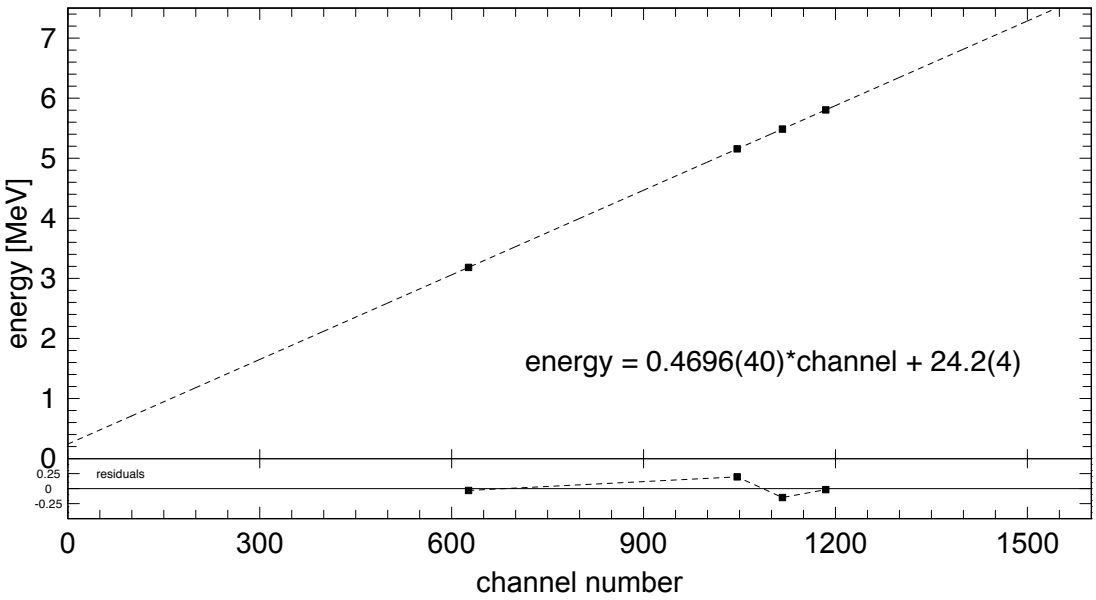

Figure 6.3: Calibration fit for (the front) strip number 10.

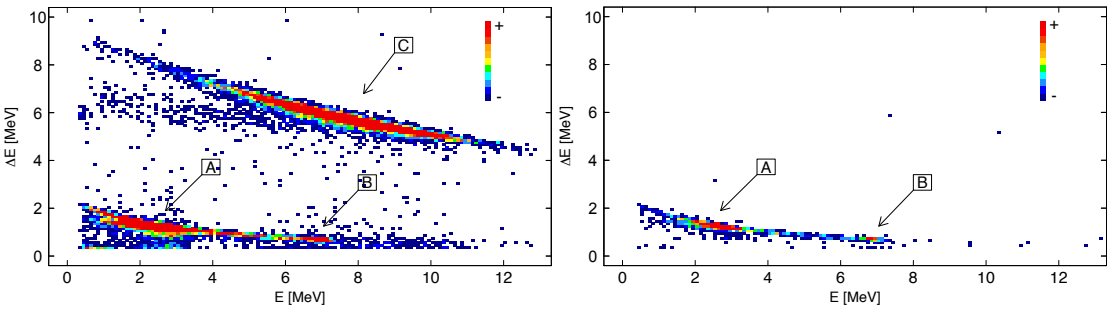

Figure 6.4: Gas-in (left) and gas out (right) E-ΔE plot before multiplicity and E/ΔE coincidence requirements. The A, B and C labels have the same meanings throughout this chapter.

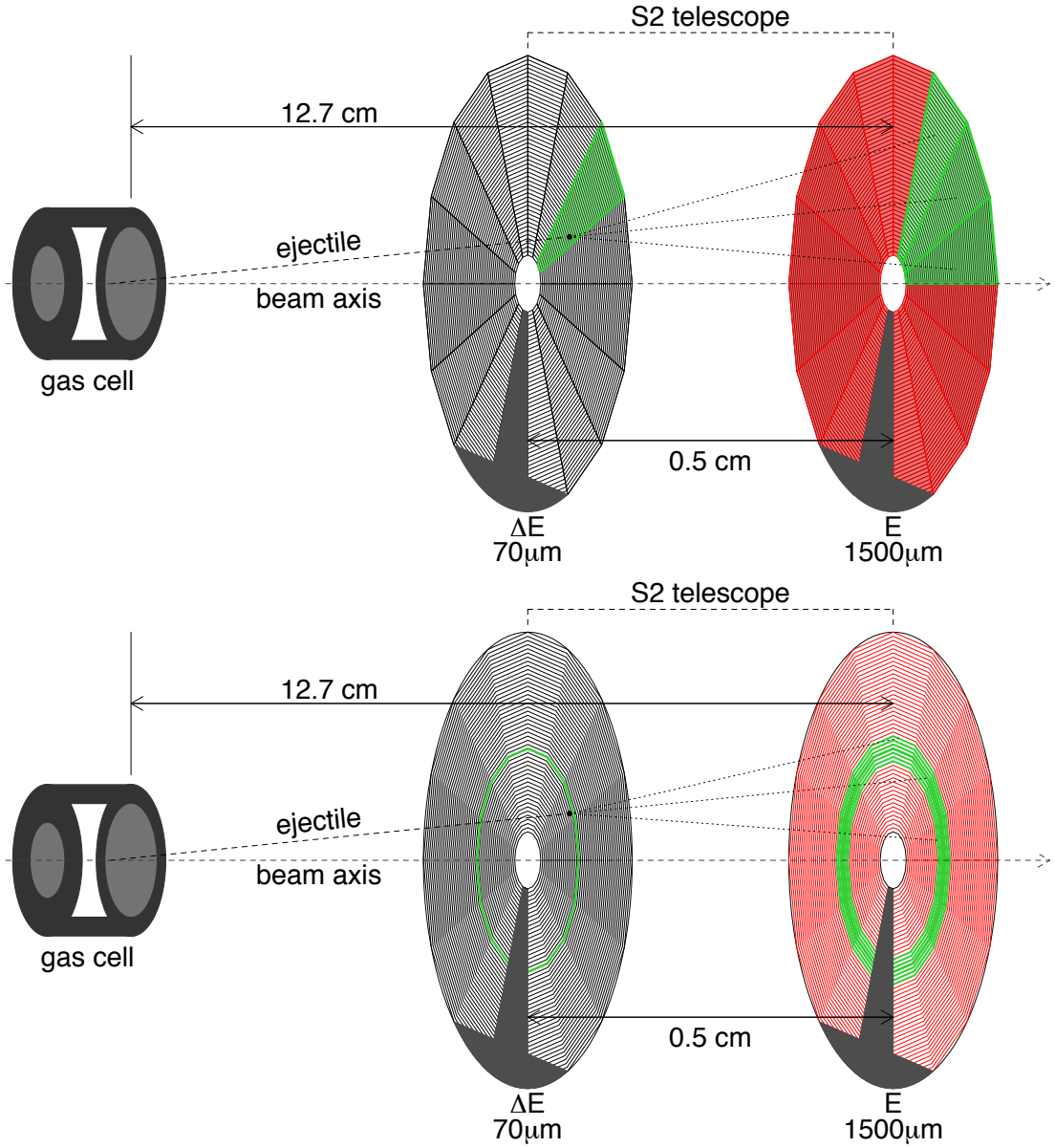

Figure 6.5: Schematic for event selection/rejection based on particle trajectory between the ΔE and E sides of the detector.

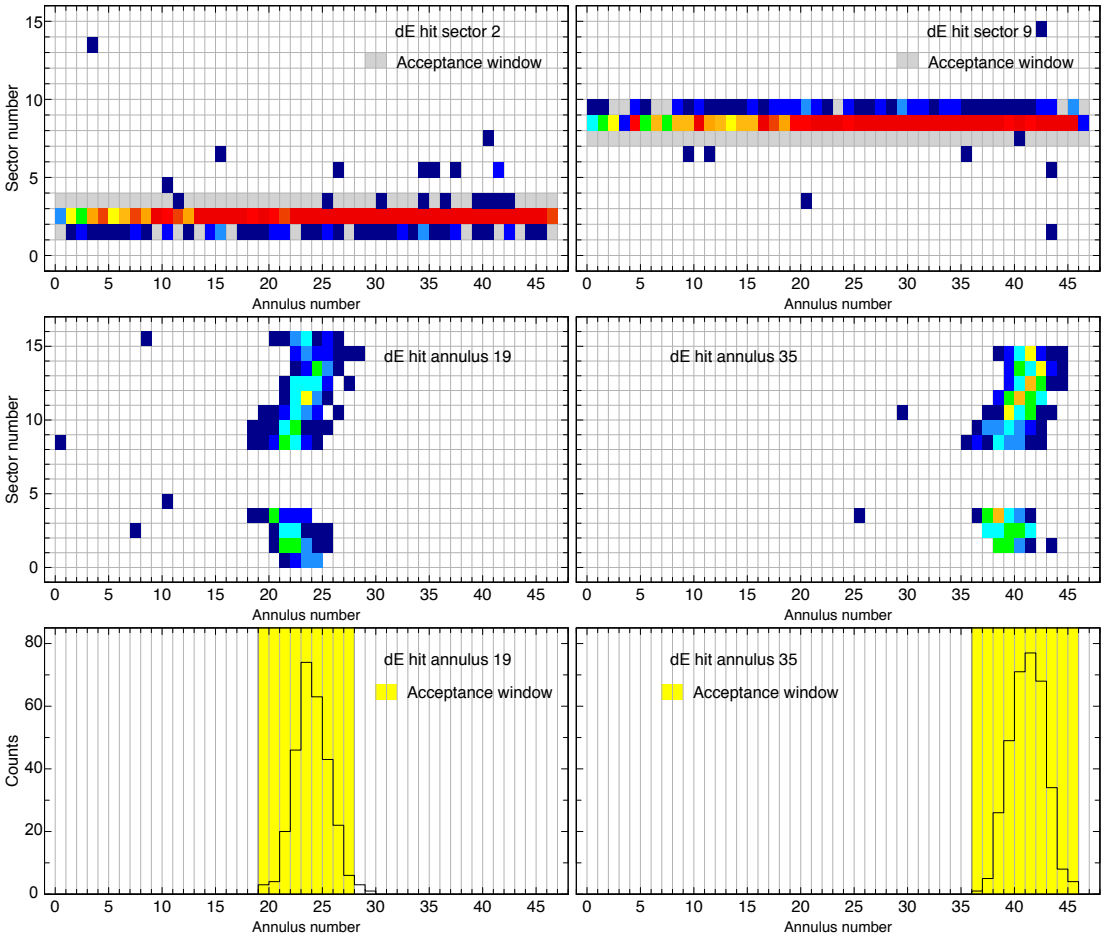

Figure 6.6: Coincident hit patterns in the E detector with selected hits in the ΔE detector. The coincidence conditions extracted from these plots are shown in grey (top) and yellow (bottom). Note that 4 sectors were given no response.

6.3 Assessing the number of ^{44}Ti(α, p)^{47}V events

Since the energy loss of a particle through material is proportional to Z^2 particle identification is relatively straightforward. While only α-particles elastically scattered are to be measured, therefore generating only one α locus, two different reaction types for the protons are expected. One is the elastic scatter of protons from condensation of water and oil on the cell windows (happening on all material within the chamber) while the other is from the sought for (α, p) events.

6.3.1 Gas-in and background data

The experimental results in the E-ΔE plane are presented in Figure 6.7, where elastically scattered α-particles from the gas are labelled A, elastically scattered protons from condensation on the front side of the entrance window of the gas cell are labelled B, and elastically scattered protons from condensation on the in side of the entrance and exit windows of the gas cell are labelled C. The identification of these loci is developed in details in the following sections. The beam intensity ratio between the gas in and the gas out (background) measurements is of importance for subtracting the background from the gas in data. In order to measure this ratio several approaches have been taken. The first is to use the recorded beam intensity from online readings of the Faraday Cup, integrating them assuming a linear behaviour between two readings. Another method consists in using the measurements of the 1157 keV line in the HPGe detector in each recorded runs and inferring a beam intensity from the time dependence of the line's intensity. The γ-rays are produced as ^{44}Sc, itself product of the β-decay of ^{44}Ti, β-decays into the 1157 keV state of ^{44}Ca and eventually to the stable ground state of ^{44}Ca by emitting a γ-ray of the same energy. Finally the ratio between elastically scattered protons from condensation on the sides of the window between runs with a filled gas cell and runs with an empty gas cell can be used. The later solution is only viable if there is the same amount of condensation across all runs, while this is not directly measurable, an indirect assessment can be carried by comparing the results of each solution. This is shown in Figure 6.8. While in appearance the most dangerous solution for beam intensity measurement it was concluded that due to the perfect agreement of all three solution and the better precision obtained, the elastically scattered protons would be the best for determining the ratio gas-in exposition to gas-out exposition. The gas in and gas out proton spectra are shown in Figure 6.9.

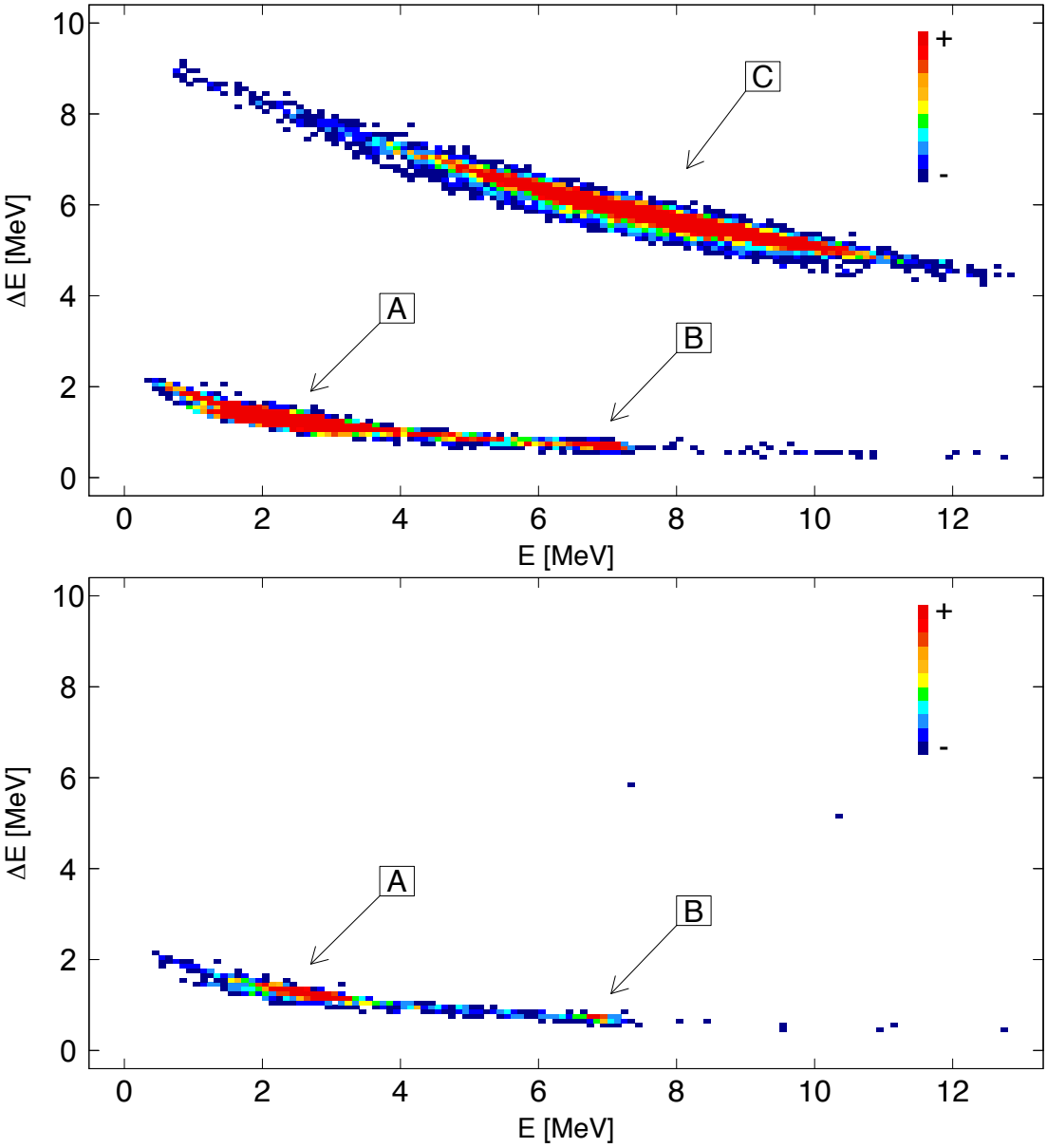

Figure 6.7: Gas in (top), gas out (bottom) data observed by a S2 detector positioned at 12.7 cm downstream from the gas cell, obtained by impinging a nominal 2.10 MeV/u ^{44}Ti beam on a gas cell containing ∼50 mbar of ^{4}He gas. The gas cell is closed by an entrance window made of Aluminium with nominal thickness of 6 μm, the exit window has an Aluminium thickness of 15 μm. The exposition ratio between gas-in and gas-out data is ∼4:1 (see text). Elastically scattered α-particles from the gas are labelled A, elastically scattered protons from condensation on the gas cell are labelled B and C (see text).

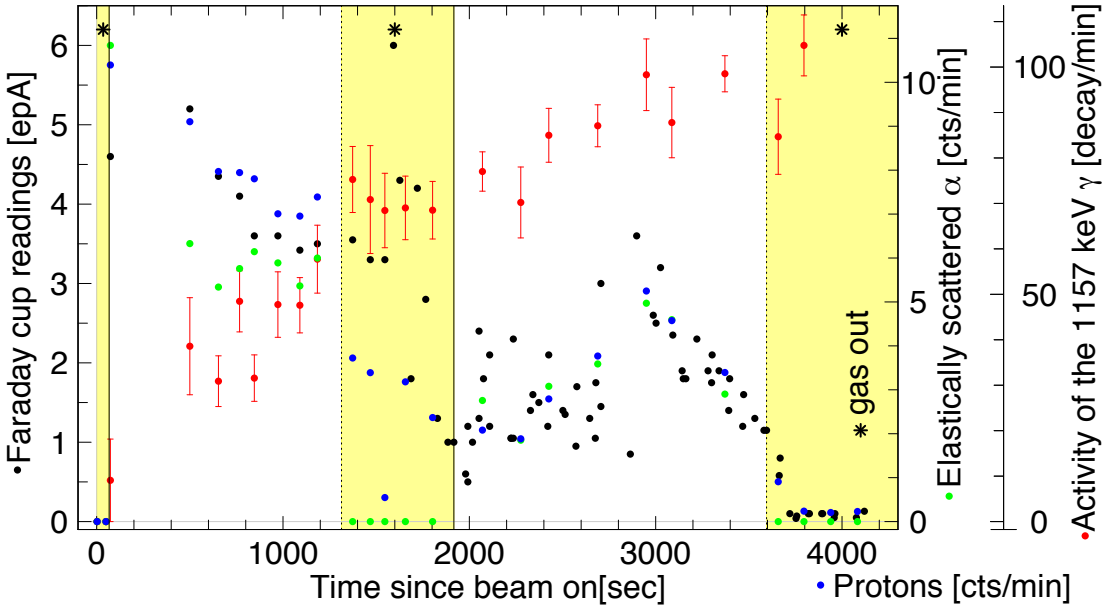

Figure 6.8: (Real-)Time dependence of different experimental features, for the first continuous set of measurements. In black the online readings of the Faraday cup amperage are shown. The other measurements are all off-line and therefore only one data point per run can be presented. The elastically scattered α-particles are plotted in green, the elastically scattered protons (regardless of their origin) are shown in blue with a scale similar to that of the α-particles (not shown for visibility purposes). Finally the activity of the 1157 keV γ-ray as measured by the HPGe detector (and corrected for efficiency) is shown in red.

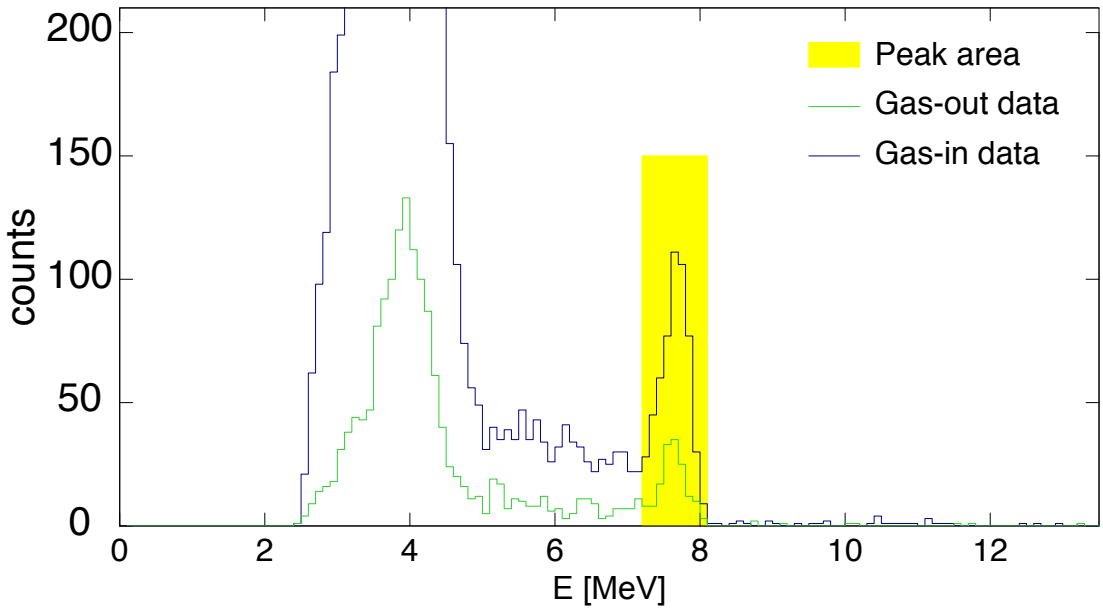

Figure 6.9: Comparison between the gas in and gas out total energy projection zooming on the elastically scattered protons energy region. The yellow area represents the region labelled B in previous figures (elastically scattered protons from the front side of the entrance window). In this region the ratio between the integrated number of counts (554 vs 151) represents the beam exposure difference between the two set of measurements.

6.3.2 Monte-Carlo simulation as an event identification tool

In order to identify the observed features, the Monte-Carlo simulation code of Professor Alex Murphy, used in, for example, Ref. [Salter 2012] was solicited. It incorporates energy losses from the evaluation tables of SRIM [SRIM], energy straggling from the Bohr formula (scaled to experimental calibration data), angular dispersion of the beam determined by the beam focussing geometry, with application of Gaussian smearing to relevant parameters. Scattering was assumed to be isotropic in the centre of mass, detector dead-layers set at 0.8 μm and intrinsic energy resolutions of 15 keV for protons and 25 keV for α-particles assumed. Typical results from this simulation are presented in Figure 6.10, where the parameters used are E_{beam}=1.95 MeV/u, a S2 distance of 12.7 cm and entrance window thickness of 5.75 μm. Considering the energy loss in a material is proportional to Z, the beam energy could first be found by reproducing the high energy peak from elastically scattered protons from the front of the entrance window. As the incoming ^{44}Ti particles have not been slowed through the aluminium, this peak only depends on the beam energy.

Consequently this parameter was set to 2.16 MeV/u, somewhat different from

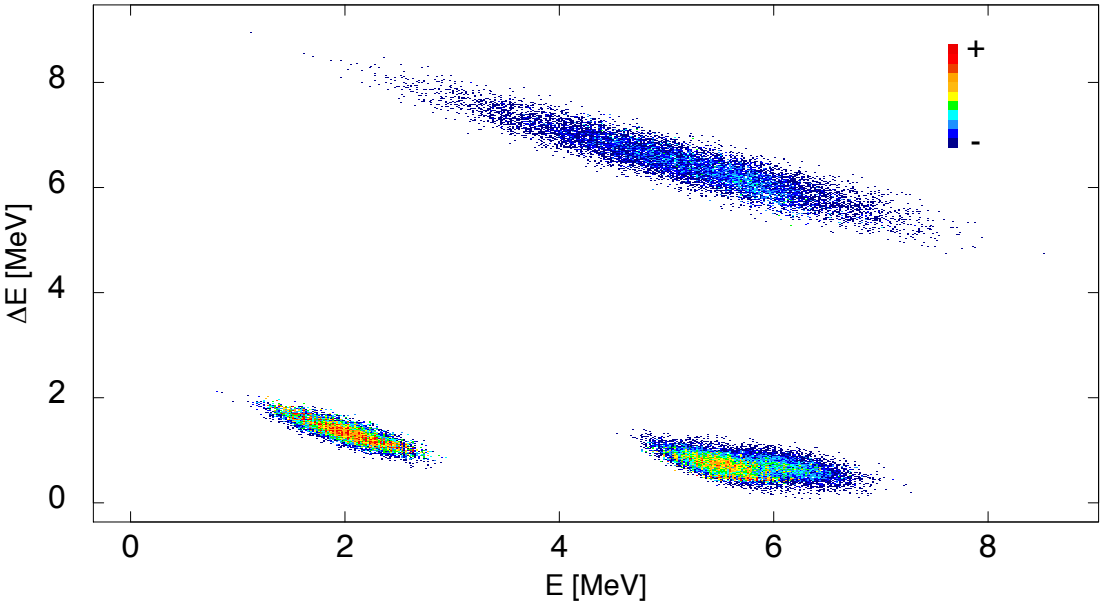

Figure 6.10: Results of a Monte-Carlo simulation of the E-ΔE plot for the ^{44}Ti(α, p)^{47}V reaction. A total number of 10'000 events are simulated. Cross sections are set arbitrarily for plotting purposes. The parameters used are E_{beam}=1.95 MeV/u, a S2 distance of 12.7 cm and entrance window thickness of 5.75 μm.

what the CERN Isolde operators suggested (2.10 MeV/u) but within an acceptable margin. The second parameter, the entrance window thickness, was then varied, with the beam energy fixed to 2.16 MeV/u, until reproduction of the low energy peak, from elastically scattered protons from the inside of the gas cell, *i.e.* back of the entrance window and front of the exit window. The most accurate reproduction of the experimental features was obtained with a thickness of 6.62 μm. Comparison between the simulation output for those parameters and the experimental results are presented in Figure 6.11. As can be seen, the main features, peak centroids and widths are well reproduced, but smaller features are not. In particular a constant background between the two elastically scattered proton peaks. This can be explained by a "filling" of the Aluminium entrance window with water from which protons would be elastically scattered as the beam travel through the window and explaining the constant background. Similarly the low energy tail could be explained by a "filling" of the Aluminium exit window, the difference being that low energy protons would not be able to exit the window and/or to travel through the ΔE side of the S2 telescope (therefore not producing a 2-fold event).

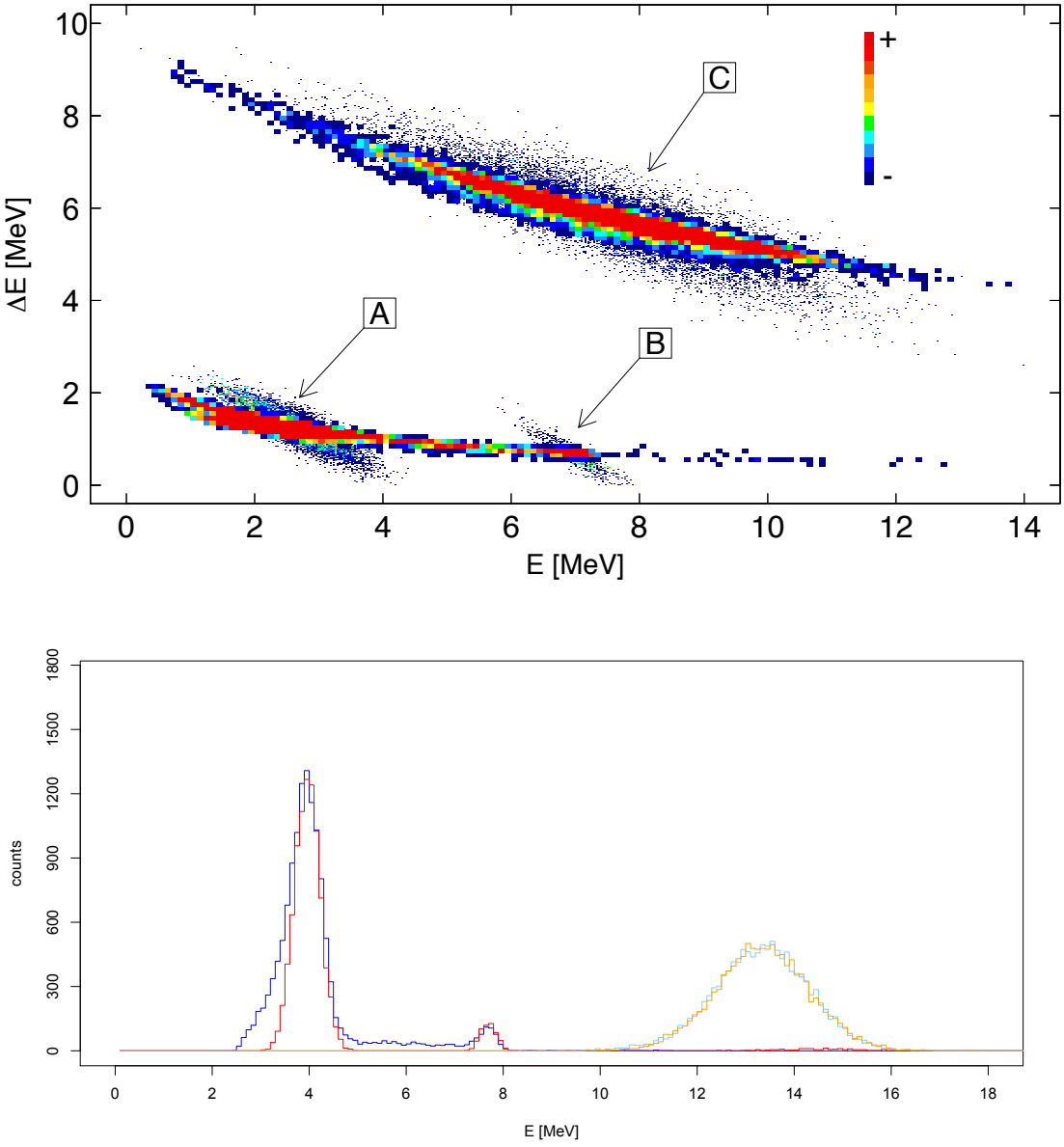

Figure 6.11: 2D (top) comparisons between a Monte-Carlo simulation of the E-ΔE plot for the ^{44}Ti(α, p)^{47}V reaction and the experimental results. The 1D (bottom) comparison is for a projection on the E+ΔE plan in order to separate proton and α events. The parameters used are E_{beam}=2.16 MeV/u, a S2 distance of 12.7 cm and entrance window thickness of 6.62 μm.

6.3.3 Absence of clear ^{44}Ti(α, p)^{47}V events

In Figure 6.12, feature D shows the simulated distribution for events from ^{44}Ti(α, p)^{47}V reactions, under the same parameter set as used to accurately reproduce features A, B and C. Ejectile protons are expected to be detected with a broadly Gaussian distribution of energies centred at E_{lab} = 8.09 MeV with a 1σ width of 0.50 MeV. The corresponding centre of mass energy distribution for the reacting α-particles, within the gas cell, is centred at E_{cm} = 4.15 MeV and has a 1σ width of 0.23 MeV. A fit of the peak resulting from elastic scattering of protons on the outside of the entrance window (feature B) suggests that the protons from this source contribute less than one count to the data above an energy of 8.09 MeV. The region bounded from the peak energy for the ^{44}Ti(α, p)^{47}V reaction to the peak plus the 3σ width energy is taken as a region where ^{44}Ti(α, p)^{47}V reaction events would be expected, while contamination from elastically scattered protons would not be present. In this energy region, the numbers of events in the gas-in (12 counts) to the gas-out (3 counts) data sets is consistent with the numbers of elastically scattered protons seen in the gas-in and gas-out data in feature B (ratio of 3.7(2)), and corresponds to the respective beam exposures for the gas-in and gas-out runs.

6.3.4 Evaluating of the cross section

Rutherford scattering

Use of Feldman-Cousin statistics

Potential ^{44}Ti(α, p)^{47}V events can therefore only be within the background signal uncertainty, and applying the Feldman-Cousins statistical approach [Feldman & Cousins 1998] this represents a maximum of 5.3 counts (8.0 counts), or 10.6 in the whole peak (16), at a 68% (90%) confidence limit. The resulting upper limit on the ^{44}Ti(α, p)^{47}V reaction cross section is 40 μbarn (60 μbarn), see Figure 6.13. The upper limit is shown considering a flat behaviour of the cross section across the energy spanned by the reacting particles (α-particles as shown in Figure 6.13). A single data point would have no physical meaning. The previous measurements by Sonzogni *et al.* are also presented in Figure 6.13 alongside the cross-section energy dependence obtained from the `NON-SMOKER` Hauser-Feshbach statistical model code (used with standard parameters) [Rauscher 1998, Rauscher 2001]. Note that the Sonzogni's results will be developed in the next chapter.

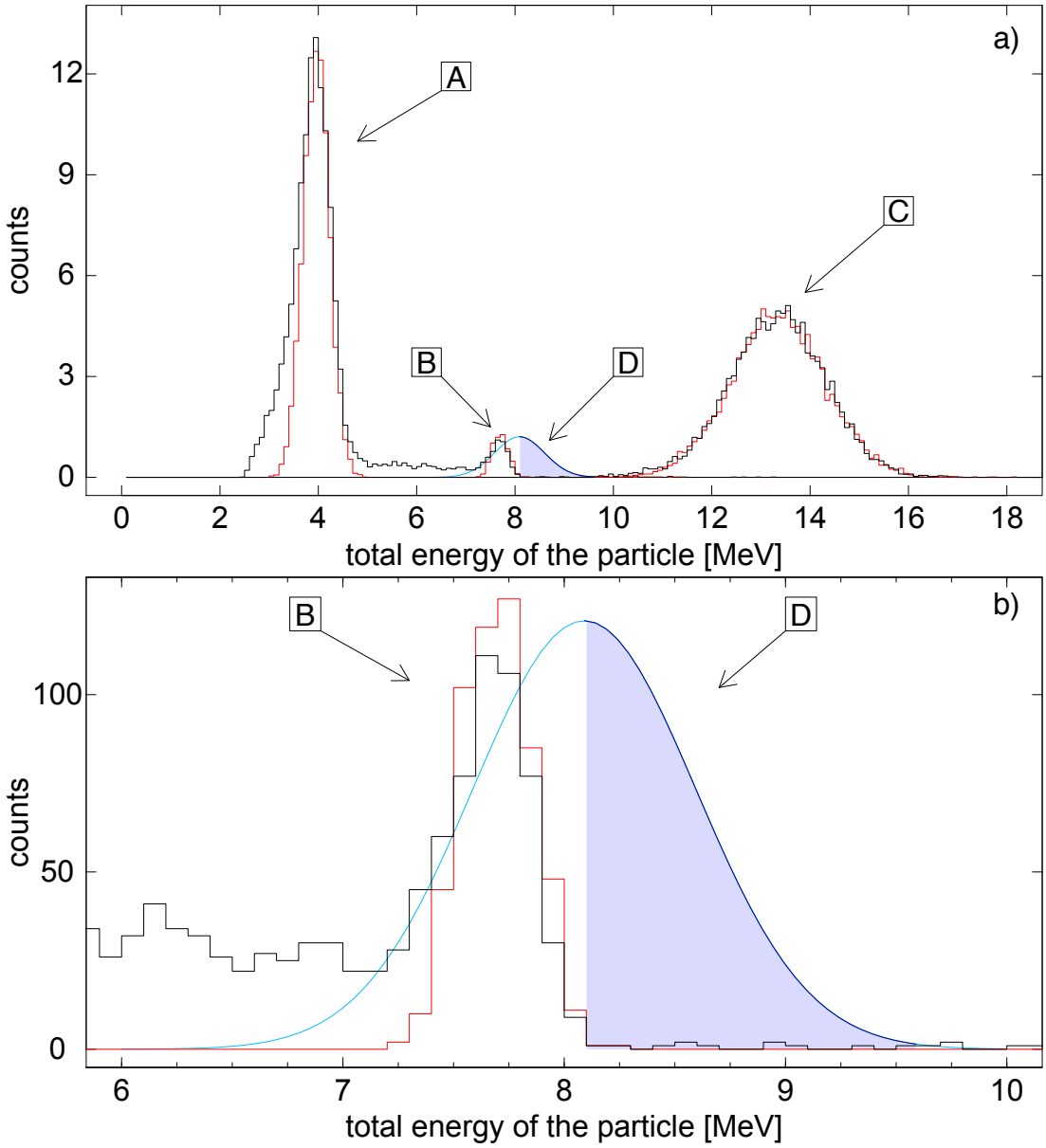

Figure 6.12: Comparison between the total (E+ΔE) energy projection of the experimental data (black) and the results from the simulation using the parameters discussed in the text (red). Figure a) shows the entire energy range; Figure b) zooms on the region where (α, p) events are expected. The blue line represents the simulated (α, p) energy peak and the darker blue line with the shaded blue area represents the region from the centroid position, μ, to μ+3σ.

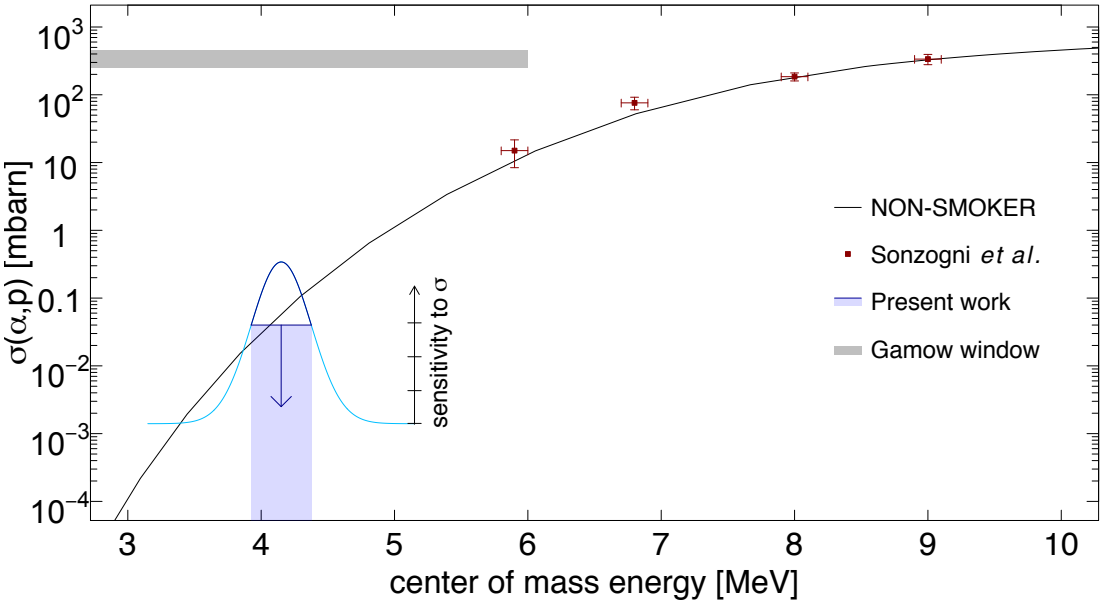

Figure 6.13: Comparison of the measured cross section and the NON-SMOKER prediction, black line, for the ^{44}Ti(α, p)^{47}V reaction. The red points are taken from Sonzogni *et al.* [Sonzogni 2000] while the shaded area represents the constrained region for the cross-section from our measurement. Note that the Gaussian represents the energy spanned by the beam when it passes through the gas cell, see text.

Chapter 7

Discussion

7.1 Implications for the ^{26}Al(d, p)^{27}Al reaction rate

7.1.1 In Asymptotic giant branch and Wolf-Rayet stars

Figure 7.1 shows the contributions of individual resonances to the ^{26g}Al(p, γ)^{27}Si stellar reaction rate, incorporating the results derived in the previous chapter, an average value of 45^{19}_{-16} eV for the strength of the 188.9(6) keV resonance [Vogelaar 1996] and strong resonances at 276.3(4) and 368.5(4) keV in ^{27}Si [Buchmann 1984] (resonance energies are taken from Ref. [Lotay 2011]). It is clear from Figure 7.1 that the 127 keV resonance now dominates the reaction over almost the entire temperature range of WR stars and AGB stars (T $\in$ [0.04, 0.10] GK). Furthermore, by significantly constraining the proton spectroscopic factor for the 127 keV resonance compared to the full range considered in Parikh *et al.* [Parikh 2014], its contribution in novae environments is likely to be negligible.

7.1.2 In Novae

It can be seen from Figure 7.1 that for the region immediately above $\sim$ 0.1 GK, corresponding to the lower temperature range for hydrogen burning in novae, the 189 keV resonance (7652 keV excitation energy in ^{27}Si), is the strongest single contributing state to ^{26}Al destruction. Lotay *et al.* [Lotay 2011] paired this state with a mirror analog level at 7948 keV in ^{27}Al [Basunia 2011], with angular distribution measurements of γ-decays giving a clear $J = 11/2$ assignment for the 7652 keV level in ^{27}Si but with no robust conclusion with regards to the parity of the state. As shown in Section 5.5 from Chapter 5, the present work

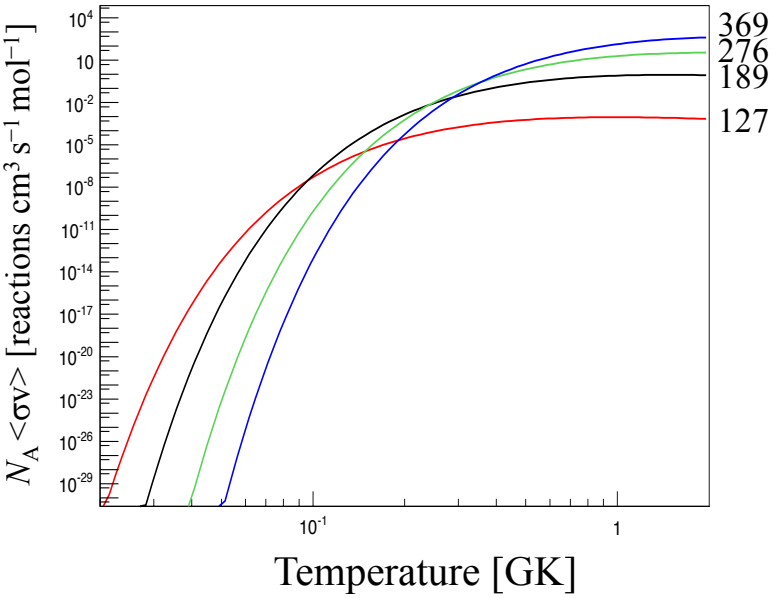

Figure 7.1: Contribution of individual resonances to the ^{26g}Al(p, γ)^{27}Si stellar reaction rate. Resonance energies in keV are given on the right-hand side of the figure. The errors on the energies and strengths of resonances used to derive the reaction rates are given in the text. The contribution of the 68 keV resonance represents an upper limit.

strongly support a $\ell = 1$ assignment for the transfer which indicates a $J^\pi = 11/2^-$ assignment for the the state. The current assignment from the Nuclear Data Sheets is $11/2^+$ [Basunia 2011]. This seems unlikely now. Using the measured C^2S value, 0.14(3), an implied strength for the 189 keV resonance at 52(11) μeV is obtained. This is in excellent agreement with the two direct measurements of 55(9) [Vogelaar 1989] and 35(7) μeV [Ruiz 2006].

7.2 Comparison with recent studies

7.2.1 The competing study of the ^{26}Al(d, p)^{27}Al reaction

An investigation, in inverse kinematics, of the ^{26}Al(d, p)^{27}Al reaction was performed at the Holifield Radioactive Ion Beam Facility (HRIBF) at Oak Ridge National Laboratory which comprises a 25 MV tandem [Pain 2015]. The ^{26}Al beam was accelerated to 117 MeV or 4.5 MeV/u, 75% of the beam energy used for this thesis work (6 MeV/u), and impinged on a 150(14) μg/cm^2 CD_2 target. Silicon detectors were used for measuring the protons and they covered a centre of mass region from ∼6 to ∼55°, and ∼40° for the 7806 keV line. The

spectrum collected at 6.5° is shown in Figure 7.2 taken from Ref. [Pain 2015], the full width at half maximum claimed by Pain *et al.* is 72 keV, against 60 keV in the present study. An insert shows the 7806 keV line which, unlike the spectra presented in Figure 5.9, is not clean. Unfortunately, no fit is presented. The angular distribution reported in Ref. [Pain 2015] is shown in Figure 7.3. Theoretical angular distributions for $\ell = 0$ and $\ell = 2$ obtained by performing an adiabatic wave approximation calculation with the code `FRESCO` [Thompson 1988]. The light particle interactions with ^{26}Al and ^{27}Al were constructed using the Chapel-Hill global optical parametrisation (CH89) [Varner 1991], which is not ideal for the mass region of aluminium as the CH89 potential covers the mass range from $A = 40$ to $A = 209$ and a beam energy region from 10 to 65 MeV/u, as presented in Section 3.4, although it is believed to function well outside these ranges of applicability. (For completeness the neutron potential was built with using a Woods-Saxon shape with parameters $r_0 = 1.25$ fm and $a_0 = 0.65$ fm.) Nevertheless the measured $\ell = 0$ C^{2}S is $10(3)\times10^{-2}$. This is in remarkably good agreement with the results presented in Section 5.5, C^{2}S ($\ell = 0$)= $9.3(19)\times10^{-3}$. An $\ell = 2$ contribution seems very likely from the extra angular coverage compared to the present study, even though it could be from the 7790 keV line (the spin/parity of the corresponding state is $5/2^+$ which would be populated via a pure $\ell = 2$ transfer), a possibility that was not found to be material in the analysis presented in Chapter 5. In any case, the contribution yields a C^{2}S of $2.9(16)\times10^{-2}$. In Section 5.5 this contribution was measured at $6.8(14)\times10^{-2}$. The results disagree but it should be noted that considering the difficulty in measuring the $\ell = 2$ contribution the similar order of magnitude found is already a small success. Consequently the reaction rate found by Pain *et al.* agrees with that presented earlier in this chapter.

7.2.2 The ^{26}Al(d, n)^{27}Si reaction

A recent experiment conducted at Michigan State University by Kankainen *et al.* [Kankainen 2016] aimed at measuring the ^{26}Al(d, n)^{27}Si reaction. The beam at an energy of 30 MeV/u was produced using the in-flight methodology and it was bombarded onto a thick $(CD_2)_n$ target, 10.7(8) mg/cm^2. At the back of the target location, the Gamma-Ray Energy Tracking In-beam Nuclear Array (GRETINA) was positioned to measure the γ-rays coming off the excited states of ^{27}Si populated in the experiment. Collection of data was (principally) triggered by the coincident hit of a γ-ray in GRETINA and of a ^{27}Si recoil in a particle detector (S800 spectrograph [Bazin 2003]). This set up provides a mean for angle integrated cross section to be derived. Here too, the transfer calculations were

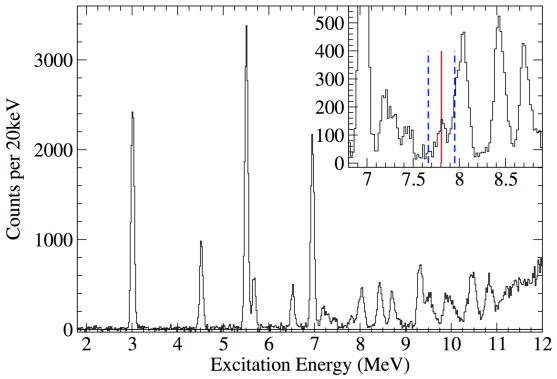

Figure 7.2: Excitation energy spectrum from ^{26}Al(d, p)^{27}Al in the region 2 to 12 MeV, with E_{beam} = 4.5 MeV/u and $\theta_{\text{c.m.}}$ = 6.5°. The inset shows a zoom up on the 7–9 MeV energy range exhibit a peak at 7806 keV, red line. The nearby peaks at 7664 and 7950 keV are indicated by dashed blue lines. The figure is taken from Ref. [Pain 2015].

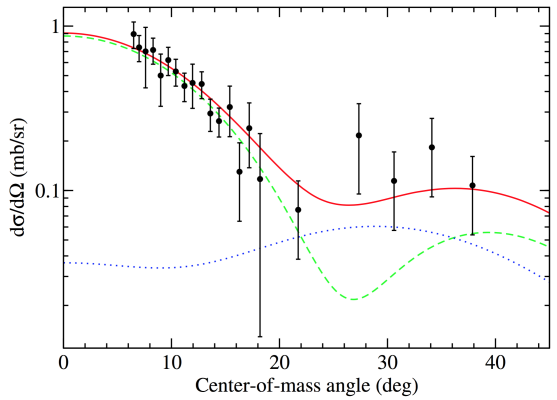

Figure 7.3: Angular distributions and fit of a ADWA calculation for the 7806 keV state in ^{27}Al from Ref. [Pain 2015].

made using FRESCO [Thompson 1988], and the nucleon-^{26}Al potential was also built with the CH89 potential [Varner 1991]. Several C^{2}S were measured for states also investigated in the work presented in this thesis, they are for the resonances at 126.9(9) keV ($E_{\text{exc.}}$ = 7590.1(9) keV), at 188.7(6) keV ($E_{\text{exc.}}$ = 7651.9(6) keV) and at 276.1(4) keV ($E_{\text{exc.}}$ = 7739.3(4) keV). In particular the measurement of the spectroscopic factor of the 188.7(6) keV resonance, 0.22(5), whose mirror state in ^{27}Al is at 7948 keV is in acceptable agreement with the measurement presented in the previous chapter, 0.14(3). This seems to confirm the negative parity of the state.

7.3 Shell model calculation for ^{27}Al

Theoretical spectroscopic factors can be obtained by performing shell model calculations. One of the features of the shell model is to consider that the core of the nucleus made of magic numbers of protons and neutrons is mostly inert. For ^{27}Al the core is ^{16}O, such that the first three orbitals $1s_{1/2}$, $1p_{3/2}$ and $1p_{1/2}$ are primarily ignored. The "active" nucleons are on the $1d_{5/2}$ orbitals, hence the $5/2^+$ ground state of ^{27}Al. The odd proton space, available upon excitation of the valence nucleon, is [$1d_{5/2}$, $2s_{1/2}$, $1d_{3/2}$], known as the *sd*-shell space, which produce positive parity states. When the excitation energy becomes high enough negative parity states can be populated in the *fp*-space, [$1f_{7/2}$, $1p_{3/2}$], or by core excitation with for example the odd protons transitioning from the *sd*-shells to the $1p_{1/2}$ shell. The shell picture for ^{27}Al was presented in Figure 3.9.

Calculations whose results are shown here in Table 7.1 were provided by B. Alex Brown and are further reported in Ref. [Margerin 2016b]. For the *sd*-shell space it utilises the USDA-cdpn and USDB-cdpn Hamiltonians, which are interactions built in a isospin formalism [Bown & Richter 2006] and taking into account the charge-dependent (cd...) and charge-asymmetric nuclear Hamiltonian obtained by Ormand and Brown in a proton-neutron basis (...pn) [Ormand & Brown 1989].

Such calculations are semi-empirical. They heavily hinged upon experimental two-body matrix elements (NNN effects are only considered inherently and when they affect the two-body matrix elements), for example $\langle 1d_{5/2}|2s_{1/2}\rangle_{3^+}$, and single-particle energies, namely $\varepsilon_{1d5/2}$, $\varepsilon_{2s1/2}$ and $\varepsilon_{1d3/2}$. This is similar to the use of semi-empirical shell model calculation near ^{208}Pb, see Refs. [Margerin 2012, Margerin 2016a], that uses the formalism of, for example, Ref. [Lawson 1980]. Here, two "universal" *sd* (USD) Hamiltonians are derived from fitting experimental results, this is explained in details in Ref. [Bown & Richter 2006]. In short, one,

USDA, is highly constrained by requirements in data quality and in the distance from the Hamiltonian results to the data, that further helps convergence of the fit. Theoretical models for the two-body interactions are used when the semi-empirical values may risk the fit to diverge (as per the requirements). The other one, USDB, can be seen as a best fit to most fits. The derivation of USDA highlights a minimum number, N_T, of data to consider to obtain converge. Truncation of the full data, N_d to N_T is done, but the data making up N_T are varied (it is not said if this is $\binom{N_d}{N_T}$, however, seeing as using the values of [Bown & Richter 2006] this number would be $\sim 10^{13}$, it is highly unlikely). The USDB Hamiltonian is therefore determined when a convergence to the all the combinations used to build N_T is obtained. In the *sd* region the rms obtained when fitting existed data with USDA and/or USDB in ∼150 keV [Bown & Richter 2006]. Consideration of charge-dependency and charge-asymmetry leads to a breaking of the isospin quantum number. This is not a "good" quantum number, as highlighted by the mirror energy difference that exists between states of the same isospin T and angular momentum ℓ. These differences were shown in Figure 3.4 from the study of the mirror analogues between ^{27}Al and ^{27}Si by Lotay *et al.* [Lotay 2011]. In considering isobaric (same A) multiplets, an isobaric-mass (difference) multiplet equation can be parametrised. Ensuring these are respected by the shell model Hamiltonians, the model is charge-dependent and charge-asymmetric.

Decomposition of a state on the *sd* basis uses the coefficient of fractional parentages, see Refs. [Lawson 1980, Margerin 2012], which are linked to the C^{2}S coefficients as shown in Chapter 3. Consequently performing shell model calculations of states in ^{27}Al yields the corresponding semi-empirical spectroscopic factors. Typically the closest to 1 a spectroscopic factor is, the better the calculation should perform. Indeed a high C^{2}S means a strong overlap between the (^{26}Al+p) and ^{27}Al systems, and consequently signifies a single-particle driven excitation, which is very well captured by the shell model. Weaker factors should not be so well reproduced because they are synonym of higher modes of excitation, collectiveness, which is not taken into account in the shell model. A comparison of the theoretical and experimental spectroscopic factors is shown in Table 7.1. Considering the relatively small angular coverage of the experimental distribution that does not allow for firm determination of $\ell = 2$ components of mixed $\ell = 0$ & 2 transfers, it is better to compare the $\ell = 0$ C^{2}S for mixed transitions or the single $\ell = 1$ or $\ell = 2$ transfers. It is worth noting that constraining the comparison as just described, and only considering the main states for which it is easier to match experimental and theoretical states, then the shell model results are very consistent with the measurements.

Table 7.1: Comparison between the spectroscopic factors obtained by shell model calculation described in the text and experimental results for selected states.

n	J^π	E_{exc} (MeV)	C^2S $\ell = 0(1)$	C^2S $\ell = 2(3)$
1	$5/2^+$	0.000		1.1
exp.	$\ell = 2$	0.000		3
4	$7/2^+$	2.313		1.0×10^{-1}
exp.	$\ell = 2$	2.212		2.3×10^{-1}
7	$9/2^+$	2.949	5.0×10^{-1}	4.0×10^{-2}
exp.	$\ell = 0$ & 2	3.004	4.9×10^{-1}	1.8×10^{-1}
11	$11/2^+$	4.437	1.3×10^{-1}	2.6×10^{-1}
exp.	$\ell = 0$ & 2	4.510	1.1×10^{-1}	3.3×10^{-1}
17	$11/2^+$	5.382	3.4×10^{-1}	1.3×10^{-1}
exp.	$\ell = 0$ & 2	5.500	3.7×10^{-1}	5.3×10^{-1}
20	$9/2^+$	5.726	9.5×10^{-2}	4.2×10^{-1}
exp.	$\ell = 0$ & 2	5.667	5.3×10^{-2}	6.1×10^{-1}
27	$9/2^+$	6.492	2.2×10^{-2}	3.1×10^{-1}
exp.	$\ell = 0$ & 2	6.514	4.1×10^{-2}	2.3×10^{-1}
39	$11/2^+$	7.118	1.6×10^{-1}	5.0×10^{-1}
exp.	$\ell = 0$ & 2	6.948	1.7×10^{-1}	6.1×10^{-1}
40	$13/2^+$	7.201		1.3×10^{-1}
exp.	$\ell = 2$	7.289		0.45
49	$9/2^+$	7.737	1.1×10^{-2}	1.1×10^{-2}
exp.	$\ell = 0$ & 2	7.806	9.3×10^{-3}	6.8×10^{-2}

7.4 Core collapse supernovae and ^{44}Ti

The upper limit cross section presented in the preceding chapter helps to detach CCSNe calculation from statistical models. However, covering only a small region of the Gamow window, furthermore with an upper limit, is clearly not sufficient for definitive statements and a full calculation of the ^{44}Ti ejecta content still require statistical models. There is nonetheless several factors to learn.

The first observation is that the upper limit is lower than the mean statistical

model prediction, which a 4σ assertion, see Table 7.2. Yet an evaluation of the reaction rates implied by the previous data and by the statistical model [Hoffman 2010] concluded that a factor of three uncertainty remained, and that additional data at lower energy were needed. The new upper limit, at significant lower energy, is presented as the horizontal bar in Figure 6.13 (this was explained in the previous chapter). Folding the distribution of ion energies and an energy dependent cross section provided by the `NON-SMOKER` calculation, the predicted cross section would have been 88 μbarn. Therefore the present result indicates a cross section smaller by, at a 68% (90%) confidence level, at least a factor of 2.2 (1.3) compared to the `NON-SMOKER` expectation, see Table 7.2, considering our reaction distribution, incidentally near the lower limit for `NON-SMOKER`. (At a 99% confidence level, the measured upper limit, 85 μbarn, is still below the `NON-SMOKER` prediction.)

7.4.1 Implications for CCSNe

The dependency of the final ^{44}Ti abundance produced in core collapse supernovae was studied in detail by The *et al.* [The 1998]. The study showed that lowering the ^{44}Ti(α, p)^{47}V reaction rate by a factor of 10 lead to a doubling of the ^{44}Ti abundance in the ejecta. Under the assumption that the present upper limit implies a minimum reduction in the cross section at all energies (within the Gamow window), then the consequent increase in the amount of ^{44}Ti ejected is $\gtrsim$30%, i.e., for the highest model predictions, $\gtrsim$1.3 M$_\odot$. This rate increase would bring the observation of ^{44}Ti produced in SN1987A, 1.5(3) $\times10^{-4}$ M$_\odot$ [Boggs 2015], and Cassiopeia A, 1.25$\pm$0.3 $\times10^{-4}$ M$_\odot$ [Grefenstette 2014], into closer agreement with the amount predicted by core collapse supernovae models.

Perego *et al.* [Perego 2015] have recently used the new upper limit of this work into a CCSNe model (PUSH). This is still a semi-empirical approach as parameters have to be fit to several observables from SN1987A (crucially not the ^{44}Ti yield). The ^{44}Ti ejecta yield derived is 1.49×10^{-5} M$_\odot$ (or 5.65×10^{-5} M$_\odot$ ignoring the quantity that would fall back into the newly formed proto-neutron star). The PUSH method allows the authors to consider mixing and convective overturn of material, whereby material destined to be ejected into interstellar medium or trapped into the PN star might have a different outcome due to the enormous convective forces in play. In doing so, Perego *et al.* concludes that *"the amount of 44Ti in the ejecta is 3.99$\times10^{-5}$ M$_\odot$"*.

Finally it is also worth noting that, by applying this factor to the highest model prediction for the CCSNe ^{44}Ti yield, the age of the recently discovered Vela SNR may rather be $\gtrsim$800 years.

Table 7.2: Impact of the measured upper limit for the cross section of the ^{44}Ti(α, p)^{47}V reactions depending on the confidence level.

Confidence level	Upper limit for the cross section (μbarn)	Reduction factor in σ from NON-SMOKER	CCSNe ejecta ^{44}Ti content[a]
68%	39.6	2.22	1.30
90%	59.9	1.47	1.15
95%	69.9	1.26	1.09
99%	84.5	1.04	1.04

[a] Based on the maximal amount in ejecta from standard calculations at 1 $M_{\odot}$.

7.4.2 Measuring (α, p) reactions on heavy ions

Previous measurement of the ^{44}Ti(α, p)^{47}V reaction

A previous measurement, which was also the first of the ^{44}Ti(α, p)^{47}V reaction, was conducted at Argonne by Sonzogni *et al.* [Sonzogni 2000]. This measurement was made in two parts. The first consisted in forming ^{44}Ti on a scandium disc via the ^{45}Sc(p, $2n$)^{44}Ti reaction. The material was left to irradiate away for long enough, two weeks, until it could be manipulated and the ^{44}Ti separated and adjoin to a $^{\text{nat}}TiO_2$ solution. This is indeed similar to the extraction of ^{44}Ti from the PSI beam dumps as presented in Chapter 4. However, while there was no traces of contaminants in the extraction performed at PSI, the target derived from chemical separation contained other species, in particular ^{44}Ca. (The (α, n) reaction on ^{44}Ca produces ^{47}Ti, while the (α, n) reaction produces ^{47}Ti.) In a second part, the ^{44}Ti ions were accelerated to 133.5 MeV and impinged on a gas cell filled with helium-4 (or not for background measurement). The time of flight of particles trough Argonne's fragment mass analyser was measured to separate the mass 44 species (in particular the beam) from the $A = 47$ species, containing ^{47}V. Upon careful subtraction of the other mass 47 contaminants from the results, the yield of the ^{44}Ti(α, p)^{47}V reaction could be obtained at 5.7, 6.8, 9.0 and 9.0 MeV in the centre of mass. The corresponding results were shown on Figure 6.13, in Chapter 6.

Systematics of HI(α, p)

In order to compare different heavy-ion+α reactions, P. Mohr *et al.* [Mohr 2014] have used a re-scaling of the energy and cross section of a reaction [Gomes 2005]:

$$E_{\text{red.}} = \frac{(A_P^{1/3} + A_T^{1/3})E_{\text{c.m.}}}{Z_P.Z_T}, \text{ and}$$
$$\sigma_{\text{red.}} = \frac{\sigma_{\text{r}}}{(A_P^{1/3} + A_T^{1/3})^2},$$

where P denotes the projectile and T the target, A and Z are the usual mass and proton numbers of the nucleus. In Figure 7.5[1] many heavy-ion+α reactions are plotted showing that they mostly fall on the same pattern apart from four outliers. Although ^{44}Ti(α, p)^{47}V does not exactly fall on the systematics trend, it can be seen on both Figure 7.5 and Figure 6.13, that the reaction does seem to behave as expected from a statistical model such as `NON-SMOKER` (note Ref. [Mohr 2015] uses a slightly different statistical model). It reinforces the conclusion made in the previous section further showing that if the cross section is to behave near the statistical model predictions, then the upper limit must be close to the actual data point. Also if one extrapolates the Sonzogni *et al.* data, showed in various figures, it seems to overshoot the calculation. It could be due to the presence of more contaminant than measured for in the last mentioned experimental work. This could warrant a short re-run of the reaction cross section measurement at the lowest energies investigated by Sonzogni *et al.* [Sonzogni 2000] for which the cross section is still in the tens of millibarn.

[1] This figure is courtesy of P. Mohr

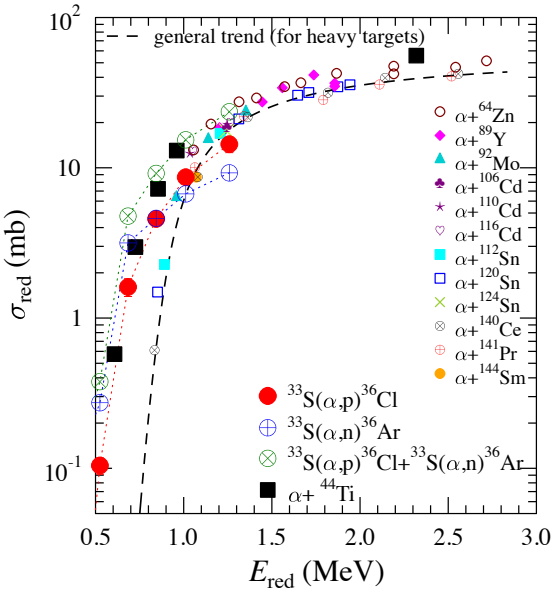

Figure 7.4: courtesy of P. Mohr, a similar figure can be found in Ref. [Mohr 2014].

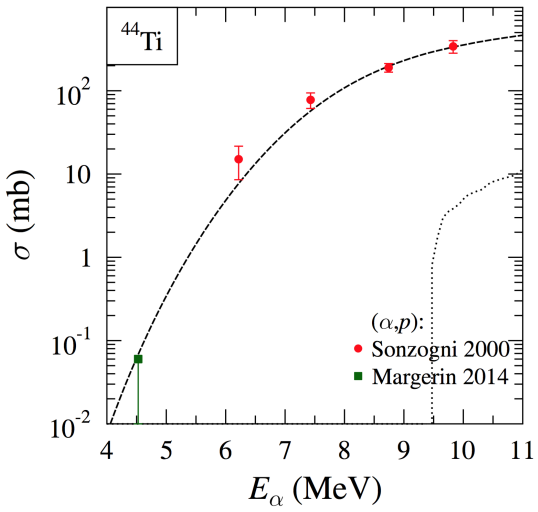

Figure 7.5: From [Mohr 2015].

Chapter 8

Conclusive comments

In conclusion, the work of this thesis has already had a clear impact on the field of nuclear astrophysics. The ^{44}Ti and ^{26}Al nuclei are some of the few astrophysics observables whose provenance and production mechanisms still ask for complete understanding. Here two reactions commanding the reaction rate behaviour have been tackled using new and state-of-the-art methods.

Regarding the ^{26}Al(p, γ)^{27}Si, the mirror study is now complete, although scientific completeness may only be achieved with a direct study and this will be discussed below.

The first study of the ^{44}Ti(α, p)^{47}V reaction at energies of interest for core collapse supernovae was presented in length. Achievement of this pioneering measurement was made through the development of a novel beam production technique. At PSI, Switzerland, the ERAWAST initiative made a TiF sample containing ^{44}Ti in sufficient quantity that it could be accelerated (at the low energies available) at ISOLDE. This allowed a study at a centre of mass energy of 4.15 MeV, below the lowest energy of the previous study and, for the first time, well within the relevant Gamow window. A detailed analysis found no evidence for the presence of ^{44}Ti(α, p)^{47}V reactions in the data, leading to an upper limit of 40 μbarn, at a 68 % confidence limit. This is about half the `NON SMOKER` prediction, and constitutes a step towards explaining the ^{44}Ti excesses already observed in CCSNe. Future experimental studies utilising this and other isotopes reclaimed from accelerator waste have been developed and accepted, they are awaiting scheduling at ISOLDE, with improved beam intensities expected.

8.1 Closing the ^{26}Al(p, γ)^{27}Si reaction study

In recent years, several pieces of work have tackled the issues of the ^{26}Al(p, γ)^{27}Si reaction, which is a pivotal reaction in the production rate of ^{26}Al in most stars. Due to the low cross-sections the direct measurement of proton spectroscopic factors has to be done with the (^{3}He, d) reaction. It has proven to be a very complicated experimental effort, and the study of Vogelaar *et al.* [Vogelaar 1996], which investigated this reaction, has not resolved all the questions. Consequently indirect measurements have been attended, all by the way of inverse kinematics reactions.

In this thesis, a high-resolution study of the ^{26}Al(d, p)^{27}Al transfer reaction in inverse kinematics was indeed presented. It was performed using the most intense radioactive ^{26}Al available in the world, delivered by the ISAC-II facility at TRIUMF, allied with state-of-the-art detection apparatus, the TUDA array. A comprehensive study of many states, principally populated via $\ell = 0$, $\ell = 2$ and $\ell = 0$ & 2, was conducted. It allowed to place experimental constraints on the proton spectroscopic factor C2S of the key 127 keV resonance in the ^{26g}Al(p, γ)^{27}Si reaction. This has resulted in stringent restrictions on the rate at which this reaction occurs and clearly points to the dominant role of the 127 keV resonance in the destruction of the cosmic γ-ray emitting isotope ^{26}Al in Wolf-Rayet and AGB stars. This result was reported in Ref. [Margerin 2015]. A competitive and completely independent study by Pain *et al.* [Pain 2015], came with the same results (see Table 8.1), although with less precise measurements due to a lower beam intensity and broader full width at half maximum for the observed peaks in the proton spectra.

Also from the analysis of Chapter **??** it was shown that the spin/parity of the 7948 keV state in ^{27}Al which Lotay *et al.* have assigned as the analogue state to the 189 keV resonance (E_{exc} = 7652 keV) of the ^{26}Al(p, γ)^{27}Si may rather be $J^\pi = 11/2^-$ instead of the positive parity previously assigned. A (d, n) study conducted by Kankainen *et al.* at NSCL at Michigan State University [Kankainen 2016] could also study the 189 keV state. This resulted in similar conclusions to those present in this work, at the very least in agreements once uncertainties are considered (see Table 8.1).

Although, those studies do not preclude the need to perform a direct measurement via the ^{26}Al(^{3}He, d)^{27}Si reaction, the coherent picture provided by all the very recent results brings the question of the destruction of the cosmic γ-ray emitting isotope ^{26}Al in Wolf-Rayet and AGB stars, and to a lesser extent in Novae, closer to a definite solution.

Table 8.1: Comparison between recent works on the destruction of ^{26}Al in stars.

E_{exc} (keV)	E_{res} (keV)	J^π	ℓ	C^{2}S (d, p)[a]	C^{2}S (d, p)[b]	C^{2}S (d, n)[c]
7806	127	$9/2^+$	0	$9.3(19)\times10^{-3}$	$10(3)\times10^{-2}$	
			2	$6.8(14)\times10^{-2}$	$2.9(16)\times10^{-2}$	
7948	189	$11/2^-$	1	0.14(3)		0.22(5)

[a] From this work and Ref. [Margerin 2015].
[b] From Ref. [Pain 2015].
[c] From Ref. [Kankainen 2016].

8.2 Further exploration of the ^{44}Ti(α, p)^{47}V cross section

Measuring the ^{44}Ti(α, p)^{47}V cross section could ideally be done by obtaining a ^{44}Ti target and impinging an α-particle beam on it. However production of a solid target continues to prove unsuccessful due to still insurmountable chemical obstacles. Measurement of the recoil would be an option. For example in the work of this thesis all ^{47}V recoils produced by the reaction would be collected on the exit window. Extracting and post accelerating them to perform an Accelerator Mass Spectrometry (AMS) analysis could yield an extremely precise count of the number of recoils generated, for an example of how precise such measurements can be, see Ref. [Wallner 2015]. But ^{47}V decays to ^{47}Ti with a lifetime τ = 47 min. Effectively all the ^{47}V recoils would be ^{47}Ti nuclei by the time extraction takes place. Unfortunately ^{47}Ti is naturally occurring, and with the handling of the window and the chemical procedure to extract the radioisotopes from the aluminium foil, it is almost certain that enough ^{47}Ti would be added to the sample to make the measurement statistically insignificant (remembering that the reaction would only produce up to 1000 ^{47}V nuclei depending on the beam intensity). And this is not mentioning the very plausible presence of ^{47}Ti nuclei in the aluminium window. This means that, currently, the only possible way forward is enhancing the set up used in this work.

Consequently, in order to provide measurement of the ^{44}Ti(α, p)^{47}V at different energies, several changes in light of the successes and downsides of the experiment presented in the previous sections have been developed. While the detection technique is not to be profoundly modified, apart from the likely addition of a second S2-telescope, a new gas cell entrance window using thin (2–4 μm)

Mylar foil will be used. It is expected that elastically scattered protons from the scattering centres of the Mylar molecule (a $C_xH_yO_z$ composite), and the oil/water condensation on the window will generate, considering a 60 MeV beam, a 5 kHz count rate, below the detectors limit of 10 kHz. Due to the $1/E^2$ dependance of the Rutherford cross section, a higher beam energy will only lower this background rate. The exit window would not be changed (a 15 μm thick aluminium foil) as this effectively stops the recoil and only generates background counts from water/oil condensation on the inner side of the window.

Previous work from the Edinburgh group has used thin Mylar foils with 300 mBar pressure which is ∼5 times higher than was used in the first phase of IS543, the code name of the experiment at REX-ISOLDE. Our preliminary tests indicate that the gas cell with its new entrance window can handle this pressure and it is anticipated that the forthcoming gas-in data will be taken with 150-200 mBar of ^{4}He. For the experiment, a 30 MBq sample of ^{44}Ti, similar to what provided for the first experiment, will be available but it is thought that little of the source material was successfully extracted and delivered to the gas cell. With better efficiency, a significantly stronger beam intensity is expected.

The use of Mylar foils leads to a lower energy beam being required to deliver the the same reaction energy, as compared to aluminium foils. The reaction energy dependency to the beam energy and the foil thickness is shown in Figure 8.1. This is due to different energy loss in the respective materials. Aluminium entrance window, with 6 μm thickness (as given by the manufacturer), the smaller thickness that resisted a range of pressure tests that we conducted before IS543-I, will still be used in case the required beam energy is below the limit achievable by ISOLDE, given its development status. However this would constrain the new experiment to high energies, with regards to the Gamow window, which would not necessarily fulfil the scientific case.

In the ideal case, the cross section for the ^{44}Ti(α, p)^{47}V reaction shall be studied at 4 energies, given here in the centre of mass frame for the α-particle: 6 MeV, 5.5 MeV, 5 MeV, and 4 MeV. The motivation for this choice is to 1) corroborate the results from Sonzogni *et al.* [Sonzogni 2000] at 6 MeV, the high energy end of the Gamow window, 2) map out the cross section behaviour in the 5-6 MeV region of the Gamow window, where the cross section is high, 3) confirm and obtain a cross section value at the 4 MeV, the energy used in the first phase of IS543. Upon obtaining of meaningful measurements, lower reaction energies could potentially be investigated.

The progress made by the CERN beam development team in understanding the ^{44}Ti source means that it is not foolish to seek for an increase of a factor

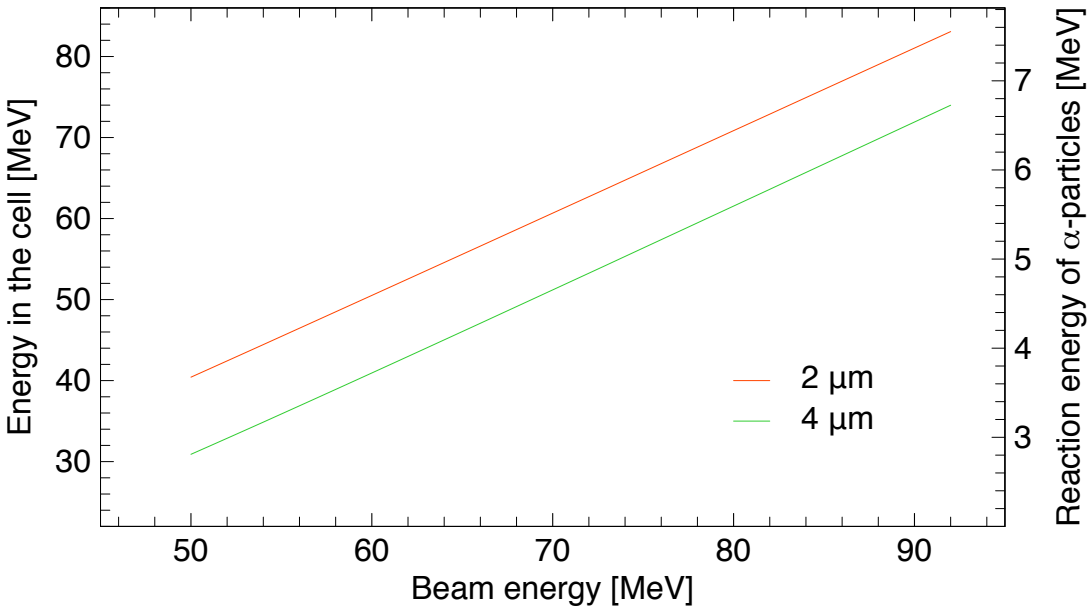

Figure 8.1: Dependence of the final energy of the ^{44}Ti particles upon the delivered beam energy for Mylar window thicknesses of 2 and 4 μm.

of 10 to 100 in beam intensity. For an increase of a factor of 50, the beam intensity would be in the range 25 to 100×10^6 pps, the expected count rate for the ^{44}Ti(α, p)^{47}V is presented in Table 8.2. (The figures shown there are drawn considering a similar increase of the cross section at 6 MeV to that measured by Sonzogni *et al.* value at 5.8 MeV, the `NON-SMOKER` prediction at 5.5 and 5 MeV, and our upper limit from the previous measurement at 4.15 MeV.)

Table 8.2: Expected event rate, in the S2-telescope, for the ^{44}Ti(α, p)^{47}V reaction at 4, 5, 5.5 and 6 MeV in the centre of mass of the reacting α-particle, for a beam intensity of 50×10^6 pps. The rates are given following two possible entrance foil materials. It is assumed that the detector is at 12 cm downstream and that its efficiency is 100%

Entrance window foil	^{4}He gas pressure [mBar]	Reaction energy [MeV]	E_{beam} [MeV/u]	σ [mbarn]	Event rate [counts/s]
Mylar (3 μm)					
	200	4	1.32	<0.05	∼0.003
	200	5	1.57	0.7	∼0.04
	200	5.5	1.68	3.5	∼0.2
	200	6	1.81	15	∼1
Al (6 μm)					
	70	4	2.08	<0.05	∼0.001
	70	5	2.60	0.7	∼0.02
	70	5.5	2.86	3.5	∼0.08
	70	6	3.12	15	∼0.3

Bibliography

[Ahmad 2006] I. Ahmad, J.P. Greene, E.F. Moore, S. Ghelberg, A. Ofan, M. Paul and W. Kutschera, Phys. Rev. C **74**, 065803 (2006).

[Arnett 1989] David Arnett, John N. Bahcall, Robert P. Kirshner and Stanford E. Woosley, Annu. Rev. Astron. Astrophys. **27**, 629 (1989).

[Arnett 1996] David Arnett, *Supernovae and Nucleosynthesis: An Investigation of the History of Matter, from the Big Bang to the Present*, Princeton University Press, 1996.

[Audi 2003] G. Audi, A.H. Wapstra and C. Thibault, Nucl. Phys. **A729**,337 (2003).

[Basunia 2011] M. Shamsuzzoha Basunia, Nuclear Data Sheets **112**, 1875 (2011)

[Bazin 2003] D. Bazin *et al.*, Nucl. Instrum. Methods Phys. Res. B **204**, 629 (2003) 14th International Conference on Electromagnetic Isotope Separators and Techniques Related to their Applications.

[Benamara 2014] S. Benamara, N. de Séréville *et al.*, Phys. Rev. C **89**, 065805 (2014).

[Bester 1996] M. Bester *et al.* Astrophys. J. **463**, 336 (1996).

[Bethe 1985] H.A. Bethe and J.R. Wilson, Astrophys. J **295**, 14 (1985).

[Bionta 1987] R.M. Bionta *et al.*, Phys. Rev. Lett. **58**, 1494 (1987).

[Boggs 2015] S.E. Boggs *et al.*, Science **348**, 670 (2015).

[Brown 2014] B.A. Brown, W.A. Richter, and C. Wrede, Phys. Rev. C **89**, 062801(R) (2014).

[Bown & Richter 2006] B.A. Brown, W.A. Richter, Phys. Rev. C **74**, 034315 (2006).

[Buchmann 1980] L. Buchmann, H.W. Becker, K.U. Kettner, W.E. Kieser, P. Schmalbrock and C. Rolfs, Z. Physik - Atoms and Nuclei **296**, 273 (1980).

[Buchmann 1984] L. Buchmann, M. Hilgemeier, A. Krauss, A. Redder, C. Rolfs, H.P. Trautvetter, and T.R. Donoghue, Nucl. Phys. **A415**, 93 (1984).

[B^{2}HF 1957] E. Margaret Burbridge, G.R. Burbridge, William A. Fowler and F. Hoyle, Review of Modern Physics **29**, 547 (1957).

[Champagne 1990] A.E. Champagne, P.V. Magnus, M.S. Smith and A.J. Howard, Nucl. Phys. **A512**, 317 (1990).

[Chevalier 1992] R.A. Chevalier, Nature **355**, 691 (1992).

[Churazov 2014] E. Churazov *et al.*, Nature **512**, 406 (2014).

[Couch 2015] Sean M. Couch, Emmanouil Chatzopoulos, W. David Arnett, and F.X. Timmes, arXiv:1503.02199v1 (2015).

[Daehnick 1980] W.W. Daehnick, J.D. Childs and Z. Vrclej, Phys. Rev. C**21**, 2253 (1980).

[deVoigt 1971a] M.J.A. de Voigt, J.W. Maas, D. Veenhof and C. van der Leun, Nucl. Phys. **A170**, 449 (1971).

[deVoigt 1971b] M.J.A. de Voigt, J. Grootenhuis, J.B. van Meurs and C. van der Leun, Nucl. Phys. **A170**, 467 (1971).

[Diehl 1995] R. Diehl *et al.*, Astron. Astrophys. **298**, 445 (1995).

[Diehl 2006] R. Diehl *et al.*, Nature **439**, 45 (2006).

[Diehl 2014] R. Diehl, T. Siegert, W. Hillebrandt, S.A. Grebenev, J. Greiner, M. Krause, M. Kromer, K. Maeda, F. Ropke, and S. Taubenberger, Science **345**, 1162 (2014).

[Diehl website] http://www2011.mpe.mpg.de/gamma/science/lines/26Al/26Al.html, last visited on January 22, 2016.

[Dressler 2012] R. Dressler, M. Ayranov, D. Bemmerer, M. Bunka, Y. Dai, C. Lederer, J. Fallis, A.StJ. Murphy, M. Pignatari, D. Schumann, T. Stora, T. Stowasser1, F.-K. Thielemann and P.J. Woods, J. Phys. G: Nucl. Part. Phys. **39**, 105201 (2012).

[ERAWAST] https://www.psi.ch/lch/, last visited on March 22, 2016.

[Feldman & Cousins 1998] Gary J. Feldman and Robert D. Cousins, Phys. Rev. D **57**, 3873 1998.

[Fisher 2014] David B. Fisher, Alberto D. Bolatto, Rodrigo Herrera-Camus, Bruce T. Draine, Jessica Donaldson, Fabian Walter, Karin M. Sandstrom, Adam K. Leroy, John Cannon & Karl Gordon, Nature **505**, 186 (2014).

[Gade 2008] A. Gade *et al.*, Phys. Rev. C **77**, 044306 (2008).

[Gomes 2005] P.R.S. Gomes, J. Lubian, I. Padron, R.M. Anjos, Phys. Rev. C **71**, 017601 (2005).

[Grebenev 2012] S.A. Grebenev, A.A. Lutovinov, S.S. Tsygankov and C. Winkler, Nature **490**, 373 (2012).

[Grefenstette 2014] B.W. Grefenstette *et al.*, Nature **506**, 339 (2014).

[Habs 2000] D. Habs *et al.*, Hyperfine Interactions **129**, 43 (2000).

[Henley 1969] E.M. Henley. *Isospin in nuclear physics.*, ed. D.H. Wilkinson. North Holland, Amsterdam, 1969.

[Hoffman 2010] R.D. Hoffman *et al.*, Astrophys. J. **715**, 1383 (2010).

[Iliadis 1990] Ch. Iliadis, Th. Schange, C. Rolfs, U. Schröder, E. Somorjai, H.P. Trautvetter and K. Wolke, P.M. Endt, S.W. Kikstra, A.E. Champagne, M. Arnould and G. Paulus, Nucl. Phys. **A512**, 509 (1990).

[Iliadis 2011] C. Iliadis, A.E. Champagne, A. Chieffi, and M. Limongi, Astrophys. J. Suppl. Ser. **193**, 16 (2011).

[Iyudin 1994] A. F. Iyudin *et al.*, Astron. Astrophys. **284**, L1 (1994).

[Iyudin 1998] A. F. Iyudin, V. Schönfelder, K. Bennett, H. Bloemen, R. Diehl, W. Hermsen, G.G. Lichti, R.D. van der Meulen, J. Ryan and C. Winkler, Nature **396**, 142 (1998).

[Janka 2007] H.-Th. Janka, K. Langanke, A. Marek, G. Martinez-Pinedo and B.Müller, Phys. Rep. **442**, 38 (2007).

[Johnson & Tandy 1974] R.C. Johnson and P.C. Tandy, Nucl. Phys. **A235**, 56 (1974).

[Jose 1997] J. Jose, M. Hernanz, and A. Coc, Astrophys. J. **479**, L55 (1997).

[Kankainen 2016] A. Kankainen *et al.*, Eur. Phys. J. A **52**, 6 (2016).

[Keller 2014] S.C. Keller, M.S. Bessell, A. Frebel, A.R. Casey, M. Asplund, H.R. Jacobson, K. Lind, J.E. Norris, D. Yong, A. Heger, Z. Magic, G.S. Da Costa, B.P. Schmidt & P. Tisserand, Nature **506**, 463 (2014).

[Koning & Delaroche 2003] A.J. Koning and J.P. Delaroche, Nucl. Phys. **A713**, 231 (2003).

[Lane 1960] A.M. Lane, Rev. Mod. Phys. **32**, 519 (1960).

[Lawson 1980] R. D. Lawson. *Theory of the Nuclear Shell Model. Oxford studies in nuclear physics*, Clarendon Press, Oxford, 1980.

[Lee 1977] T. Lee, D.A. Papanastassiou, and G.J. Wasserburg, Astrophys. J. **211**, L107 (1977).

[Lickert 1988] M. Lickert, J. Brenneisen, F. Glatz, D. Grathwohl, A. Martinez v. Remisowski, H. Röpke, J. Siefert, and B.H. Wildenthal, Z. Phys. A - Atomic Nuclei **331**, 409 (1988).

[Lotay 2009] G. Lotay, P.J. Woods, D. Seweryniak, M.P. Carpenter, R.V.F. Janssens, and S. Zhu, Phys. Rev. Lett. **102**, 162502 (2009).

[Lotay 2011] G. Lotay, P.J. Woods, D. Seweryniak, M.P. Carpenter, H.M. David, R.V.F. Janssens, and S. Zhu, Phys. Rev. C **84**, 035802 (2011).

[Magkotsios 2010] G. Magkotsios, F. X. Timmes, A. L. Hungerford, C. L. Fryer, P. A. Young, and M. Wiescher, Astrophys. J. Suppl. Series **191**, 66 (2010).

[Mahoney 1982] W.A. Mahoney, J.C. Ling, A.S. Jacobson, and R.E. Lingenfelter, Astrophys. J. **262**, 742 (1982).

[Margerin 2012] V. Margerin, MPhil thesis, The Australian National University, 2012.

[Margerin 2014] V. Margerin, A.St.J. Murphy, T. Davinson, R. Dressler, J. Fallis, A. Kankainen, A.M. Laird, G. Lotay, D.J. Mountford, C.D. Murphy, C. Seiffert, D. Schumann, T. Stowasser, T. Stora, C.H.-T. Wang, P.J. Woods, Phys. Lett. B**731**, 358 (2014).

[Margerin 2015] V. Margerin, G. Lotay, P.J. Woods, M. Aliotta, G. Christian, B. Davids, T. Davinson, D.T. Doherty, J. Fallis, D. Howell, O.S. Kirsebom, D.J. Mountford, A. Rojas, C. Ruiz, and J.A. Tostevin, Phys. Rev. Lett. **115**, 062701 (2015).

[Margerin 2016a] V. Margerin, G.J. Lane, G.D. Dracoulis, N. Palalani, M.L. Smith and A.E. Stuchbery, accepted for publication in Phys. Rev. C.

[Margerin 2016b] V. Margerin, G. Lotay *et al.*, in preparation for submission to Phys. Rev. C.

[Meurders & van der Steld 1974] F. Meurders and A. van der Steld, Nucl. Phys. **A230**, 317 (1974).

[Mohr 2014] P. Mohr, Phys. Rev. C **89**, 058801 (2014).

[Mohr 2015] P. Mohr, Eur. Phys. J. A **51**, 56 (2015).

[Moss & Sherman 1976] C.E. Moss and J.D. Sherman, Nucl. Phys. **A259**, 413 (1976).

[MSL S2] Micron Semiconductor Ltd. http://www.micronsemiconductor.co.uk, last visited on March 15, 2016.

[Ormand & Brown 1989] W. Ormand, B.A. Brown, Nucl. Phys. **A491**, 1 (1989).

[Pain 2015] S.D. Pain *et al.*, Phys. Rev. Lett. **114**, 212501 (2015).

[Parikh 2014] A. Parikh, J. Jose, A. Karakas, C. Ruiz, and K. Wimmer, Phys. Rev. C **90**, 038801 (2014).

[Perego 2015] A. Perego, M. Hempel, C. Fröhlich, K. Ebinger, M. Eichler, J. Casanova, M. Liebendörfer, and F.-K. Thielemann, ApJ **806**, 275 (2015).

[Rauscher 1998] T. Rauscher and F.-K. Thielemann, in *'Stellar Evolution, Stellar Explosions and Galactic Chemical Evolution'*, edited by A. Mezzacappa (IOP, Bristol, 1998), p. 519.

[Rauscher 2001] T. Rauscher and F.-K. Thielemann, Atomic Data Nuclear Data Tables **75** (2000) 1 and **79**, 47 (2001).

[Reichard 2012] L. Reichard *et al.*, Phys. Rev. C **85**, 065801 (2012).

[Renaud 2006] M. Renaud *et al.*, Astrophys. J. **647**, L41 (2006).

[Ruiz 2003] C. Ruiz, PhD thesis, The University of Edinburgh, 2003.

[Ruiz 2006] C. Ruiz *et al.*, Phys. Rev. Lett. **96**, 252501 (2006).

[Salter 2012] P.J.C. Salter, PhD thesis, The University of Edinburgh, 2012.

[Serpico 2004] P.D. Serpico, S. Esposito, F. Iocco, G. Mangano, G. Miele and O. Pisanti, J. of Cosm and Astro. Phys. **12**, 010 (2004).

[Siess & Arnould 2008] L. Siess and M. Arnould, Astron.Astrophys. **489**, 395(2008).

[Schatz & Rehm 2006] H. Schatz and K.E. Rehm, Nucl. Phys. **A777**, 601 (2006).

[Show 1976] D.L. Show, B.H. Wildenthal, J.A. Nolen Jr. and E. Kashy, Nucl. Phys. **A263**, 293 (1976).

[Smit 1982] J.J.A. Smit, J.P.L. Reinecke, M.A. Meyer, D. Reitmann and P.M. Endt, Nucl. Phys. **A377**, 15 (1982).

[Smith 2009] Nathan Smith, Kenneth H. Hinkle, and Nils Ryde, Astronom. J. **137**, 3558 (2009).

[SNO 2001] Q.R. Ahmad *et al.*, SNO collaboration, Phys. Rev. Lett. **87**, 071301 (2001).

[Sonzogni 2000] A.A. Sonzogni *et al.*, Phys. Rev. Lett. **84**, 1651 (2000).

[SRIM] *SRIM 2006.02* http://www.srim.org, last visited on March 15, 2016.

[Srinivasan 1999] G. Srinivasan, J.N. Goswami, and N. Bhandari, Science **284**, 1348 (1999).

[Stora 2013] T. Stora, Nucl. Instr. Meth. **B 317**, 402 (2013).

[The 1998] L.-S. The, D.D. Clayton, L. Jin and B.S. Mayer, Astrophys. J. **504**, 500 (1998).

[Thompson 1988] I. Thompson, Comput. Phys. Rep. **7**, 167 (1988).

[Thompson & Nunes 2009] Ian J. Thompson and Filumena M. Nunes, *Nuclear Reactions for Astrophysics*, Cambridge University Press, 2009.

[Timmes 1996] F.X. Timmes, S.E. Woosley, D.H. Hartmann and R.D. Hoffman, Astrophys. J. **464**, 332-341 (1996).

[Timofeyuk 2003] N.K. Timofeyuk, R.C. Johnson, and A.M. Mukhamedzhanov, Phys. Rev. Lett. **91**, 232501 (2003).

[Timofeyuk 2006] N.K. Timofeyuk, P. Descouvemont, and R.C. Johnson, Eur. Phys. J. A **27**, 269 (2006).

[Tostevin] J. A. Tostevin, University of Surrey version of the code TWOFNR (of M. Toyama, M. Igarashi and N. Kishida) and code FRONT (private communication).

[Tostevin communic.] Private communication with J. Tostevin, September 2014.

[TWOFNR] Report of M. Toyama and M. Igarashi 1972-1977 available at `www.nucleartheory.net/NPG/codes/twofnr.pdf`, last visited March 15, 2016.

[Tur 2010] C. Tur, A. Heger and S. M. Austin, Astrophys. J. **718**, 357-367 (2010).

[vanRaai 2008] M.A. van Raai, M. Lugaro, A.I. Karakas, and C. Iliadis, Astron. Astrophys. **478**, 521 (2008).

[Varner 1991] R. Varner, W. Thompson, T. McAbee, E. Ludwig, and T. Clegg, Physics Reports **201**, 57 (1991).

[Vink 2001] J. Vink, J. M. Laming, J. S. Kaastra, J.A.M. Bleeker, H. Bloemen, and U. Oberlack, Astrophys. J. **560**, L79-L82 (2001).

[Vogelaar 1989] R.B. Vogelaar, Ph.D. thesis, California Institute of Technology, 1989.

[Vogelaar 1996] R.B. Vogelaar, L.W. Mitchell, R.W. Kavanagh, A.E. Champagne, P.V. Magnus, M.S. Smith, A.J. Howard, P.D. Parker, and H.A. OBrien, Phys. Rev. C **53**, 1945 (1996).

[Wallner 2015] A. Wallner *et al.* Nature Communications **6**, 5956 (2015).

[Wang 2009] W. Wang *et al.*, Astron. Astrophys. **496**, 713 (2009).

[Wasserburg 2006] G. Wasserburg, M. Busso, R. Gallino, and K.M. Nollett, Nucl. Phys. **A777**, 5 (2006).

[Westerfeldt & Mitchell 1978] C.R. Westerfeldt and G.E. Mitchell, Nucl. Phys. **A303**, 111 (1978).

[Wiringa 1995] R.B. Wiringa, V.G.J Stoks and R. Schiavilla, Phys. Rev. C **51**, 38 (1995).

[Yoon 2010] Jinmi Yoon , Deane M. Peterson, Robert L. Kurucz, and Robert J. Zagarello, Astrophys. J. **708**, 71 (2010).

[Zampieri 1998] Luca Zampieri, Monica Colpi, Stuart L.Shapiro, and Ira Wasserman, Astrophys. J. **505**, 876 (1998).